BINDING SERVICES
Tel +44 (0)29 2087 4949
Fax +44 (0)29 20371921
e-mail bindery@cardiff.ac.uk

Internal field effects in InGaN quantum wells

by

Iain Brown

A thesis submitted to the
University of Wales
for the degree of
Doctor of Philosophy

UMI Number: U584703

All rights reserved

INFORMATION TO ALL USERS
The quality of this reproduction is dependent upon the quality of the copy submitted.

In the unlikely event that the author did not send a complete manuscript
and there are missing pages, these will be noted. Also, if material had to be removed,
a note will indicate the deletion.

UMI U584703
Published by ProQuest LLC 2013. Copyright in the Dissertation held by the Author.
Microform Edition © ProQuest LLC.
All rights reserved. This work is protected against
unauthorized copying under Title 17, United States Code.

ProQuest LLC
789 East Eisenhower Parkway
P.O. Box 1346
Ann Arbor, MI 48106-1346

Acknowledgements

I would like to thank my PhD supervisors Dr. Peter Smowton and Prof. Peter Blood for their advice and time over the duration of this project. A number of individuals and organisations have helped to make my research possible, and I would like to thank them for their contributions. Firstly, Prof. Weng Chow, who developed the original model, kindly made it available for my use, and who has provided in–depth knowledge and insights into the more complex aspects of my work. Secondly, Iestyn Pope and Santiago Olaizola Izquierdo for their experimental work. Thirdly, the Engineering and Physical Sciences Research Council (EPSRC) which provided financial support for this project and finally the members of the optoelectronics group, especially my old office mates Davey, Helen and Lois!

Additional thanks to the postgrad community in the department, especially my good friends Hannah, Emma, Iestyn and Dave for their support and many fun times over the years!

Thanks are also due to the magical properties of the coffee bean which have seen me through my research!

Thanks to my parents and my sister for all their support over the years.

Finally, a special thanks to my wife, Maddy, for always being there, for understanding, and for helping to keep me sane!

Nobody said it was easy
No one ever said it would be this hard
Oh take me back to the start
I was just guessing
At numbers and figures
Pulling your puzzles apart
Questions of science
Science and progress
Do not speak as loud as my heart

The Scientist–Coldplay

Abstract

InGaN/GaN based quantum well structures are strained and due to the lack of a centre of symmetry large internal fields are present which skew the potential of the quantum wells, this has a large effect on the properties of these structures. InGaN/GaN based quantum well structures are studied using a theoretical method based on the Pade model and comparison made with experimental results.

The importance of using a correct description for the depletion widths of p–i–n structures for use in interpreting measurements of the internal field is established in this work. Interpreting the results from reverse bias photocurrent absorption measurements of an $In_{0.1}Ga_{0.9}N$ quantum well structure, a value of –1.9 $MVcm^{-1}$ for the internal field has been determined, which is within 5 % of the field of –1.8 $MVcm^{-1}$ calculated using piezoelectric constants interpolated from the binaries. Comparison of the results of the Pade model and experiment demonstrate that the experimental absorption magnitude is an unreliable indication of the internal field due to the carrier extraction efficiency at low bias, hence the absorption peak energy should be used.

Using a theoretical model governed by pumping and recombination processes time–resolved photoluminescence experiments performed at Sheffield University have been modelled. It was found that the observed shift of the emission peak arises from a delicate balance between the contributions from bandgap renormalisation, screening of the internal field and the Coulomb interaction. Comparisons between the free carrier and Pade models, found that the energy shift and magnitude of the peak intensity are underestimated when using the free carrier model. Although the internal field is strongly screened at high carrier density, the increase in the dipole matrix element is small. It was found that at threshold the screened internal field is still of the order of –1 $MVcm^{-1}$, hence inclusion of the screened internal field is essential in laser gain–current calculation.

Contents

1 Introduction and background. **1**
- 1.1 Introduction. 2
- 1.2 Lasers. 2
- 1.3 History of gallium nitride. 5
- 1.4 Properties of gallium nitride. 8
  - 1.4.1 Structure. 8
    - 1.4.1.1 Zinc blende. 9
    - 1.4.1.2 Wurtzite. 10
  - 1.4.2 Substrate. 11
  - 1.4.3 Strain. 12
  - 1.4.4 Internal field. 13
- 1.5 Applications of gallium nitride. 14
  - 1.5.1 Optical storage. 14
  - 1.5.2 LEDs. 15
- 1.6 Summary. 16
- 1.7 Rationale and outline. 16

2 Internal field. **19**
- 2.1 Introduction. 19
- 2.2 Internal field. 20
- 2.3 Spontaneous polarization. 21
- 2.4 Piezoelectric field. 22
- 2.5 Screening of the internal field. 27
- 2.6 Average screening of the internal field. 28
- 2.7 Summary. 29

3 Pade model. **31**
- 3.1 Introduction. 31
- 3.2 Gain. 31
  - 3.2.1 Hamiltonian: Kinetic energy 34
  - 3.2.2 Hamiltonian: Free carrier. 35
  - 3.2.3 Hamiltonian: Coulomb. 36
- 3.3 Pade model. 37
- 3.4 Screening of the Coulomb potential. 42
- 3.5 Bandgap renormalisation. 47

3.5.1 Debye shift. 47
3.5.2 Exchange shift. 48
3.6 Program details. 49
3.7 Summary. 49

4 Programming issues. 51
4.1 Introduction. 51
4.2 Computing issues. 52
4.3 Bandgap. 53
4.4 Band offset ratio. 54
4.5 Internal field. 55
4.6 Screening of the internal field. 58
4.7 Homogeneous lineshape function. 60
4.8 Spontaneous emission. 63
4.9 Contributions from different transitions. 65
4.10 Contributions to the Pade model. 66
4.10.1 Bandgap renormalisation. 66
4.10.1.1 Rigid shift approximation. 69
4.10.2 Internal field. 70
4.10.3 Coulomb enhancement. 71
4.10.4 Pade model. 72
4.11 Summary. 73

5 Measurement of the internal field. 75
5.1 Introduction. 76
5.2 Reverse bias photocurrent. 78
5.3 Effective internal field. 80
5.4 Depletion width. 81
5.4.1 Depletion width: p–n junction approximation. 82
5.4.2 Depletion width: p–i–n method. 85
5.5 Published results. 90
5.6 Further experimental data. 91
5.6.1 Structure details. 91
5.6.2 Experimental details. 92
5.6.3 Theory. 93
5.7 Results. 94
5.8 Summary. 98

6 Screening of the internal field. 99
6.1 Introduction. 99
6.2 Photoluminescence spectroscopy. 100
6.3 Stretched exponential lineshape. 105
6.4 Theoretical modelling. 108
6.4.1 Carrier density. 109
6.4.2 Lifetime. 110

6.5 Time–resolved results. 111
6.5.1 Contributions to the Pade model. 116
6.5.2 Carrier density. 119
6.5.3 Screened internal field. 120
6.5.4 Wavefunction overlap integral and dipole matrix. 121
6.5.5 Radiative lifetime. 124
6.5.6 Overall lifetime. 125
6.5.7 Efficiency. 126
6.6 Extrapolation to high carrier density. 127
6.6.1 Screened internal field. 127
6.6.2 Wavefunction overlap integral and dipole matrix. 128
6.6.3 Radiative lifetime. 131
6.6.4 Material gain. 132
6.7 Summary. 137

7 Summary and future work. 139
7.1 Summary. 139
7.2 Future work. 141

Bibliography 143

List of Figures

1.2.1 Bandgap as a function of lattice constant for zinc blende structures. 5
1.3.1 Publications of GaN related papers. 7
1.4.1 Zinc blende structure 9
1.4.2 Wurtzite structure 10
1.4.3 Wurtzite structure: Ga–face and N–face 11

2.1.1 Well shape and wavefunction for square and skewed quantum wells. 19
2.4.1 Directions of strain and shear strain 24

4.3.1 Bandgap of InN. 53
4.4.1 Band offset ratio. 54
4.5.1 Strain in $In_xGa_{1-x}N/GaN$ quantum wells. 55
4.5.2 Internal field in $In_xGa_{1-x}N/GaN$ quantum wells. 56
4.6.1 Average and $z-$dependent screening field. 59
4.6.2 Well shape due to average and $z-$dependent screened internal field. 60
4.7.1 Sech and Lorentzian lineshape functions. 61
4.7.2 Gain spectrum using the sech and Lorentzian lineshape functions. . 62
4.7.3 Gain spectra for different values of homogeneous lineshape factor. . 63
4.8.1 Spontaneous emission spectra obtained from gain spectra. 64
4.9.1 Contributions to gain spectra different transitions. 65
4.10.1 Energy shift due to bandgap renormalisation. 67
4.10.2 The effect of renormalisation on the shape of the gain spectra. . . 68
4.10.3 Bandgap renormalisation: full regime and rigid shift approximation. 69
4.10.4 Gain spectra changes due to screening of the internal field. 70
4.10.5 Effects of the Coulomb enhancement on the gain spectra. 71
4.10.6 Gain spectra calculated at different levels of model approximation. 72

5.1.1 Increase in internal field with In from published results. 77
5.2.1 p–i–n junction under zero and reverse biases. 78
5.2.2 Well shape due to the internal and applied fields. 80
5.4.1 Electric field across the p–i–n structure using Simwin^{TM}. 83
5.4.2 Electric field across a p–i–n structure. 84
5.4.3 Electric field across a p–i–n structure. 89
5.6.1 Experimental photocurrent absorption spectrum. 92
5.7.1 Depletion width as a function of reverse bias. 94

5.7.2 Energy and amplitude of peak absorption as a function of reverse bias. 95
5.7.3 Internal field as a function of applied reverse bias. 96
5.7.4 The effects of donor doping fluctuations. 97

6.2.1 Optical pumping of InGaN/GaN quantum wells. 102
6.2.2 Experimental time evolution of the peak energy. 103
6.2.3 Experimental time evolution of the energy–integrated intensity. . . 104
6.3.1 Stretched exponential lineshape function. 106
6.3.2 Comparison of experimental results and stretched lineshape function. 107
6.5.1 Time evolution of the energy of the peak intensity. 112
6.5.2 Time evolution of the energy–integrated intensity. 114
6.5.3 The sensitivity of the theoretical fit to the Pump and non–radiative lifetime parameters. 115
6.5.4 Energy variations of the peak intensity with carrier density. 117
6.5.5 Energy–integrated intensity variations with carrier density. 118
6.5.6 Modelled time evolution of the carrier density. 120
6.5.7 Modelled time evolution of the screened internal field. 121
6.5.8 Modelled time evolution of the wavefunction overlap integral. 122
6.5.9 Modelled time evolution of the relative dipole matrix element. . . . 123
6.5.10 Modelled time evolution of the radiative lifetime. 124
6.5.11 Modelled time evolution of the overall lifetime. 125
6.5.12 Modelled time evolution of the efficiency. 126
6.6.1 Variation of the screened internal field with carrier density. 127
6.6.2 Variation of the wavefunction overlap integral with carrier density and internal field. 129
6.6.3 Variation of relative dipole matrix element with carrier density. . . 130
6.6.4 Radiative lifetime as a function of carrier density. 132
6.6.5 Variation of material gain with carrier and radiative current density. 133
6.6.6 Variation of material gain, hole Fermi energy and dipole matrix element with carrier density. 135

List of Tables

1.5.1 Optical storage methods 14
1.5.2 Comparison of light bulbs and LEDs 15

5.1.1 Internal field in InGaN/GaN quantum wells. 76

6.2.1 Device structure. 102
6.3.1 Stretched exponential lineshape function parameters. 105
6.5.1 Model parameters. 116
6.5.2 Calculated energy shift. 119

Chapter 1

Introduction and background.

Gallium nitride has evolved from a research curiosity to an important semiconductor, as the growth and fabrication have improved in recent years [1]. In particular, the development of nitride–based blue–green light–emitting diodes (LEDs) has dramatically opened the spectral range available for semiconductor emitters and the actual and potential impact of these materials is widespread. Applications are in two main markets: one for optoelectronic products–solid state lighting and optical storage; the other for electronic applications that include high power microwave, wireless and satellite communications. However, even though blue and green light emitting diodes and lasers based on GaN are already being mass produced and are commercially available, the light generation mechanisms are poorly understood [2]. GaN has been studied to greater extent than the other III–N materials, but the depth of knowledge is still not as extensive as for Si and GaAs for example [3]. InGaN/GaN structures are strained due to lattice mismatch and because of the lack of centre of symmetry this generates a large internal field of the order of $MVcm^{-1}$. By improving the knowledge of the internal field, the structural design and hence the performance can be improved [4, 5]. This can be achieved by experimentally investigating these structures using different techniques, and through the simulation of the working device, yielding further understanding of the intrinsic properties of InGaN/GaN structures.

1.1 Introduction.

In this chapter a background of the laser is covered in section 1.2. In section 1.3, a brief history and background to GaN based structures is introduced. I have assumed a general knowledge of semiconductor physics and have only included a description of features specific to the GaN/InGaN material system. In section 1.4 the properties of GaN are introduced, with the structure and substrate covered in sections 1.4.1 and 1.4.2 respectively. In sections 1.4.3 and 1.4.4 the issue of strains and internal field are introduced. In section 1.5, the general applications of GaN based devices are discussed, with the specific cases of optical storage and LEDs covered at greater length in sections 1.5.1 and 1.5.2 respectively. Finally in section 1.6 the chapter is summarised.

1.2 Lasers.

Is this section a brief introduction to the laser is covered, many books address this topic and the interested reader is referred to books written by Kittel [6], Sze [7] and Coldren and Corzine [8] for further information.

The word 'laser' is an acronym for light amplification by stimulated emission of radiation and can be thought of as way to control the release of photons by energised atoms. A material, which contains atoms in the excited states, emits radiation when electrons fall from the higher energy levels to the lower levels. This process normally occurs randomly and is known as spontaneous emission. The emitted radiation is incoherent and travels in all directions. The energy of the photon i.e. the colour of the light, depends on the energy gap between the excited and ground states, for a semiconductor this is known as the bandgap and depends on the material system. The process can also be induced and this is known as stimulated emission, this happens when a photon causes the transition of the electron to the lower state and in doing so another photon is emitted. The two photons have the same phase, frequency and direction. Stimulated emission from an inverted population was

first demonstrated by Townes in 1954, this was done using a maser which is a laser operating at microwave wavelengths. The first true laser was developed by Maiman, using a ruby crystal in 1960.

A laser is designed so that the rate of stimulated emission surpasses that of spontaneous emission. For this to occur the photon density must be large and the population must be inverted i.e. more electrons must be in the upper (conduction) than the lower (valence) state. Population inversion can be achieved by optical or electrical means; solid state and gas lasers e.g. ruby are optically pumped and semiconductor lasers such as GaAs are electrically pumped. We shall concentrate on semiconductor lasers in this work but the reader is referred to books such those written by Siegman [9] and Silfvast [10] for information on the other laser types.

A light emitting diode consists of a p–n junction and when a current is applied, electrons and holes are injected into the n–type and p–type regions respectively. The increased carrier density leads to the recombination of electrons and holes at the junction and the creation of photons by spontaneous emission. As it is difficult to grow large crystals that are pure enough to emit light, thin pure layers are grown by epitaxy on top of a poorer quality substrate. If the substrate and epitaxial layers are not lattice matched, defects can occur which degrade the optical quality and this is discussed in section 1.4.2. The operation of the semiconductor laser is characteristically the same as an LED, but a waveguide is introduced to confine the light and the opposite faces of the semiconductor are cut and polished, this forms a optical cavity, so laser light is reflected back and forth within the crystal promoting stimulated emission. The light emitted by lasers is coherent and monochromatic.

The structure described above is a homojunction because the material is the same on both sides of the junction, but almost all practical injection lasers are based on the double heterostructure which was proposed by H. Kroemer, for which he received the Nobel Prize for physics in 2000. In this a layer of narrower bandgap and higher refractive index material known as the active region is sandwiched between two layers of wider bandgap material. The potential barrier on each side prevents the flow of electrons to the p–type and holes to the n–type region, respectively [6],

hence the double heterostructure allows laser action at much lower current densities than a homojunction device. If the thickness of the active layer is close to the De–Broglie wavelength, which is around 10 nm for semiconductors then quantum effects become apparent and the quantised electron energies take on a discrete nature [11]. The optical field is confined by the higher refractive index of the active region and the fraction of the total light intensity in the active layer is known as the confinement factor. The materials used in the heterostructure must have similar lattice constants, which restricts the choice of material. If there are differences between the lattice constants of the heterostructure strains occur which can have large effects on the operation of these devices and this is discussed further in the following sections and in chapter 2. In figure 1.2.1 is a plot of lattice constant as a function of bandgap for selected III–V zinc blende semiconductors, the visible spectrum covers the energy range from approximately 1.8 to 3.1 eV.

The Optoelectronics industry has long been dominated by devices based on GaAs which emits in the infrared and by alloying with Al to form AlGaAs red emission can be achieved. Arsenic and phosphorus compounds suffer from an indirect bandgap as the bandgap gets larger, hence the compounds of GaP, AlP and AlAs which are shown in Figure 1.2.1 all have an indirect bandgap. In an indirect bandgap the conduction band minimum and the valence band maximum occur at different points in reciprocal space and hence a phonon and photon are emitted during a transition in order to conserve energy and momentum. Because this is a three particle process the lifetime of radiative transitions is long compared to non–radiative transitions in indirect bandgap structures, hence the radiative efficiency is low. Commercial devices are therefore made from direct bandgap compounds. Thus devices with increasing optical output and reliability, in a increasing range of colours have appeared on the market, but until recently no efficient device at the blue end of the spectrum was available. The creation of an efficient blue emitting device was a stumbling block for some time, without it displays using LED clusters and projection displays using solid state lasers based on LEDs, could not achieve a satisfactory white. In the following section a history of GaN and other blue emitting

devices is discussed.

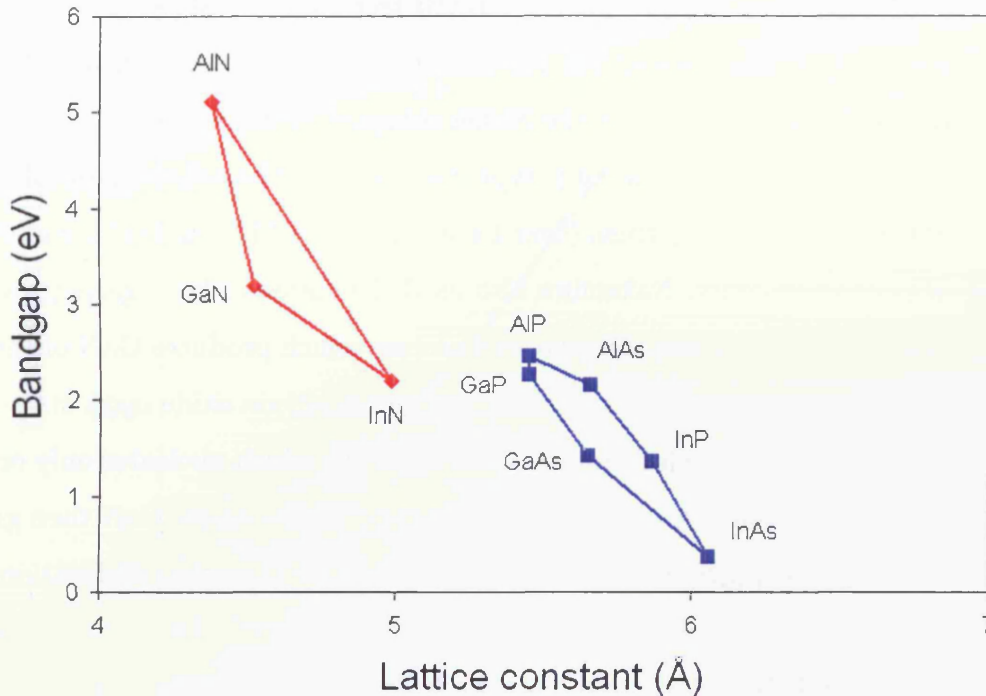

Figure 1.2.1: Bandgap as a function of lattice constant for zinc blende structures [12].

1.3 History of gallium nitride.

Although early progress with GaN as a blue emitter was promising, p–type doping was difficult to achieve, hence most of the research in the early 1990s was based on materials such as ZnSe and SiC. Commercial devices based on SiC were available, but due to the indirect bandgap these were inefficient light emitters and hence were not of a sufficient brightness to be of wide interest. Hence, research into the blue LEDs and laser diodes was based on ZnSe because the crystal growth was simpler in terms of lattice matched substrate and growth temperature compared with GaN. In 1991, the 3M company announced the first ZnSe based II–VI based blue laser diode, but the large degradation and hence short lifetimes of these structures resulted in difficulties in the commercialisation of these devices. The problem of p–type doping

of GaN was solved by Amano et al. [13] using low–energy electron–beam irradiation (LEEBI). They found that the LEEBI treatment of Mg–doped GaN reduced the resistivity and enhanced the PL efficiency of MOVPE–grown Mg–doped GaN p–n LEDs. Nakamura et al. of the Nichia company in Japan went on to show that using high temperature annealing p–type material could be achieved and the development of the first high brightness (over 1 candela) GaN LED in 1993 completed the range of primary colours. Nakamura also used the epitaxial lateral overgrowth technique (ELOG), this is a two stage growth process which produces GaN of very high structural quality. Using photomasking techniques silicon oxide mask stripes were grown on the GaN surface followed by GaN regrowth which nucleates only on the exposed GaN seed surfaces between the stripes [14]. High–quality GaN then grows laterally over the mask stripes, where it is unaffected by threading dislocations in the GaN seed layer and hence has very low defect densities [15]. Hence, Nichia were the early leaders in InGaN LED and laser diode technology, announcing commercially available blue GaN LEDs in 1993, green LEDs in 1995 [16], white LEDs in 1996 [17] and violet laser diodes in 1999 [18]. As a result of the breakthroughs at Nichia, most of the leading lighting application companies focused their attention on GaN as a medium for blue LEDs and laser diodes. In the past few years the group III nitride semiconductors have demonstrated their potential for advancing optical technologies across a range of applications and this is discussed in section 1.5. In addition, by alloying GaN with InN and AlN, the GaN based material system has the potential to be fabricated into devices which have active wavelengths from the red to the ultraviolet [3]. GaN based structures have been the subject of intensive research and product development for the past ten years and the dramatic increase in recent years of publications concerning GaN related issues can be seen in Figure 1.3.1. In addition to the problems already highlighted above, experiments have shown the presence of indium fluctuations in InGaN quantum wells due to localization during growth, as found for example by Cho et al. [21]. This is because at typical growth temperatures InGaN is unstable and phase separation into high and low indium phases occurs. Localised fluctuations in indium composition cause inhomogeneous

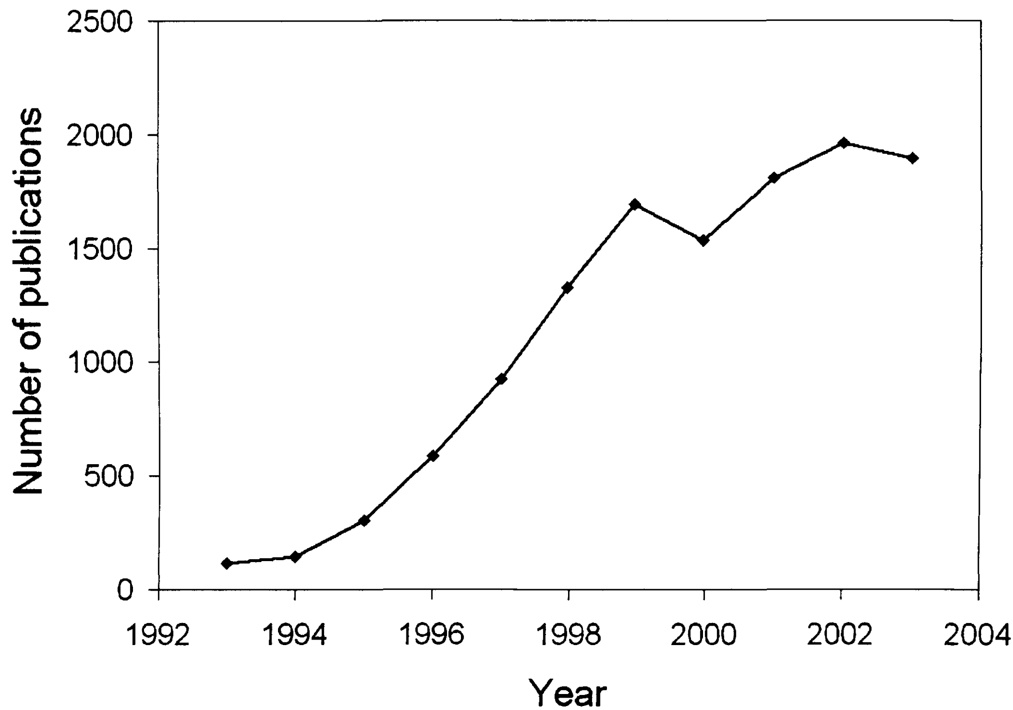

Figure 1.3.1: Publications of GaN related papers [19, 20].

broadening of the gain spectrum. This has been modelled by Chow et al. [22–24], who express the inhomogeneous broadened spectrum as the statistical average of the homogeneously broadened spectrum (discussed in sections 3.3 and 4.7). Inhomogeneous broadening due to fluctuations in indium composition was found to cause reduction in gain and a red–shift of up to of 130 meV [22]. Also, strong absorption at energies less than the bandgap has also been observed from AlN grown at low temperature [25], this can be explained by high defect or doping densities under the band edge which causes the formation of states which extend the bands into the energy gap, This is known as band tailing [26, 27]. The extent of band tailing in the forbidden energy band gap can be calculated using the Urbach equation and is a measure of the disorder in the material [28]. The effects of composition fluctuations and band tailing have not been taken into account in the results presented in this thesis.

1.4 Properties of gallium nitride.

The structural details of GaN are discussed in section 1.4.1 with the zinc blende and wurtzite formation detailed in sections 1.4.1.1 and 1.4.1.2, respectively. The substrate is described in section 1.4.2. Due to lattice mismatch InGaN/GaN structures experience large strains and these induce an internal field which is discussed in sections 1.4.3 and 1.4.4. Some of the applications of these devices are discussed in section 1.5.

1.4.1 Structure.

Some III–V materials are allotropic and either form a zinc blende (cubic) or wurtzite crystal structure. In ambient conditions, GaN favours the wurtzite crystal structure, as it is thermodynamically stable and minimises the free energy [1, 3, 29]. Zinc blende crystal structures can be grown by modifying the substrate and growth conditions [1, 29, 30], i.e. epitaxial growth of thin films on (011) crystal planes of cubic substrates such as Si, MgO and GaAs. In this case the tendency to form the thermodynamically stable wurtzite structure, has been overcome to produce metastable zinc blende structure, due to topological constraints. A third structure, rock–salt, can be induced under high pressure conditions [3, 7]. The cohesive energy of both zinc blende and wurtzite is quite similar [31], as the nearest neighbours are the same for both and it is the bond angle of the second nearest neighbours which determines the type of structure [31]. Most of the work completed so far has been on wurtzite structures, grown on a sapphire substrate (section 1.4.2), although there are advantages in using the zinc blende structures such as mirror facets compatible with GaAs substrates [32]. Hence both zinc blende and wurtzite structures have important applications in semiconductors and these structures are discussed in further detail in sections 1.4.1.1 and 1.4.1.2 respectively.

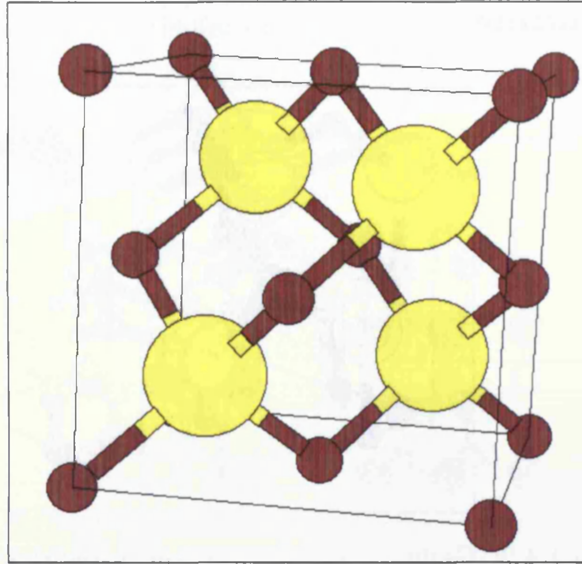

Figure 1.4.1: Gallium (yellow) nitride (brown) zinc blende structure [33].

1.4.1.1 Zinc blende.

In diamond each carbon atom forms covalent bonds with its four nearest neighbours which are arranged at the corners of a regular tetrahedron. Each carbon atom has four valence electrons which are effectively shared between it and one of its four nearest neighbours. This forms the chemical covalent bond, and there is no transfer of electric charge between different lattice locations. Hence there are eight shared electrons in four pairs of opposite spin in the outer shell of the carbon atom, which results in a very stable low energy structure [34]. Elemental semiconductors such as Si, Ge, and C, fall in this category [35]. The atoms can be split into two groups, to form a fcc Bravais lattice and a fcc lattice displaced by one quarter of a unit cell in the [111] direction and these differ only by the bond orientation to the nearest neighbour. If the atoms in the two groups are different, the structure is known as zinc blende, compound semiconductors such as GaN, GaAs and AlAs, fall into this category [35] and the structure of zinc blende GaN is shown in Figure 1.4.1. The group III–V zinc blende structure is composed of layers of anions, group V, and of cations, group III, the (111) plane is defined with the cation layer uppermost and the $\bar{1}\bar{1}\bar{1}$ plane is when the anion layer is uppermost.

1.4.1.2 Wurtzite.

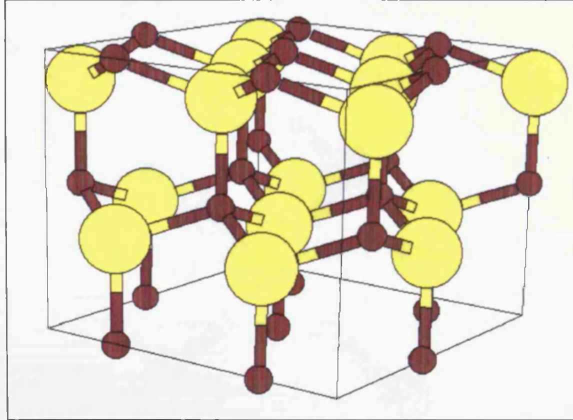

Figure 1.4.2: Gallium (yellow) nitride (brown) wurtzite structure [33].

Wurtzite is a hexagonal close packed structure and consists of two interpenetrating simple hexagonal Bravais lattices. The planes can be described by a set of three Miller indices, as for zinc blende, but it is conventional to use a set of four Miller indices [31]. Hence a plane can be categorized as $(10\bar{1}0)$ or (0001) for example, the fourth index is the intercept on the c–axis and the sum of the first three Miller indices must be zero $\sum_{i=1,3} a_i = 0$. The main difference between wurtzite and zinc blende structures occurs in the stacking sequence of the closest packed diatomic planes. The stacking sequence is ABCABC in the (111) plane for zinc blende and ABABAB in the (0001) plane for wurtzite, where A, B, and C denote the atomic double layer and are the possible sites for densely packed layers [36]. Which is due to a 60 degree rotation in zinc blende and a mirror image but no in-plane rotation with bond angles in wurtzite [3]. The structure of wurtzite can be seen in Figure 1.4.2. Nitride based wurtzite structures demonstrate an appreciable birefringence and optical gain occurs only for the TE mode as a result of their low symmetry [37, 38]. The results discussed in this thesis are for devices with wurtzite structure. GaN is relatively chemically unreactive, with the N–face material being more reactive than the Ga–face material [39], which shown in Figure 1.4.3. The polarity of the crystal, i.e. whether the anion or the cation bonds face the surface,

determines the polarization orientation, most III–nitride devices are grown with cation polarity [40].

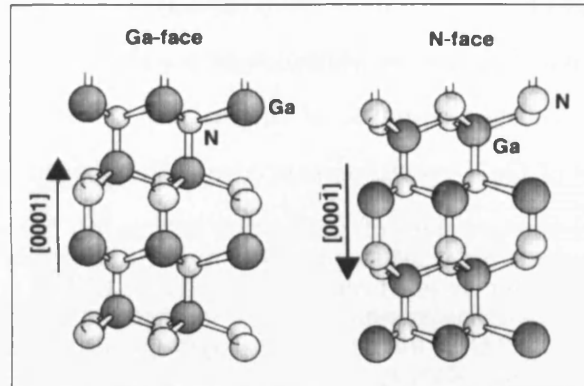

Figure 1.4.3: Ga–face (cation) and N–face (anion) wurtzite structure [41].

1.4.2 Substrate.

One of the basic problems still limiting InGaN device development is the lack of a suitable substrate material. For epitaxial growth, ideally there should be a zero percent lattice mismatch between the substrate and epitaxial materials. This allows crystalline growth of the epitaxial materials without any dislocations (defects), which is important to achieve a reliable, high–power laser. In the epitaxial growth of narrow bandgap II–VI or III–V materials, GaAs is used as a substrate, the lattice mismatch is almost zero and hence they are essentially lattice matched. For the wider bandgap materials such as GaN, this was a serious issue, as a lattice–matched substrate was unavailable. Normally, a single crystal substrate is produced by melting at high temperature a semiconductor crystal such as silicon or GaAs and then letting it cool and coagulate [42]. At the high pressures, 2×10^{19} Pa, and temperatures, 1800°C, needed to produce crystals from the melt [18], GaN evaporates and decomposes. Hence GaN substrates cannot be produced by this method and recently new techniques using vapour phase technology, have been developed [42]. These grow GaN crystal on a substrate made of a material other than GaN, and then the substrate is removed to obtain a GaN single crystal. SiC and sapphire (Al_2O_3)

have been the two most commonly used substrates for III–V nitrides, with the benefits of shared hexagonal symmetry and high temperature stability. The majority of GaN LEDs and laser structures have been grown on sapphire substrates due to cost issues over SiC. The use of Sapphire as a substrate is not completely satisfactory because of a 13.5 % mismatch of the lattices of GaN and sapphire, and hence the early crystals of GaN grown on sapphire suffered from poor quality. Researchers at Nichia solved the problem of the lattice mismatch between the substrate and GaN by creating a buffer layer of aluminium nitride (AlN) on the sapphire substrate before the GaN crystal is formed. This layer prevented crystal dislocations affecting the active region [12], hence devices still work efficiently, despite the large lattice mismatch. Also the cleaving of laser mirrors from GaN based materials grown on sapphire substrates is challenging, because there is a 30° difference in the angle of the cleaved planes of GaN and sapphire [38]. The early successes in the growth of bulk GaN was lead by Porowski at the High Pressure Research Centre based in Poland and more recently research has led to the growth of GaN substrates e.g. Cree [43].

1.4.3 Strain.

In addition to the lattice mismatch between the substrate and epilayer as discussed in section 1.4.2, the impact of which can be reduced by using a buffer layer, there is a lattice mismatch between the well and barrier materials which causes strain. For an InGaN/GaN quantum well device, there are large strains generated due to the lattice differences of InN and GaN of a =3.49 and 3.15 Å respectively. Hence the quantum well region is under biaxial compression, as the larger lattice of InGaN is constrained to that of GaN. For the case of a GaN/AlGaN structure, the quantum well is under tensile strain, due to the smaller lattice constant of 3.08 Å for AlN. The strains affecting these structures are discussed in further detail in sections 2.4 and 4.5. These strains induce an internal field in the structure which has a large effect on the operation and performance of these devices, and this is discussed in

further detail in section 1.4.4 and in chapter 2. If the quantum well exceeds a critical thickness the energy stored will break the bonds and strain will be relieved by dislocations. The devices discussed in this thesis incorporate layers which are sufficiently thin to avoid this and hence strain relaxation can be neglected.

1.4.4 Internal field.

One of the main differences between GaN and other semiconductor material systems is the large internal field present in the well and which will therefore be one of the foci of this thesis. This field can be split into contributions from the piezoelectric and spontaneous fields. The piezoelectric effect was discovered in 1880 by Curie and is the electrical polarization of crystals without a centre of symmetry upon the application of a mechanical force [44, 45]. The inverse piezoelectric effect also exists, applying an electric field causes a change in length of the crystal [46]. A quartz watch contains a piece of vibrating quartz, whose period is accurate to one part per million due to its piezoelectric properties [47]. In addition these structures are pyroelectric and display spontaneous polarization, which is due to the partially filled unit cells at the well–barrier interface. This causes a polarization density even without an external field and wurtzite has the highest symmetry that still displays this property. The piezoelectric field is proportional to the lattice mismatch induced strain discussed in section 1.4.3, and the piezoelectric coefficients of InGaN/GaN based structures, are 10 times larger than other III–V materials and up to 100 times larger than non–ferroelectric piezoelectrics e.g. quartz [48, 49]. Hence, the InGaN/GaN structures discussed in this thesis are dominated by the piezoelectric field, although structures such as GaN/AlGaN have a much larger spontaneous polarization contribution. Hence the spontaneous and piezoelectric components of the internal field must be taken into account when calculating the strained and optical properties of wurtzite structures, and these are discussed in further detail in section 2.

1.5 Applications of gallium nitride.

GaN based structures come under the class of direct wide bandgap semiconductors, with a bandgap of 3.44 eV at room temperature [50, 51], and by alloying with InN and AlN, bandgap energies in the range of 0.8–6.2 eV can be obtained [2]. GaN based materials have high thermal conductivity and breakdown field, with values of 1.3 $Wcm^{-1}K^{-1}$ and 5 $MVcm^{-1}$ respectively, this compares to values of 0.55 $Wcm^{-1}K^{-1}$ and 0.4 $MVcm^{-1}$ for GaAs [52]. Hence GaN based devices have applications in high power, frequency and temperature devices [1, 53]. The development of GaN based blue light emitting diodes and lasers has allowed the whole wavelength range of the visible spectrum to be covered by semiconductor emitters, hence white lighting and full–colour displays are now possible using LEDs [16]. These devices have found commercial markets in a wide range of applications, including printing, lighting, medicine and solar blind detectors to name but a few [16, 20, 54–56]. The following two sections in this chapter go on to cover in further detail, applications in optical data storage (section 1.5.1), and the lighting potential of GaN devices (sections 1.5.2).

1.5.1 Optical storage.

Table 1.5.1: Comparison of optical storage methods [54, 57, 58].

	CD	DVD	Blu–ray
Wavelength (nm)	780	650	400
Colour	Infrared	Red	Blue
Storage (GB)	0.7	4.7	27
Material	AlGaAs	AlGaInP	InGaN
Numerical aperture	0.5	0.6	0.85
Spot size (μm)	0.9	0.5	0.2

The sixfold increase in storage density between a DVD and a CD, was achieved by altering the wavelength of the recording laser and using a lens with a greater ability to gather light and resolve detail (numerical aperture) i.e. a higher numerical

aperture and a shorter wavelength result in a smaller laser spot size. This permits the beam to be focussed with much higher precision and a reduction of the Track pitch. In 2003 the 'Blu–ray' system based on InGaN, which was jointly developed by ten leading consumer electronics companies, was declared as the next industry standard for optical storage [57]. The Blu–ray system has a numerical aperture of 0.85 and a laser wavelength of 400 nm.

Whereas a DVD consists of 0.6 mm disc with 0.6 mm protective coating, a Blu-ray uses a 1.1 mm disc with a protective layer of only 0.1 mm. The recording layer is therefore very close to the surface of the disc and hence is more vulnerable to accidental scratches. As the laser has less material to read through, a higher numerical aperture can be used, a lower track pitch, a smaller pit length and therefore more storage compared to DVD [59]. The relative capabilities and design features of CDs, DVDs and Blu–ray are summarised in table 1.5.1.

1.5.2 LEDs.

Table 1.5.2: Comparison of light bulbs and LEDs for traffic light applications [54].

	Light bulbs	LEDs
Power consumption	70 Watts	20 Watts
Replacement interval	6–12 months	5–10 years
Failure Mode	Sudden total failure	Gradual decrease
Visibility	filter: reflects sunlight	Direct

Previously, indirect bandgap materials e.g. gallium phosphide and silicon carbide were used to produce green and blue LEDs. These devices were often doped to increase recombination via impurities and had quantum efficiencies of 0.02% [60]. The discovery of direct bandgap nitride LEDs in 1995, with quantum efficiencies of 12% [60], made these indirect bandgap devices obsolete [12]. A positive feature is that InGaN LEDs do not contain any toxic elements such as arsenic or phosphorus, and hence are more environmentally friendly [61]. White light can be produced by using LEDs either by combining red, green, and blue LEDs in a cluster device or by

coating a blue InGaN LED with phosphors [62]. These developments have led to bulbs and fluorescent tubes being replaced by white light solid-state devices [16], and the relative benefits of LEDs over light bulbs for use in traffic lights is shown in table 1.5.2. As LEDs use one quarter of the electricity of a conventional light bulb and last ten times longer (filament bulb traffic lights are replaced once a year in Japan, for safety reasons), the potential savings are huge [16].

1.6 Summary.

In this chapter the importance of research into GaN based devices has been described and a brief history and background of GaN based structures has been presented in section 1.3. Some of the more striking differences from conventional III–V materials have been detailed. These concern the structure, both zinc blende and wurtzite and the substrate which were covered in sections 1.4.1 and 1.4.2 respectively. The issues of strain and internal field were briefly introduced in sections 1.4.3 and 1.4.4 respectively and these are discussed in further detail in chapter 2. The general applications of GaN based devices were discussed in section 1.5, with optical storage and LEDs covered at greater length in sections 1.5.1 and 1.5.2 respectively.

1.7 Rationale and outline.

Although commercial devices based on GaN are now available, many of the fundamental parameters remain undefined with any degree of certainty. One of these is the internal field as discussed in section 1.4.4, which is of the order of $MVcm^{-1}$ in InGaN/GaN based devices and has huge effects on all aspects of device operation and performance. By investigation into the internal field, a better understanding and optimisation of these devices can be accomplished. This is achieved by making comparisons between results obtained using a theoretical model originally developed by Chow and Koch [24] and experimental work performed by Pope [63] and Olaizola Izquierdo [64].

In chapter 2, the strain induced piezoelectric and spontaneous polarization fields in InGaN/GaN quantum wells are introduced. The effects of carrier screening at higher carrier densities are discussed and an approximation for this screening is developed.

In chapter 3, the microscopic gain theory developed by Chow and Koch [24] is presented, this is based on the semiconductor Bloch equations, and solved at the level of the screened Hartree–Fock approximation. The many body Coulomb effects, which cause renormalisation of the bandgap and Coulomb enhancement are taken into account.

In chapter 4, material parameters and the contributions to the Pade model are investigated. In addition the developments and adaptations made to permit simulation of InGaN/GaN structures are detailed.

In chapter 5, the internal fields in InGaN/GaN structures are investigated as there are large reported differences between values obtained from theoretical and experimental methods. This is achieved by analysing experiments reported in the literature [65, 66] and those of Pope [63], and includes the development of a valid approximation of the depletion width for these structures. Finally, comparisons of the values of the internal field obtained from the experimental results and from interpolation of the piezoelectric constants of the binaries are made.

In chapter 6, time–resolved photoluminescence experiments performed by Olaizola Izquierdo [64], which display an initial blue–shift of the energy of the peak intensity followed by a subsequent red–shift are presented. Using a theoretical model governed by pumping and recombination processes these results are investigated, permitting further understanding of properties such as the screening of the internal field, carrier lifetimes, dipole matrix element and gain.

Finally in chapter 7 the thesis is concluded with a summary of key results and possible directions for further work.

Chapter 2

Internal field.

2.1 Introduction.

As a result of lattice mismatch between the well and barrier layers InGaN/GaN structures are highly strained and this generates an internal field as first discussed in sections 1.4.3 and 1.4.4, which is of the order of $MVcm^{-1}$ [67, 68]. This skews the well and causes spatial separation of the electron and hole wavefunctions, this is shown in figure 2.1.1 for the case of an ideal square (left) and a skewed (right) quantum well. Even though the energy of the bandgap is the same for a ideal

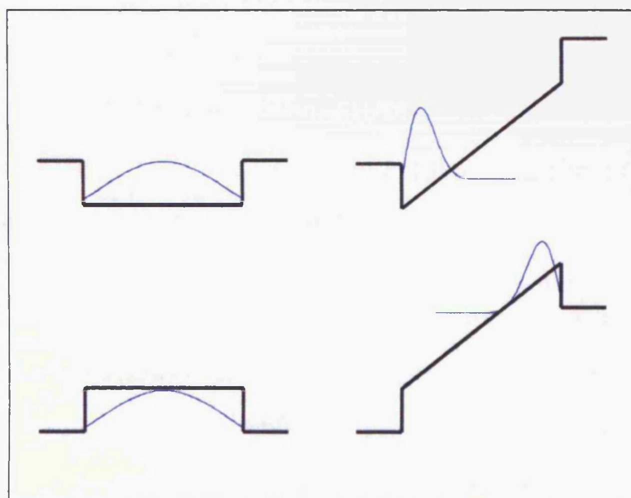

Figure 2.1.1: The well shape and wavefunction for an ideal square (left) and skewed (right) quantum wells.

square and skewed quantum well, the skewed well has a lower transition energy as can be seen in Figure 2.1.1. In addition parity is no longer a good quantum number, as mixing between the confined states has occurred and the ground state contains properties of the second and higher order states. Thus transitions that were forbidden due to parity rules in the square well case, may be observed in the skewed well. The field causes spatial separation of the electron and hole wavefunctions to opposite sides of the quantum well. This reduces the overlap of the electron and hole wavefunctions and hence the interband optical matrix elements [32, 37, 69–72]. The optical gain in these structures is strongly dependent upon the overlap of the electron and hole wavefunctions, hence the internal field has a large effect on the magnitude and spectrum of the gain and this is discussed in more detail in chapter 6.

In this chapter the internal field is discussed in section 2.2, this is composed of spontaneous and piezoelectric fields with are discussed in sections 2.3 and 2.4 respectively. Section 2.5 goes on to look at the screening of the internal field due to charge carriers at high densities and in section 2.6 an approximation for the screening field is derived.

2.2 Internal field.

The total internal field, $E_{int}(0)$, can be written as

$$E_{int}(0) = E_{sp} + E_{pz}, \tag{2.2.1}$$

where E_{sp} and E_{pz} are the spontaneous polarization and piezoelectric fields, which are covered in further detail in sections 2.3 and 2.4 respectively. In addition, there is a carrier dependent screening field which is covered in section 2.5, this is only important at higher carrier densities. For structures under biaxial tensile strain, e.g. GaN/AlGaN, both the spontaneous and the piezoelectric polarizations point in the $(000\bar{1})$ direction, which is from substrate to surface (gallium to nitrogen face). If

the structure is under biaxial compressive strain, e.g. InGaN/GaN, the direction of the piezoelectric polarization is reversed to point in the (0001) direction, hence the spontaneous and the piezoelectric polarization oppose each other [70, 73]. The spontaneous polarisation is much smaller than the piezoelectric field in $In_xGa_{1-x}N/GaN$ structures [4, 48] and the importance and relative contributions of the piezoelectric and spontaneous fields with increasing indium content in $In_xGa_{1-x}N/GaN$ structures are discussed in section 4.5. If the energy stored due to strain is large enough to break the bonds, dislocations develop and strain relaxation will occur, hence the piezoelectric field will tend to zero. From X–ray diffraction intensity experiments, a single layer of 40 nm $In_xGa_{1-x}N/GaN$ for indium fractions in the range of $x = 0 - 0.2$ was found to be fully strained [74–76]. Hence it can be assumed that strain relaxation will not take place in the structures considered in this thesis, which are for narrower wells and smaller indium contents.

2.3 Spontaneous polarization.

A crystal exhibits spontaneous polarization (also know as pyroelectricity) if the primitive cell contains a dipole moment i.e. the positive charge is in a different spatial location to that of the negative charge [30]. The sum of the dipole moments of an infinite crystal is zero as the crystal as a whole is neutral and there is no spontaneous polarization. Whereas in a finite crystal the surface cells are partially filled and therefore charged, the overall polarization is the product of the number of primitive unit cells and the dipole moment. Under normal conditions the dipole moment is masked by neutralising layers of ions which collect on the faces of the crystal. These evaporate upon heating of the crystal and hence the effect was thought to be produced by heat, this is the origin of the name pyro which is Greek for fire [45, 77, 78]. In a quantum well structure the masking effects do not happen because of the growth conditions. The overall spontaneous polarization of a quantum well, E_{sp}, can be written as the difference in the spontaneous polarizations

of the barrier, E_{sp}^{b}, and quantum well, E_{sp}^{q}, layers [40, 79, 80]

$$E_{sp} = E_{sp}^{q} - E_{sp}^{b}. \tag{2.3.1}$$

The wurtzite structure has the highest symmetry that still displays spontaneous polarization, as it lacks a centre of symmetry [48, 81–84]. The direction of polarization depends on the polarity of the crystal, i.e. whether the bonds are from cation to anion sites or visa versa. The accepted convention for the [0001] axis ($c-$direction) is that it points from the anion (N) plane to the cation (Ga) plane, known as N polarity. GaN wurtzite structures under consideration here are grown with the bonds going from gallium to nitrogen along the $c-$direction, hence the spontaneous polarization points in the $[000\bar{1}]$ direction [48, 70].

2.4 Piezoelectric field.

In the epitaxial growth of a thin layer of InGaN on GaN the new layers are constrained to form with the same unit cell as the previous layers and the lattice mismatch between the layers of different composition causes stress and strain to occur. The lattice constant of InN is larger than GaN, so as the indium content increases, the compressive strain within a InGaN quantum well increases [85]. As discussed in section 1.4.4, the strain displaces the positive and negative charge centers by different amounts creating dipoles, and the nonuniform charge distribution within the unit cell of the crystal induces the piezoelectric field [40, 47, 86–88]. For a quantum well, the growth can be assumed to be pseudomorphic, so the structure is isotropic in the basal $x-y$ plane i.e. the strains in the x and y planes are equal, $e_{xx} = e_{yy}$ [67]. For the case of a quantum well, the strain can be written as the

difference in the lattice constants for the well and barrier material [89]

$$\begin{aligned} e_{xx} &= e_{yy} \\ &= \frac{a_b - a_q}{a_q} \qquad (2.4.1) \\ e_{zz} &= \frac{c_b - c_q}{c_q}, \qquad (2.4.2) \end{aligned}$$

where the lattice constants are a in the x and y directions and c in the z direction, respectively. If the strains are too large or the well width exceeds a critical thickness, strain relaxation occurs by the formation of crystal dislocations [8], which severely degrades the optical quality and the piezoelectric field tends to zero [12, 80]. The critical thickness of $In_xGa_{1-x}N$ for $x < 0.15$ has been reported to be larger than 40 nm [82]. Hence, in sufficiently thin quantum wells the strain arising from lattice mismatch can be accommodated elastically, as long as the energy stored is insufficient to create dislocations [18]. In the case of a quantum well device with thin wells and relatively wide barriers, it is valid to assume that the barriers are unstrained as strain relaxation has taken place and that the well is strained due to the lattice mismatch between the well and barrier [79].

Using Hooke's law the relationship between the applied stress, σ_{ij}, and the strain, e_{kl}, can be described using

$$\sigma_{ij} = \sum_{k,l} C_{ijkl} e_{kl}, \qquad (2.4.3)$$

where C_{ijkl} are the elastic stiffness constants [8, 73]. The subscripts i and j indicate the direction of the piezoelectric field and strain respectively, where j=1–3 and j=4–6 corresponds to strain and shear strain respectively, see figure 2.4.1 [46]. As a consequence of spatial symmetry, Voigt notation can be used to reduce the fourth

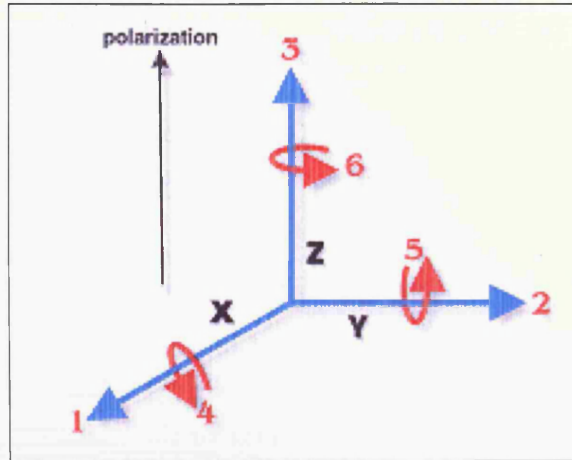

Figure 2.4.1: Directions of strain (1–3) and shear strain (4–6) [46].

rank tensor of C_{ijkl} to a 6×6 matrix [73]. Thus, by applying the mapping [30, 45]

$$\begin{aligned} xx &\rightarrow 1 \qquad yz, zy \rightarrow 4 \\ yy &\rightarrow 2 \qquad zx, xz \rightarrow 5 \\ zz &\rightarrow 3 \qquad xy, yx \rightarrow 6, \end{aligned} \tag{2.4.4}$$

allows Hooke's law to be simplified to [90]

$$\sigma_i = \sum_j C_{ij} e_j. \tag{2.4.5}$$

As the stiffness matrix is symmetric, $C_{ij} = C_{ji}$, the maximum number of independent values for the elastic stiffness constants is 21, and the 6×6 matrix for wurtzite

structures can be rewritten as [30, 73]

$$\begin{bmatrix} \sigma_{xx} \\ \sigma_{yy} \\ \sigma_{zz} \\ \sigma_{xy} \\ \sigma_{yz} \\ \sigma_{zx} \end{bmatrix} = \begin{bmatrix} C_{11} & C_{12} & C_{13} & 0 & 0 & 0 \\ C_{12} & C_{22} & C_{13} & 0 & 0 & 0 \\ C_{13} & C_{13} & C_{33} & 0 & 0 & 0 \\ 0 & 0 & 0 & C_{44} & 0 & 0 \\ 0 & 0 & 0 & 0 & C_{55} & 0 \\ 0 & 0 & 0 & 0 & 0 & \frac{C_{11}-C_{12}}{2} \end{bmatrix} \begin{bmatrix} e_{xx} \\ e_{yy} \\ e_{zz} \\ e_{xy} \\ e_{yz} \\ e_{zx} \end{bmatrix}. \quad (2.4.6)$$

The crystal is biaxially strained in the (0001) plane ($x-y$ direction) and it expands and contracts in the [0001] direction (z direction), hence, $\sigma_{xx} = \sigma_{yy}$ and $\sigma_{zz} = 0$, and the shear stresses can be assumed to be negligible [73]. Hence using equation 2.4.6, the stress in the x, y and z directions can be written as

$$\sigma_{xx} = C_{11}e_{xx} + C_{12}e_{yy} + C_{13}e_{zz} \quad (2.4.7)$$

$$\sigma_{yy} = C_{12}e_{xx} + C_{22}e_{yy} + C_{13}e_{zz} \quad (2.4.8)$$

$$\sigma_{zz} = C_{13}e_{xx} + C_{13}e_{yy} + C_{33}e_{zz} = 0, \quad (2.4.9)$$

where the strains in the x and y directions are the same, $e_{xx} = e_{yy}$. By rearranging equation 2.4.9, the strain in the z direction, e_{zz}, can be written in terms of strain in the x direction, e_{xx}, as [8]

$$\begin{aligned} e_{zz} &= -\frac{C_{13}}{C_{33}}(e_{xx} + e_{yy}) \\ &= -2\frac{C_{13}}{C_{33}}e_{xx}. \end{aligned} \quad (2.4.10)$$

This contains Poisson's ratio, ν, which is the dimensionless ratio of transverse strain to longitudinal strain [73, 89, 91, 92]

$$\nu = -\frac{e_{zz}}{e_{xx}} = 2\frac{C_{13}}{C_{33}}. \quad (2.4.11)$$

The stresses in the x and y directions are the same, $\sigma_{xx} = \sigma_{yy}$, and by substitution of equation 2.4.10, the stress in the x plane, equation 2.4.7, can be rewritten as

$$\sigma_{xx} = e_{xx}[C_{11} + C_{12} - 2\frac{C_{13}^2}{C_{33}}]. \quad (2.4.12)$$

The values for the elastic stiffness constants, C_{ij}, are always positive, as a material under uniaxial tension gets longer [92].

The piezoelectric polarization can be written in terms of stress as [45, 51]

$$P_{pz}^i = \sum d_{ij}\sigma_{ij} \quad (2.4.13)$$

where the d_{ij} terms are the piezoelectric coefficients. As a result of the symmetry relations between the piezoelectric moduli, $d_{31} = d_{32}$, $d_{33} \neq 0$, $d_{15} = d_{24}$ and for all other components $d_{ij} = 0$. Hence equation 2.4.13, can be written as [73, 81, 93]

$$P_{pz}^x = \frac{1}{2}d_{15}\sigma_{xy} \quad (2.4.14)$$

$$P_{pz}^y = \frac{1}{2}d_{15}\sigma_{xy} \quad (2.4.15)$$

$$P_{pz}^z = d_{31}\sigma_{xx} + d_{31}\sigma_{yy} + d_{33}\sigma_{zz}, \quad (2.4.16)$$

for the x, y and z directions respectively. For biaxial stress, $\sigma_{xx} = \sigma_{yy}$ and $\sigma_{zz} = 0$, also the shear stresses can be assumed to be negligible. Thus the piezoelectric polarization has only one non–zero component, which can be written as

$$P_{pz}^z = 2d_{31}\sigma_{xx}. \quad (2.4.17)$$

The piezoelectric field can be written in terms of the piezoelectric polarization as

$$E_{pz}^i = P_{pz}^i\frac{e}{\epsilon_0\epsilon_r}, \quad (2.4.18)$$

where ϵ_0 and ϵ_r are the dielectric constants for free space and the medium respectively (assumed to be constant in all directions and independent of strain). Hence

the direction of the piezoelectric polarization is dependent upon the type of strain on the quantum well, compressive ($\sigma < 0$) and tensile ($\sigma > 0$) strain result in positive and negative piezoelectric fields respectively [87].

By substitution of equation 2.4.17, for the piezoelectric polarization into equation 2.4.18, the piezoelectric field in the z direction can be written as

$$E_{pz} = \frac{2e}{\epsilon_0 \epsilon_r} d_{31} \sigma_{xx}, \tag{2.4.19}$$

and by substitution of equation 2.4.7, this can be rewritten as

$$E_{pz} = \frac{2e}{\epsilon_0 \epsilon_r} e_{xx} d_{31} [C_{11} + C_{12} - 2\frac{C_{13}^2}{C_{33}}]. \tag{2.4.20}$$

2.5 Screening of the internal field.

The internal field, as discussed in section 2, has contributions from the spontaneous polarization and piezoelectric fields which were covered in sections 2.3 and 2.4, respectively. This field skews the quantum well, hence it is no longer square and the distribution of electrons and holes becomes spatially separated. This separation of charge creates a density dependent screening field, $E_{\text{scr}}(N, z)$, this results in a smaller effective internal field, $E_{int}(N, z)$, which can be written as

$$\begin{aligned} E_{int}(N, z) &= E_{int}(0) + E_{\text{scr}}(N, z) \\ &= E_{sp} + E_{pz} + E_{\text{scr}}(N, z). \end{aligned} \tag{2.5.1}$$

Hence, $E_{int}(0)$, which is given by equation 2.2.1, is only valid for the low density situation. The screening field can be calculated from the combined electron and hole distributions in the well [94], using Poisson's equation and integrating the charge density, $\rho(z)$, over all space. Carriers in the well have a probability distribution in the $z-$direction given by the square of their respective normalised envelope functions, $u_e(z)$ and $u_h(z)$ respectively. In the presence of an electric field these functions are displaced across the well and, assuming overall charge neutrality in

the well, then the net charge density distribution, $\rho(N, z)$, across the well is given by [95]

$$\rho(N, z) = -eN \left[|U_e(z)|^2 - |U_h(z)|^2\right], \tag{2.5.2}$$

where N is the carrier density and $U_e(z)$ and $U_h(z)$ are the spatial carrier distributions. Poisson's equation is given by

$$\frac{\mathrm{d}^2\phi}{\mathrm{d}z^2} = -\frac{\rho(z)}{\epsilon_b(z)}, \tag{2.5.3}$$

and by substitution of this into equation 2.5.2 and integrating gives the screening field as

$$E_{\mathrm{scr}}(N, z) = \frac{eN}{2\epsilon_b} \int_{-\infty}^{\infty} \mathrm{d}z \left[|U_e(z)|^2 - |U_h(z)|^2\right], \tag{2.5.4}$$

where it is assumed that the dielectric constant, ϵ, is independent of z. Approximations to this screening field are discussed in the following section.

2.6 Average screening of the internal field.

As discussed in section 2.5, the $z-$dependent screening field, $E_{\mathrm{scr}}(N, z)$, for a quantum well is given by equation 2.5.4. This was calculated from the combined electron and hole distribution in the well [94], using Poisson's equation and integrating the charge density, $\rho(z)$, over all space. Unfortunately, the method used to calculate the gain detailed in Chapter 3, cannot take the $z-$dependence of the screening field into account. To remove the $z-$dependence of the screening field, the average value which is constant across the well is used. This is found by integrating the screening field, $E_{\mathrm{scr}}(N, z)$, over the well width, to obtain the screening potential, $\phi(N)$, which can be written as

$$\phi(N) = \frac{eN}{\epsilon_b} \int_0^{L_w} \int_{-\infty}^{\infty} \left[|U_e(z)|^2 - |U_h(z)|^2\right] \mathrm{d}^2z. \tag{2.6.1}$$

by dividing by the well width, L_w, the average screening field $E_{\mathrm{scr}}(N)$ across the well (no $z-$dependence) can be written as

$$E_{\mathrm{scr}}(N) = \frac{eN}{\epsilon_b L_w} \int_0^{L_w} \mathrm{d}z_0 \int_{-\infty}^{\infty} \mathrm{d}z \left[|U_e(z)|^2 - |U_h(z)|^2 \right]. \qquad (2.6.2)$$

In this work, the centre of the well is defined at $z = 0$, hence a sign dependency of the integral is introduced and equation 2.6.2 can be rewritten as

$$\begin{aligned} E_{\mathrm{scr}}(N) = \quad & \frac{eN}{2\epsilon_b L_w} \int_{-\frac{L_w}{2}}^{\frac{L_w}{2}} \mathrm{d}z_0 & (2.6.3) \\ \times & \left(- \int_{-\infty}^{z_0} \left[|U_e(z)|^2 - |U_h(z)|^2 \right] \mathrm{d}z \right. \\ & \left. + \int_{\infty}^{z_0} \left[|U_e(z)|^2 - |U_h(z)|^2 \right] \mathrm{d}z \right), & (2.6.4) \end{aligned}$$

this can be simplified by combining the last two terms, to give

$$E_{\mathrm{scr}}(N) = \frac{eN}{2\epsilon_b L_w} \int_{\frac{-L_w}{2}}^{\frac{L_w}{2}} \mathrm{d}z_0 \int_{-\infty}^{\infty} \mathrm{d}z \left[|U_e(z)|^2 - |U_h(z)|^2 \right] \frac{z - z_0}{|z - z_0|}. \qquad (2.6.5)$$

2.7 Summary.

In this chapter the origin and effects of the internal field have been covered. The two components of spontaneous and piezoelectric polarization and the screening effects at high carrier density have been discussed and a average screening approximation was developed. In chapter 4 the effect of the screening approximation is discussed in further detail. In chapters 5 and 6, work is presented on the measurement and screening of the internal field.

Chapter 3

Pade model.

3.1 Introduction.

In this chapter, the modelling of gain in semiconductor lasers is discussed and is based on the work of Chow and Koch [24]. This theory is used to model the experimental results which are presented in chapters 4–6. In section 3.2, the gain in terms of macroscopic and microscopic polarisation is introduced. In section 3.3, an equation for gain is developed at the level of the Pade approximation, with contributions from the kinetic, free carrier and Coulomb terms. At high carrier densities, the Coulomb potential is reduced by screening and this is discussed in section 3.4 The overall effects of bandgap renormalisation are discussed in section 3.5, with the Debye and Exchange contributions detailed in sections 3.5.1 and 3.5.2 respectively.

3.2 Gain.

From Maxwell's equations the gain, g, experienced by a plane wave optical field is

$$g = \frac{\nu}{\epsilon_0 ncE(z)} \mathrm{Im}(P(z)) \tag{3.2.1}$$

where $E(z)$, $P(z)$, n and c are the laser field, polarisation, refractive index and the speed of light respectively. The polarisation, $P(z)$, can be written in the form of a

simple plane wave as

$$P(z) = 2P(z,t)e^{-i[Kz-\nu t-\phi(z)]}. \tag{3.2.2}$$

In a semiconductor gain medium the electron–electron collisions and the electron–hole pair number must be taken into account, this can be done by using the second quantised or Fock representation. Electron–electron collisions result in direct or exchange scattering, which are experimentally indistinguishable and cause reversal of the scattering amplitude. Electron–hole pairs can be created or annihilated, hence their number is not conserved. Because of the collisions and the recombination processes, it is not possible to have a precise knowledge of the state vector of the system. Hence, electrons and holes are not in pure states described by wavefunctions but rather in mixed states best described by density operators, which contain the quantum statistical properties of the particles [96].

The time dependent polarisation can be written in terms of the expectation value of the polarisation operator as

$$P(z,t) = \langle P \rangle \tag{3.2.3}$$

assuming that there is a dipole interaction between the laser field and carriers, the polarisation operator can be written as

$$P = \frac{1}{V}\sum_k (\mu_k a_k^\dagger b_{-k}^\dagger + \mu_k^* b_{-k} a_k), \tag{3.2.4}$$

where μ_k is the dipole matrix element between the valence and conduction band.

Hence the polarisation which appears in equation 3.2.1 can be written as

$$P(z) = 2e^{-i[Kz-\nu t-\phi(z)]}\frac{1}{V}\sum \mu_k^* p_k. \tag{3.2.5}$$

where p_k is the microscopic polarisation which can be written as

$$p_k = \langle b^\dagger_{-k} a_k \rangle. \tag{3.2.6}$$

Likewise the electron and hole occupation numbers can be written as

$$n_{ek} = \langle a^\dagger_k a_k \rangle \tag{3.2.7}$$

$$n_{hk} = \langle b^\dagger_{-k} b_{-k} \rangle, \tag{3.2.8}$$

where the annihilation operator and its Hermitean adjoint the creation operator are given by a_k and $a^\dagger_k$ for electrons, and $b^\dagger_{-k}$ and b_{-k} for holes respectively. The polarisation is obtained by the integral of the rate of change with time and in the Heisenberg picture, the equation of motion is obeyed by any operator Θ_k

$$\frac{\mathrm{d}\Theta_k}{\mathrm{d}t} = \frac{i}{\hbar}[H_k, \Theta_k], \tag{3.2.9}$$

this can be rewritten for the specific case of the microscopic polarisation as

$$\frac{\mathrm{d}p_k}{\mathrm{d}t} = \frac{i}{\hbar}[H_k, p_k], \tag{3.2.10}$$

where the Hamiltonian for an interacting system can be expanded as

$$H = H_{kin} + H_{c-f} + H_C. \tag{3.2.11}$$

where H_{kin}, H_{c-f} and H_C are contributions from the kinetic, free carrier and Coulomb terms respectively and these are derived in sections 3.2.1–3.2.3. Hence by calculation of the microscopic polarisation the gain in semiconductor lasers can be obtained.

3.2.1 Hamiltonian: Kinetic energy

In this section the kinetic energy contribution to the Hamiltonian discussed in section 3.2 is derived. For the case of non–interacting electrons the kinetic energy part of the Hamiltonian can be written as

$$H_{kin} = -\int \psi^{\dagger}(r)\left(\frac{\hbar^2\nabla^2}{2m_\lambda}\right)\psi(r)\mathrm{d}^3r, \tag{3.2.12}$$

where the electron field operator, $\hat{\psi}(r)$, can be written as

$$\hat{\psi}(r) = \sum_{\lambda}\sum_{k}\sum_{s_z} a_{\lambda k s_z}\psi_{\lambda k s_z}(r), \tag{3.2.13}$$

where an electron has the annihilation operator $a_{\lambda k s_z}$ and single particle eigenfunction $\psi_{\lambda k s_z}(r)$. The indices λ, k and s_z define the band, momentum and z–component of spin respectively. Hence the kinetic energy Hamiltonian H_{kin} for non–interacting electrons can be written as

$$H_{kin} = \sum_{\lambda}\sum_{k}\sum_{Sz} \epsilon_{\lambda k} a^{\dagger}_{\lambda k s_z} a_{\lambda k s_z}. \tag{3.2.14}$$

Restricting the summation to the two band approximation gives

$$H_{kin} = \sum_{k}\sum_{s_z}(\epsilon_{ck} a^{\dagger}_{cks_z} a_{cks_z} + \epsilon_{vk} a^{\dagger}_{vks_z} a_{vks_z}) \tag{3.2.15}$$

and using the hole creation and annihilation operators

$$b^{\dagger}_{-k,-s_z} = a_{vks_z} \tag{3.2.16}$$

$$b_{-k,-s_z} = a^{\dagger}_{vks_z}, \tag{3.2.17}$$

this can be rewritten as

$$H_{kin} = \sum_{k}\sum_{s_z}\left[\epsilon_{ck} a^{\dagger}_{ks_z} a_{ks_z} + \epsilon_{vk}(1 - b^{\dagger}_{-k,-s_z} b_{-k,-s_z})\right], \tag{3.2.18}$$

in the electron hole representation. As the point of zero energy is arbitrary, the constant term, $\sum_{ks_z} \epsilon_{vk}$, can be omitted.

For the simple case of a system in which the dopant atoms, thermal energy and pumping processes are neglected, the valence band is full and the conduction band empty. Using the *effective mass approximation* the bands can be approximated to a parabola in the region of small k. Thus the $\epsilon_{\alpha k}$ terms in equation 3.2.18 can be expressed as

$$\epsilon_{ck} = \frac{\hbar^2 k^2}{2m_c} + \epsilon_{g0} \quad (3.2.19)$$

$$\epsilon_{vk} = \frac{\hbar^2 k^2}{2m_v}, \quad (3.2.20)$$

where m_c and m_v are the effective masses of electrons in the conduction and valence bands respectively and ϵ_{g0} is the unrenormalised bandgap energy.

Making the assumption that the electrons are noninteracting, the effective masses are given by $m_c = m_e$ and $m_v = -m_h$, hence the kinetic energy Hamiltonian can be written as

$$H_{kin} = \sum_k \left[\left(\frac{\hbar^2 k^2}{2m_e} + \epsilon_{g0} \right) a_k^\dagger a_k + \frac{\hbar^2 k^2}{2m_h} b_{-k}^\dagger b_{-k} \right]. \quad (3.2.21)$$

When Coulomb interactions are taken into account, as discussed in section 3.3, the relationship between m_v and m_h takes on a more complex form.

3.2.2 Hamiltonian: Free carrier.

In this section the free carrier contribution to the Hamiltonian is derived, which is the second term in equation 3.2.11 and is the electric–dipole interaction. Taking into account the coupling between the optical field and the polarisation, P, the electric–dipole interaction, H_{c-f}, can be written as

$$H_{c-f} = -VP.E, \quad (3.2.22)$$

where V is the volume of the active region. By substitution of equation 3.2.4 for the polarisation the free carrier Hamiltonian can be written as

$$H_{c-f} = -\sum_k (\mu_k a_k^\dagger b_{-k}^\dagger + \mu_k^* b_{-k} a_k) E(z,t). \tag{3.2.23}$$

3.2.3 Hamiltonian: Coulomb.

The Coulomb attraction between electrons in the conduction band and holes in the valence band, tends to keep them in the vicinity of each other and increases with bandgap [12]. This results in an increase of the radiative recombination, and an enhancement of the gain and spontaneous emission [97]. As a result of the Pauli principle, electrons in the same or adjacent atoms are coupled by the exchange effect. Two types of state can be constructed, which depend on the spin of the electron, these are symmetric (anti–parallel spins: singlet state) and antisymmetric (parallel spins: triplet state) combinations. Calculating the average of the Coulomb energy of these two states, the difference can be written as [98]

$$H_C = \int\int \mathrm{d}r_1 \mathrm{d}r_2 \hat{\psi}_b^\dagger(r_2) \hat{\psi}_a^\dagger(r_1) \frac{e^2}{\epsilon_b |r_1 - r_2|} \hat{\psi}_b(r_1) \hat{\psi}_a(r_2). \tag{3.2.24}$$

expanding the electron field operator using equation 3.2.13, allows the interaction energy to be rewritten as [99]

$$H_C = \frac{1}{2} \sum_{k,k'} \sum_{q \neq 0} V_q (a_{c,k+q}^\dagger a_{c,k'-q}^\dagger a_{ck'} a_{ck} + a_{v,k+q}^\dagger a_{v,k'-q}^\dagger a_{vk'} a_{vk} + 2a_{c,k+q}^\dagger a_{v,k'-q}^\dagger a_{vk'} a_{ck}). \tag{3.2.25}$$

This expansion is based upon the two band approximation and Coulomb induced interband transitions are neglected. Also it uses the fact that Coulomb scattering does not alter the spin orientation and that $q = 0$ contributions are cancelled by the electron–ion and ion–ion Coulomb interaction. Using the electron–hole representation, given by equations 3.2.16 and 3.2.17, the Coulomb contribution to the

Hamiltonian can be written as

$$H_C = \frac{1}{2}\sum_{k,k'}\sum_{q\neq 0} V_q(a^{\dagger}_{k+q}a^{\dagger}_{k'-q}a_{k'}a_k + b^{\dagger}_{k+q}b^{\dagger}_{k'-q}b_{k'}b_k - 2a^{\dagger}_{k+q}b^{\dagger}_{k'-q}b_{k'}a_k) \tag{3.2.26}$$

where constant terms, which cause a shift of the reference energy, have been dropped. The bare Coulomb potential energy, V_q, can be written as [100]

$$\begin{aligned} V_q &= \int \mathrm{d}^2 r e^{-iq.r}\frac{e^2}{\epsilon_b r} \\ &= \frac{2\pi e^2}{\epsilon_b A q}, \end{aligned} \tag{3.2.27}$$

the effects of screening on the Coulomb potential is detailed in section 3.4.

3.3 Pade model.

In this section the equation for gain is derived at the level of the Pade approximation with contributions from kinetic, free carrier and Coulomb effects. Starting with the Hamiltonian for an interacting system given by equation 3.2.11 and substituting in equations 3.2.21, 3.2.23 and 3.2.26 gives

$$\begin{aligned} H = &+ \sum_k \left[(\epsilon_{ek} + \epsilon_{g0})a^{\dagger}_k a_k + \epsilon_{hk} b^{\dagger}_{-k} b_{-k}\right] \\ &- \sum_k (\mu_k a^{\dagger}_k b^{\dagger}_{-k} + \mu^*_k b_{-k} a_k) E(z,t) \\ &+ \frac{1}{2}\sum_{k,k'}\sum_{q\neq 0} V_q(a^{\dagger}_{k+q}a^{\dagger}_{k'-q}a_{k'}a_k + b^{\dagger}_{k+q}b^{\dagger}_{k'-q}b_{k'}b_k - 2a^{\dagger}_{k+q}b^{\dagger}_{k'-q}b_{k'}a_k). \end{aligned} \tag{3.3.1}$$

The energies can be approximated using the effective mass theory, which is based on the assumption that the bands are parabolic in the vicinity of the extrema [99].

Hence, the kinetic energy terms which appear in equation 3.3.1 can be written as

$$\epsilon_{ek} = \frac{\hbar^2 k^2}{2m_e} \tag{3.3.2}$$

$$\begin{aligned}\epsilon_{hk} &= -\epsilon_{vk} + \sum_{q\neq 0} V_q \\ &= \frac{\hbar^2 k^2}{2m_h}\end{aligned} \tag{3.3.3}$$

and by comparison with equations 3.2.19 and 3.2.20 for the free carrier result, it can be seen that the hole effective mass includes the Coulomb energy of the full valence band. This originates from the replacement of valence band electron operators by hole operators in the interaction term of equation 3.2.25.

Reducing the commutators in the Heisenberg equations, allows the interband polarisation, p_k, to be written as

$$\begin{aligned}\frac{\mathrm{d}p_k}{\mathrm{d}t} = &- i\omega_k' p_k - \frac{i}{\hbar}\mu_k E(z,t)(n_{ek} + n_{hk} - 1) \\ &+ \frac{i}{\hbar}\sum_{k',q=0} V_q \Big(\langle a^\dagger_{k'+q} b_{-k} a_{k'} a_{k+q}\rangle + \langle b^\dagger_{k'-q} b_{k'} a_k b_{-k-q}\rangle \\ &- \langle a^\dagger_{k'+q} b_{-k+q} a_{k'} a_k\rangle - \langle b^\dagger_{k'-q} b_{-k} b_{k'} a_{k-q}\rangle + \langle b^\dagger_{-k+q} a_{k-q}\delta_{k,k'}\rangle \Big) .\end{aligned} \tag{3.3.4}$$

Equation 3.3.4, includes couplings to higher–order correlation due to Coulomb interaction. By the use of projection–operator techniques, the four–operator expectation values can be factorized into the products of two operator expectation values, thus the two–operator combination AB, can be written as [99]

$$\begin{aligned}\frac{\mathrm{d}}{\mathrm{d}t}\langle AB\rangle &= \frac{\mathrm{d}}{\mathrm{d}t}\langle AB\rangle_{HF} + \left(\frac{\mathrm{d}}{\mathrm{d}t}\langle AB\rangle - \frac{\mathrm{d}}{\mathrm{d}t}\langle AB\rangle_{HF}\right) \\ &= \frac{\mathrm{d}}{\mathrm{d}t}\langle AB\rangle_{HF} + \frac{\mathrm{d}}{\mathrm{d}t}\langle AB\rangle_{col},\end{aligned} \tag{3.3.5}$$

these correspond to the 'coherent' or Hartree–Fock and the 'scattering' contributions, respectively. Using this factorizing method and adding the contributions

beyond Hartree–Fock, the *semiconductor Bloch equation* is obtained

$$\frac{\mathrm{d}p_k}{\mathrm{d}t} = -i\omega_k p_k - i\Omega_k(z,t)(n_{ek} + n_{hk} - 1) - \gamma p_k. \tag{3.3.6}$$

There are two many–body contributions to the Hartree–Fock equations, which are manifested in a renormalisation of the transition and electric–dipole interaction energies and are known as the exchange shift and the Coulomb field renormalisation respectively. These are given by

$$\hbar\omega_k = \hbar\omega'_k - \sum_{k' \neq k} V_{|k-k'|}(n_{ek'} + n_{hk'}) \tag{3.3.7}$$

and

$$\Omega_k(z,t) = \frac{\mu_k E(z,t)}{\hbar} + \frac{1}{\hbar}\sum_{k' \neq k} V_{|k-k'|} p_{k'}, \tag{3.3.8}$$

respectively, where the Coulomb terms are proportional to $V_{|k-k'|}$, similar discussions can be found in [77, 101, 102]. These Coulomb renormalisation effects are discussed in further detail in section 3.5.

To include the plasma screening effects between the charged particles, the bare potential, V_q, is replaced by a screened potential, V_{sq}, which has a reduced interaction strength especially at long distances [99], this is discussed in further detail in section 3.4. Using the product rule and multiplying by $e^{(i\omega_k+\gamma)t}$ equation 3.3.6 can be simplified to

$$\frac{\mathrm{d}}{\mathrm{d}t}(p_k e^{(i\omega_k+\gamma)t}) = -i\Omega_k(z,t)(n_{ek} + n_{hk} - 1)e^{(i\omega_k+\gamma)t} \tag{3.3.9}$$

and integrating gives the induced dipole as

$$p_k(t) = i\int_{-\infty}^{t} \mathrm{d}t' e^{(i\omega_k+\gamma)(t'-t)}\Omega_k(z,t')[n_{ek}(t') + n_{hk}(t') - 1]. \tag{3.3.10}$$

Under the *rate equation approximation*, it is assumed that the total carrier density, N, and the electric field envelope, E, vary little in the dipole lifetime, $\frac{1}{\gamma}$, hence

they can be removed from the integral and replaced with their value at time t. By substitution of the electric field, equation 3.3.10 can be rewritten as

$$\begin{aligned} p_k(t) = & - \frac{i\mu_k}{2\hbar}E(z)[n_{ek}(t)+n_{hk}(t)-1]\left(\frac{e^{i[Kz-\nu t-\phi(z)]}}{i(\omega_k-\nu)+\gamma}+\frac{e^{-i[Kz-\nu t-\phi(z)]}}{i(\omega_k+\nu)+\gamma}\right) \\ & - \frac{i}{\hbar}[n_{ek}(t)+n_{hk}(t)-1]\sum_{k'\neq k} V_{|k-k'|}\int_{-\infty}^{t} \mathrm{d}t' e^{(i\omega_k+\gamma)(t'-t)} p_{k'}. \end{aligned} \quad (3.3.11)$$

The $e^{-i[\ldots]}$ term rotates on a very small time scale compared to the $e^{i[\ldots]}$ term, thus using the *rotating wave approximation* (RWA) it can be averaged to zero and equation 3.3.11 simplifies to

$$\begin{aligned} p_k(t) = & - \frac{i}{\hbar}[n_{ek}(t)+n_{hk}(t)-1] \quad (3.3.12) \\ & \times \left[\frac{1}{2}\mu_k E(z)\frac{e^{i[Kz-\nu t-\phi(z)]}}{i(\omega_k-\nu)+\gamma}+\sum V_{s,|k-k'|}\int_{-\infty}^{t}\mathrm{d}t' e^{(i\omega_k+\gamma)(t'-t)}p_k(t')\right]. \end{aligned}$$

This can be solved by summing over the powers of the screened Coulomb interaction energy, $V_{s,|k-k'|}$, to give

$$p_k(t) = \sum_i p_k^{(i)}(t). \quad (3.3.13)$$

The lowest order free carrier result is found by setting $V_{s,|k-k'|} = 0$, which gives

$$p_k^{(0)}(t) = \frac{1}{2}E(z)e^{i[Kz-\nu t-\phi(z)]}\chi_k^{(0)} \quad (3.3.14)$$

and the first order result can be found using a similar method to give

$$p_k^{(1)}(t) = \frac{1}{2}E(z)e^{i[Kz-\nu t-\phi(z)]}\chi_k^{(0)}q(k). \quad (3.3.15)$$

Where the susceptibility function is given by

$$\chi_k^{(0)} = -\frac{i\mu_k}{\hbar}\frac{n_{ek}+n_{hk}-1}{i(\omega_k-\nu)+\gamma} \quad (3.3.16)$$

and the complex dimensionless factor, $q(k)$, is given by

$$q(k) = \frac{1}{\mu_k} \sum V_{s,|k-k'|} \chi_{k'}^{(0)}. \tag{3.3.17}$$

This process can be applied indefinitely until the required accuracy is obtained, but as the equation does not quickly converge there is no benefit in using the higher–order results. Hence the Pade approximation which limits the summation to the first two terms in the geometrical series is used. Thus the induced dipole (equation 3.3.12) is the sum of the zero and first order terms, given by equations 3.3.14 and 3.3.15 respectively and can be written as

$$\begin{aligned} p_k(t) &\simeq p_k^{(0)}(t) + p_k^{(1)}(t) \\ &\simeq \frac{1}{2} E(z) e^{i[Kz - \nu t - \phi(z)]} \frac{\chi_k^{(0)}}{1 - q(k)}. \end{aligned} \tag{3.3.18}$$

This can be substituted into equation 3.2.5, to give the polarisation

$$P(z) = -\frac{E(z)}{w} \sum_k \frac{\mu_k \chi_k^{(0)}}{1 - q(k)}, \tag{3.3.19}$$

Using the lineshape function given by

$$L(\omega_k - \nu) = \frac{\gamma^2}{\gamma^2 + (\omega_k - \nu)^2} \tag{3.3.20}$$

and equation 3.3.16 the polarisation can be rewritten as

$$P(z) = -\frac{iE(z)}{\hbar w \gamma} \sum_k \frac{|\mu_k|^2}{1 - q(k)} [n_{ek} + n_{hk} - 1] \left(1 - i\frac{\omega_k - \nu}{\gamma}\right) L(\omega_k - \nu), \tag{3.3.21}$$

Taking the imaginary part of the polarisation, converting the summation to an integral and using equation 3.2.1, gives the material gain as

$$g = \frac{\nu}{2\pi \epsilon_0 n c \hbar \omega \gamma} \int_0^\infty k |\mu_k|^2 [n_{ek} + n_{hk} - 1] \frac{L(\omega - \nu)}{1 - q(k)} \mathrm{d}k. \tag{3.3.22}$$

3.4 Screening of the Coulomb potential.

One of the most important many–body interactions is the phenomenon of screening. Plasma screening is the carrier density dependent weakening of the Coulomb interaction potential due to the presence of background charge carriers, i.e. the range of the Coulomb interaction decreases with increasing the carrier density. More specifically, the dielectric function increases with increasing plasma density. The semiconductor Bloch equations are solved at the level of the screened Hartree–Fock approximation, by the use a simplified form of the Lindhard formula to model for the plasma screening. The effects of plasma screening are included by replacement of the bare Coulomb potential, V_q, which appears in equation 3.2.25, with the screened Coulomb potential, V_{sq} [103]. The problem is simplified by assuming that the screening from the electron–hole plasma ensemble, can be approximated by the sum of the individual electron and hole plasmas. In narrow bandgap semiconductors, the many–body effects are not as pronounced, as the Coulomb forces are strongly screened, but as the bandgap increases, the screening of the Coulomb forces is reduced [104].

To investigate the effect of an electron at the origin on its surroundings, a test charge is introduced, this changes the carrier distribution and the electrostatic potential. It is assumed that the test charge is small, so there is a negligible perturbation effect on the electron plasma, hence the quasi–thermal equilibrium of the plasma has always been maintained [96]. The screened electron distribution is the product of two electron field operators, given by

$$\begin{aligned} n_s(r) &= \hat{\psi}^\dagger(r)\hat{\psi}(r) \\ &= \frac{1}{V}\sum_{k,k'} e^{i(k-k').r} a_{k'}^\dagger a_k \\ &= \sum_q n_{sq} e^{iq.r}, \end{aligned} \tag{3.4.1}$$

where the Fourier transform of the density operator is

$$n_{sq} = \frac{1}{V} \sum a^{\dagger}_{k-q} a_k. \quad (3.4.2)$$

In the Hartree–Fock approach, an effective single particle Hamiltonian can be used to describe the screening effects

$$H_{eff} = \sum_k \epsilon_{ek} a^{\dagger}_{k-q} a_k + V \sum_q V_{sq} n_{s,-q}, \quad (3.4.3)$$

where the screened Coulomb potential is given by

$$V_{sq} = \frac{1}{V} \int \mathrm{d}^3 r V_s(r) e^{-iq.r}, \quad (3.4.4)$$

this is the similar to the bare potential, given by equation 3.2.27, where the $V(r)$ term is replaced with

$$V_s(r) = e\phi_s(r), \quad (3.4.5)$$

where $\phi_s(r)$ is the screened electrostatic potential. Using the Heisenberg equation [100, 105] and the effective Hamiltonian, equation 3.4.3, the time dependent equation of motion is given by

$$\begin{aligned} i\hbar \frac{\mathrm{d}}{\mathrm{d}t} a^{\dagger}_{k-q} a_k &= \left[a^{\dagger}_{k-q} a_k, H_{eff} \right] \\ &= (\epsilon_k - \epsilon_{k-q}) a^{\dagger}_{k-q} a_k + \sum V_{sq} (a^{\dagger}_{k-q} a_{k+p} - a^{\dagger}_{k-q-p} a_k), \end{aligned} \quad (3.4.6)$$

where the first and second terms correspond to the kinetic and Coulomb contributions respectively. By taking the expectation value and keeping the slowly varying terms, $p = -q$, gives

$$i\hbar \frac{\mathrm{d}}{\mathrm{d}t} \langle a^{\dagger}_{k-q} a_k \rangle = (\epsilon_k - \epsilon_{k-q}) \langle a^{\dagger}_{k-q} a_k \rangle + V_{sq} (n_{k-q} - n_k). \quad (3.4.7)$$

Under the *random phase approximation (RPA)* which is covered in the work of Haug and Koch [100], $\langle a^{\dagger}_{k-q} a_k \rangle$ is found to have a $e^{(\delta - i\omega)t}$ solution. Assuming that

the induced charge distribution follows the response of the plasma, which is homogeneous at $t = -\infty$ and the infinitesimal δ describes the adiabatic perturbation. Allows equation 3.4.7, to be written as

$$\langle a^{\dagger}_{k-q} a_k \rangle = V_{sq} \frac{n_{k-q} - n_k}{\hbar(\omega + i\delta) + \epsilon_{k-q} - \epsilon_k}, \tag{3.4.8}$$

and substituting into equation 3.4.2, gives the expectation value as

$$\langle n_{sq} \rangle = \frac{V_{sq}}{V} \sum_k \frac{n_{k-q} - n_k}{\hbar(\omega + i\delta) + \epsilon_{k-q} - \epsilon_k}. \tag{3.4.9}$$

The screening potential is determined by the Poisson equation in real space as

$$\nabla^2 \phi_s(r) = -\frac{4\pi e}{\epsilon_b} \left[n_e(r) + \langle n_s(r) \rangle \right], \tag{3.4.10}$$

taking the Fourier transform gives

$$\phi_{sq} = \frac{4\pi e}{\epsilon_b q^2} \left(\frac{1}{V} + \langle n_{sq} \rangle \right), \tag{3.4.11}$$

where

$$n_{eq} = \frac{1}{V} \int \delta^3(r) e^{-iq.r} \mathrm{d}^3 r = \frac{1}{V}, \tag{3.4.12}$$

for a point charge at the origin. Using equations 3.4.5, 3.4.9 and 3.4.11, the screened Coulomb potential can be written as

$$V_{sq} = V_q \left(1 - V_q \sum_k \frac{n_{k-q} - n_k}{\hbar(\omega + i\delta) + \epsilon_{k-q} - \epsilon_k} \right)^{-1}, \tag{3.4.13}$$

where the bare Coulomb potential, V_q, is given by equation 3.2.27. Repeating the derivation for the hole plasma, and adding the electron and hole contributions, the screened Coulomb potential energy between carriers can be written as

$$V_{sq} = \frac{V_q}{\epsilon_q(\omega)}, \tag{3.4.14}$$

where the longitudinal dielectric function, $\epsilon_q(\omega)$, is expressed as

$$\epsilon_q(\omega) = 1 - V_q \sum_k \sum_{\alpha=e,h} \frac{n_{\alpha,k-q} - n_{\alpha,k}}{\hbar(\omega + i\delta) + \epsilon_{\alpha,k-q} - \epsilon_{\alpha,k}}, \qquad (3.4.15)$$

which is known as the Lindhard formula [99, 103]. This describes the spatial and spectral dispersions of the dielectric function which is a complex and retarded function, with poles in the lower complex frequency plane [100]. The Lindhard formula can be modified to obtain a simpler treatment of the plasma screening, this is because in many practical situations, it is numerically too complicated to use because of its continuum of poles. Looking at the long wavelength limit, $\lambda \to \infty$, removes the spatial dependence, $q \propto 1/\lambda \to 0$, and by assuming a quasi–equilibrium system, the Fermi–Dirac distribution function can be used. Hence the Lindhard formula can be written as the Drude dielectric function [30, 103]

$$\epsilon_{q=0}(\omega) = 1 - \frac{\omega_{pl}^2}{\omega^2}, \qquad (3.4.16)$$

where the electron–hole plasma frequency ω_{pl} is given by

$$\omega_{pl}^2 = \frac{V_q q^2 N}{m_r}, \qquad (3.4.17)$$

or [30, 98]

$$\omega_{pl}^2 = \frac{2\pi N e^2}{\epsilon_b m_r}, \qquad (3.4.18)$$

by substitution of the bare Coulomb potential energy, given by equation 3.2.27.

The Drude dielectric function, given by equation 3.4.16, can be evaluated approximately by assuming that the excitation spectrum is dominated by plasmons [106] and this is known as the *Plasmon pole approximation*. Under the static plasmon pole approximation, the damped response of the screening can be ignored, hence the dielectric function can be simplified to

$$\frac{1}{\epsilon_q(\omega)} = 1 - \frac{\omega_{pl}^2}{\omega_q^2}. \qquad (3.4.19)$$

Which is similar to the Drude dielectric function, equation 3.4.16, where the ω term in the denominator has been replaced with the effective plasmon frequency ω_q. This approximation for the full dielectric function has replaced the continuum of poles contained in the Lindhard formula by one effective plasmon pole at ω_q [100]. Returning to the Lindhard formula, equation 3.4.15, and again using the static approximation, allows the effective plasmon frequency, ω_q, can be written as

$$\omega_q^2 = \omega_{pl}^2 \left[1 + \frac{q}{\kappa}\right] + C\left(\frac{\hbar q^2}{4m_r}\right)^2, \tag{3.4.20}$$

where the second term has been added to take into account the contribution from the pair continuum [107]. Where m_r is the reduced electron mass and the constant C has a value of between 1 and 4 [107]. With finite C, the effective plasmon frequency, ω_q, approaches the free–carrier dispersion, and the q^4 term is important to achieve correlation with screening due to the random phase approximation [107]. Hence the screened potential, V_{sq}, can be written as

$$V_{sq} = \frac{2^2\pi\epsilon_R a_0}{L^2 q}\left(\left(\frac{q}{\kappa}\right) + \frac{Ca_0q^3}{2^3\pi N}\right)\left(1 + \left(\frac{q}{\kappa}\right) + \frac{Ca_0q^3}{2^3\pi N}\right)^{-1}, \tag{3.4.21}$$

and in the case when $C = 0$, the screened potential simplifies to the Yukawa potential [100]

$$V_{sq} = \frac{2^2\pi\epsilon_R a_0}{L^2(q+\kappa)}. \tag{3.4.22}$$

The inverse static screening length, κ, which first appears in equation 3.4.20, is the effectiveness of the screening of the Coulomb interaction by other carriers [24], and it is used to calculate the screened potential, V_{sq}, in equation 3.4.21. At the level of the two band and quasi–equilibrium approximations the static screening length can be written as

$$\kappa = \frac{2}{a_0}\left(\frac{m_e}{m_r}f_{e0} + \frac{m_h}{m_r}f_{h0}\right), \tag{3.4.23}$$

where the exciton Bohr radius, a_0, is given by

$$a_0 = \frac{4\pi\epsilon_0\hbar\epsilon_b}{e^2 m_r}. \tag{3.4.24}$$

3.5 Bandgap renormalisation.

The screening of the Coulomb interaction at high carrier densities as discussed in section 3.4, causes a reduction in the localization of the single atom electron wavefunctions and increases the nearest neighbour electron overlaps. The larger overlap increases the width of the energy bands, hence reducing the bandgap between bands [8], this causes a red shift of the optical spectrum with increasing carrier density [37, 108–110]. This effect can be included by renormalisation of the bandgap, which is expressed as

$$\epsilon_g = \epsilon_{g0} + \Delta\epsilon_{CH} + \Delta\epsilon_{SX}, \tag{3.5.1}$$

where ϵ_{g0} is the unrenormalised bandgap and $\Delta\epsilon_{CH}$ and $\Delta\epsilon_{SX}$ are the Debye and screened–exchange shifts respectively, which are discussed in further detail in sections 3.5.1 and 3.5.2. The effects of bandgap renormalisation on the gain spectra are discussed in section 4.10 and the implications of bandgap renormalisation on individual transitions are covered in section 4.10.1.

3.5.1 Debye shift.

The Debye or Coulomb–hole shift, $\Delta\epsilon_{CH}$, occurs because of screening of the Coulomb interaction, this causes redistribution of the electron population resulting in a smaller effective bandgap [3, 111, 112]. The Debye or Coulomb–hole self energy can be explained by starting with the kinetic energies of electrons and holes for low exciton levels, which are given by equations 3.3.2 and 3.3.3 respectively. At high exciton levels the Coulomb potential, V_q, given by equation 3.2.27, is reduced to the screened Coulomb potential, V_{sq}, given by 3.4.21. This alters the value of the hole

energy, hence equation 3.3.3 for the unscreened hole energy, can be rewritten as

$$\epsilon^s_{hk} = \epsilon_{hk} + \sum_{q\neq 0}(V_{sq} - V_q), \tag{3.5.2}$$

for the screened case. The second term is the Debye shift, which using equation 3.4.14 can be written in terms of the screened Coulomb potential

$$\Delta\epsilon_{CH} = \sum_{q\neq 0} V_{sq}(\frac{1}{\epsilon_q} - 1), \tag{3.5.3}$$

by substitution of equation 3.4.21, this can be rewritten as

$$\Delta\epsilon_{CH} = -2\epsilon_R a_0 \int_0^\infty \left(1 + \frac{k}{\kappa} + \frac{Ca_0 k^3}{32\pi N_{2d}}\right)^{-1} \mathrm{d}k, \tag{3.5.4}$$

where using an approximation for the integral gives

$$\Delta\epsilon_{CH} \simeq -2\epsilon_R a_0 \kappa \ln\left(1 + \sqrt{\frac{32\pi N_{2d}}{Ca_0\kappa^3}}\right). \tag{3.5.5}$$

3.5.2 Exchange shift.

The exchange shift, $\Delta\epsilon_{SX}$, comes from the Hartree–Fock contribution to the semiconductor Bloch equations in equation 3.3.7. The Hartree–Fock contributions contains two many body effects, renormalisation of the electric–dipole interaction energy and a density dependent contribution to the transition energy. Many–body Coulomb interactions cause this normalization and they couple equations for different k states. Using the screened Hartree–Fock approximation the screened–exchange shift can be written as

$$\Delta\epsilon_{SX,k} = -\sum_{k'\neq k} V_{s,|k-k'|}(n_{ek'} + n_{hk'}) \tag{3.5.6}$$

and by substitution of equation 3.4.21 gives

$$\Delta\epsilon_{SX} = -\frac{2\epsilon_R a_0}{\kappa}\int_0^\infty k\left(1+\frac{C\kappa a_0 k^2}{32\pi N_{2d}}\right)\left(1+\frac{k}{\kappa}+\frac{C a_0 k^3}{32\pi N_{2d}}\right)^{-1}(n_{ek}+n_{hk})\,\mathrm{d}k, \tag{3.5.7}$$

where the weak k dependence of the exchange shift has been neglected.

3.6 Program details.

The theory introduced in the earlier sections of this chapter 3.2–3.5, has been developed into a computational model by Weng Chow [113] to permit the investigation of InGaN structures. The gain is calculated using equation 3.3.22 which is based on the Pade approximation and has inputs from the band structure properties which were calculated using a 6×6 Luttinger–Kohn Hamiltonian and the envelope approximation. The Coulomb enhancement which appears in the equation for gain (equation 3.3.22), is given by equation 3.3.17 where the screened Coulomb potential is given by equation 3.4.21. The effects of bandgap renormalisation were calculated using the Debye and exchange shifts which are given by equations 3.5.5 and 3.5.7 respectively. The results presented in this thesis were obtained by modifying and developing this computational model to permit the interpretation of experimental results performed by Pope [63] and Olaizola Izquierdo [64].

3.7 Summary.

In this chapter the gain at the level of the Pade approximation for a many–body system has been derived. It was found that the many body Coulomb effects cause bandgap renormalisation with contributions from the Debye and Exchange shifts, and increase the gain through the Coulomb enhancement term. If these effects are neglected the model returns to the level of free carrier theory and in chapter 4, the relative importance of these effects is investigated.

Chapter 4

Programming issues.

4.1 Introduction.

In this chapter, the material parameters and the model originally written by Weng Chow [113] at the level of the Pade approximation discussed in chapter 3 are investigated. We begin with the alterations and developments made to the original model in section 4.2. We then go on to discuss the material parameters of InGaN structures and in sections 4.3 and 4.4 the bandgap and band offset ratio are investigated. Section 4.5 goes on to discuss the issue of the internal field, with examination of the direction and strength of the strain, piezoelectric and spontaneous fields. In section 4.6, the screening of the internal field is investigated and an approximation for the screening field is introduced. Section 4.7 covers the homogeneous lineshape function and the effects of hyperbolic secant (sech) and Lorentzian lineshapes, and the value of the homogeneous lineshape factor on the gain spectra investigated. In section 4.8 methods of calculating the spontaneous emission are discussed. In section 4.9 the contributions to the overall gain from different transitions are investigated. In section 4.10, effects on the gain spectra of the different contributions to the Pade model are investigated. Starting with the free carrier model the effects of bandgap renormalisation, internal field screening and Coulomb enhancement (sections 4.10.1–4.10.3) are included separately to assess the relative importance of each

effect and in section 4.10.4 all the effects are bought together to return to the Pade model. Finally in section 4.11 the chapter is reviewed.

In this chapter a 4 nm $In_{0.07}Ga_{0.93}N/GaN$ quantum well structure, at threshold has been investigated. Using a typical value of 60 cm^{-1} for the threshold modal gain and dividing by the optical confinement factor which was calculated to be $\Gamma = 0.018$ using the transfer matrix method, the material gain of this structure was calculated as 3330 cm^{-1}. Using equation 3.3.22 the threshold material gain at room temperature was found to occur at a carrier density of $N = 5.85\times10^{16}$ m^{-2} and this value was used for all results presented in this chapter unless stated otherwise.

4.2 Computing issues.

The results presented in this thesis were obtained using a code originally written by Weng Chow [113], which has been developed and modified. The model which was originally written in Fortran 77^{TM} was modified and updated to permit the full use of the functionality of Fortran 90^{TM}. In addition the code was tested on a suite of compilers to ensure accurate and reproducible results

The model was analysed to permit the understanding of the underlying physics and from this the factors affecting the level of complexity were identified and this is discussed in section 4.10 and chapter 6. The inclusion of the Coulomb interaction which was detailed in section 3.2.3, increases the run time from minutes to hours, hence most of the initial investigative work was performed without this effect. An additional front end program was written to control the model and allow the rapid and efficient stepping over of such variables such as reverse bias and carrier density. Also routines for the spontaneous emission and depletion width were incorporated into the model and a graphics package was also hard wired into the code to allow real time visualisation of the results.

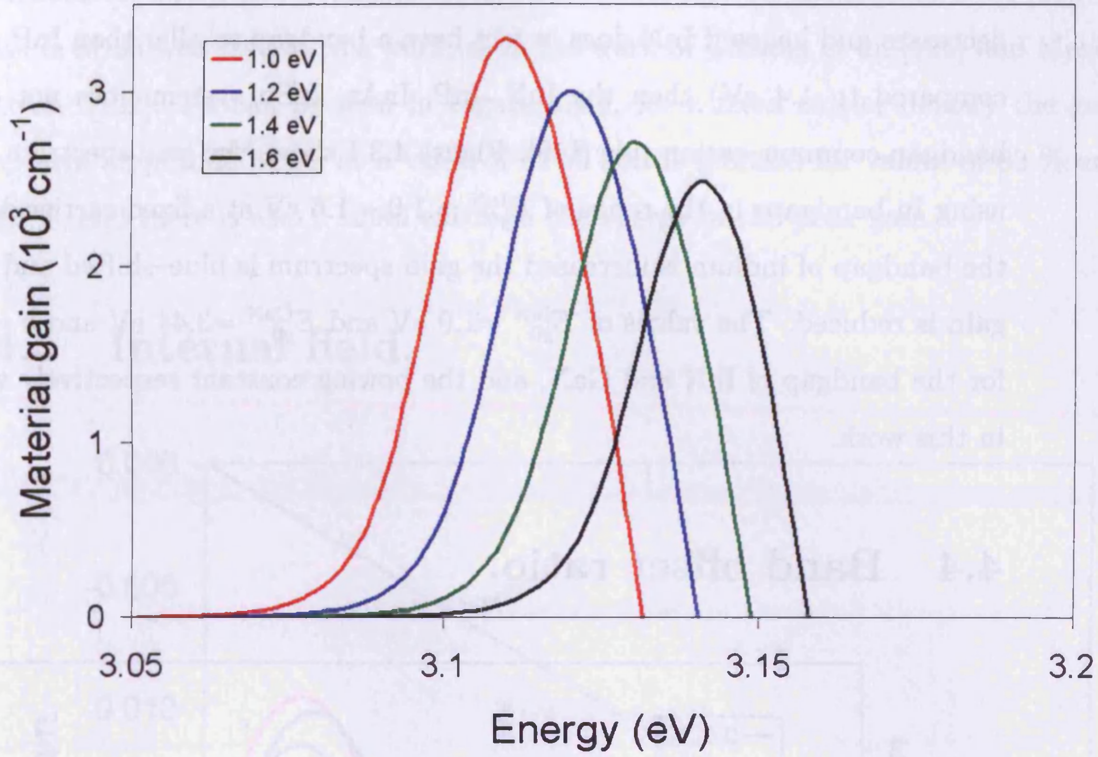

Figure 4.3.1: Gain spectra for values of the bandgap of InN in the range of 1.0–1.6 eV calculated at the level of the Pade model.

4.3 Bandgap.

In an III–V based device, the group V element predominantly controls the bandgap, with the group III element providing fine tuning over a restricted range [18], so in a InGaN based device the nitrogen dominates the bandgap. For $In_xGa_{1-x}N$, the bandgap can be found by interpolation between the values of InN and GaN [1, 67, 114–116]

$$E_{g0} = E_{g0}^{\mathrm{InN}} x + E_{g0}^{\mathrm{GaN}}(1-x) - bx(1-x), \tag{4.3.1}$$

where the last term contains the bowing parameter, b, which is a correction to the linear approximation [117]. Recent work performed on wurtzite InN measured values of 1.0 eV [118] and 0.85 eV [119]) for the bandgap of InN, much smaller than the 1.89 eV or larger bandgap widely accepted in the past [24, 51, 120]. The

common–cation rule states that the bandgap increases as the anion atomic number decreases and hence if InN does in fact have a bandgap smaller than InP (<1.0 eV compared to 1.4 eV) then the InN, InP, InAs, InSb system does not obey the bandgap common–cation rule [119]. Figure 4.3.1 shows the gain spectrum obtained using In bandgaps in the range of $E_{g0}^{\mathrm{InN}} = 1.0 - 1.6$ eV at a fixed carrier density, as the bandgap of indium is increased the gain spectrum is blue–shifted and the peak gain is reduced. The values of E_{g0}^{InN} =1.0 eV and E_{g0}^{GaN} =3.44 eV and $b = 1.02$ eV for the bandgap of InN and GaN, and the bowing constant respectively were used in this work.

4.4 Band offset ratio.

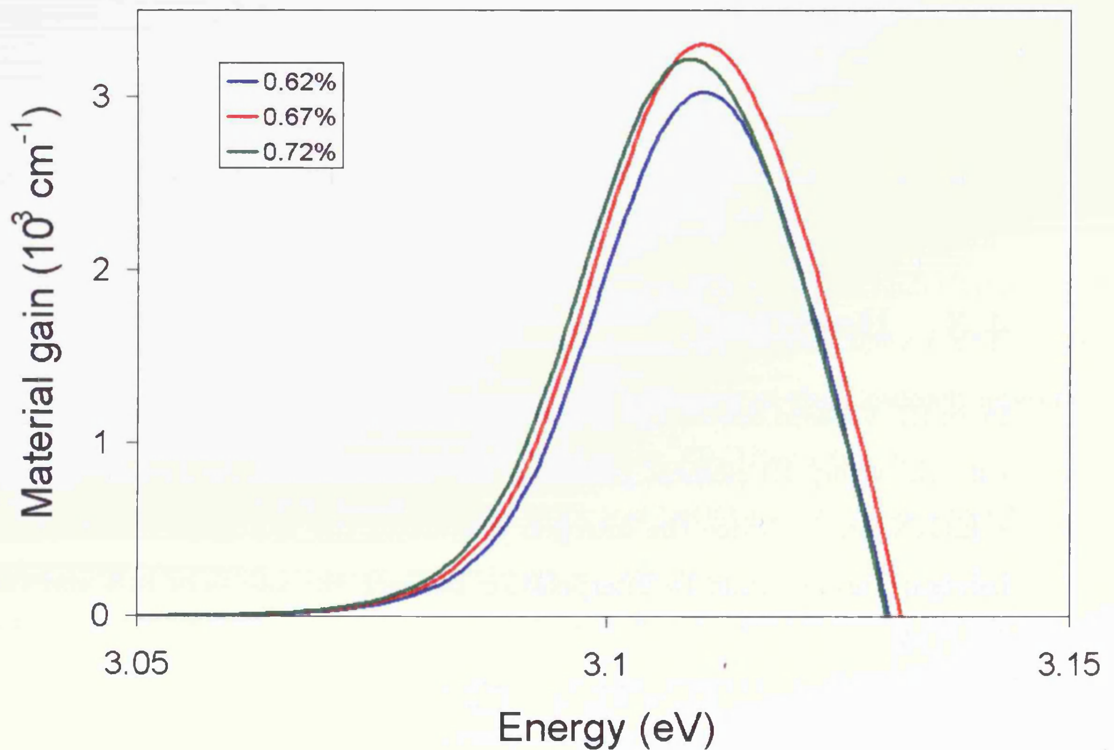

Figure 4.4.1: Gain spectra for conduction band offsets in the range of 62–72 %.

The band offset ratio (conduction:valence) is not accurately known for these

structures, but it has been shown to have little effect on the gain spectra [66]. A value 67:33 was used in this work, as in the work of Chuang et al. [121] and Meney et al. [122]. As can be seen in Figure 4.4.1, for a fixed carrier density the gain spectra amplitude peaks at a value of 67 % and is reduced for values of 62 % and 72 %, and there is also a small effect on the energy of the peak gain.

4.5 Internal field.

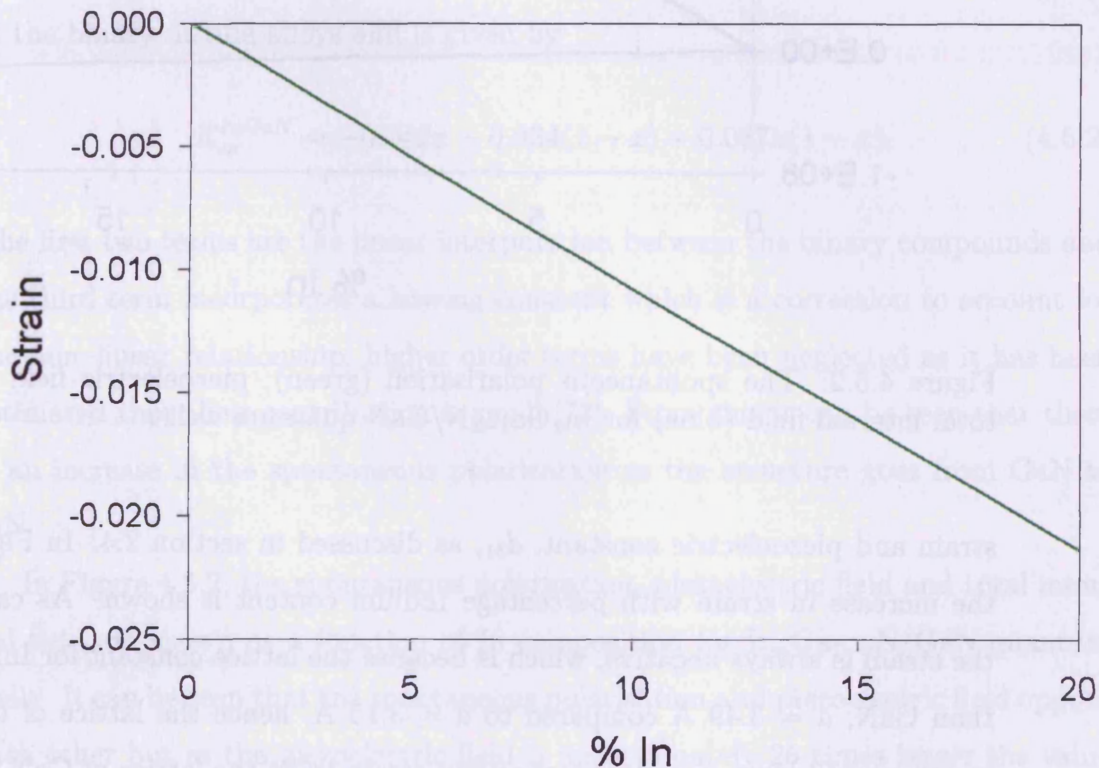

Figure 4.5.1: The strain due to lattice mismatch in $In_xGa_{1-x}N/GaN$ quantum wells.

The origin of the internal field was covered in chapter 2 and is the sum of the piezoelectric and spontaneous polarisation fields. In this section the values of strain, piezoelectric and spontaneous polarisation fields for $In_xGa_{1-x}N$ based quantum well structures are presented.

Theoretical values of the piezoelectric field are proportional to the product of the

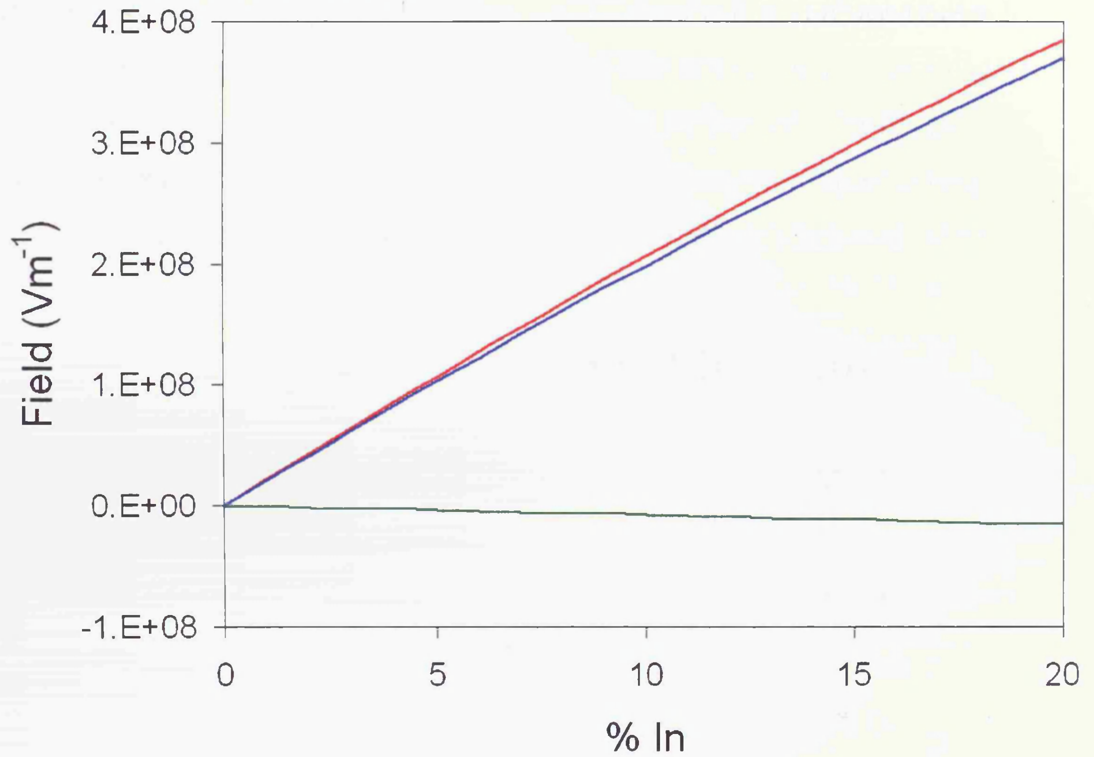

Figure 4.5.2: The spontaneous polarisation (green), piezoelectric field (red) and total internal field (blue) for $In_xGa_{1-x}N/GaN$ quantum wells.

strain and piezoelectric constant, d_{31}, as discussed in section 2.4. In Figure 4.5.1, the increase in strain with percentage Indium content is shown. As can be seen the strain is always negative, which is because the lattice constant for InN is larger than GaN, $a = 3.49$ Å compared to $a = 3.15$ Å, hence the lattice of the InGaN quantum well layer is under compressive strain to fit the lattice of GaN.

The value of the piezoelectric constant for AlN is $d_{31} = -2.0 \times 10^{-12}$ mV^{-1} [51] and using the ratio of the static dielectric constants, ϵ, of InN, GaN and AlN which are 15.3, 10 and 8.5 respectively [123], the values for GaN and InN of $d_{31} = -1.7 \times 10^{-12}$ mV^{-1} and $d_{31} = -1.1 \times 10^{-12}$ mV^{-1} respectively were obtained by Martin et al. [124]. These values have also been used in the work of Chow et al. [24] and Berkowicz et al. [93].

In a theoretical study, Al–Yacoub [125] found that the piezoelectric coefficients,

d_{31}, of InGaN vary linearly with indium concentration. Hence the piezoelectric coefficient, d_{31}, for $In_xGa_{1-x}N$ was obtained using linear interpolation of the binary values

$$d_{31}^{InGaN} = d_{31}^{InN} x + d_{31}^{GaN}(1-x). \tag{4.5.1}$$

The piezoelectric coefficient, d_{31}, of InGaN based structures, is 10 times larger than other III–V materials and up to 100 times larger than non–ferroelectric piezoelectrics e.g. quartz [48, 49].

The spontaneous polarization of $In_xGa_{1-x}N$ is also calculated using interpolation of the binary nitride alloys and is given by

$$E_{sp}^{InGaN} = -0.042x - 0.034(1-x) + 0.037x(1-x). \tag{4.5.2}$$

The first two terms are the linear interpolation between the binary compounds and the third term incorporates a bowing constant which is a correction to account for the non–linear relationship, higher order terms have been neglected as it has been estimated that their contribution is small [73]. From this it can be seen that there is an increase in the spontaneous polarization as the structure goes from GaN to InN.

In Figure 4.5.2, the spontaneous polarisation, piezoelectric field and total internal field are shown as a function of In composition for $In_xGa_{1-x}N$/GaN quantum wells. It can be seen that the spontaneous polarisation and piezoelectric field oppose each other but as the piezoelectric field is approximately 25 times larger the value of the total internal field is close to that of the piezoelectric field. As discussed in chapter 2, if the structure was under tensile strain e.g. AlGaN/GaN, the direction of the piezoelectric field is reversed and points in the same direction as the spontaneous field. In chapter 5, the measurement of the internal field is discussed and comparisons made with experimental results obtained using the method of reverse bias photocurrent spectroscopy.

4.6 Screening of the internal field.

The internal field has a large effect on the concentration, distribution and recombination of carriers in InGaN based devices [73], hence an accurate description is important. In chapter 2, the internal field was discussed and an approximation for the screening of the internal field was developed in section 2.6. In this section the approximation is investigated and comments made on it's validity. In Figure 4.6.1 (top), the average and $z-$dependent screening field obtained from equations 2.6.5 and 2.5.4 respectively, are shown for a 4 nm $In_{0.07}Ga_{0.93}N/GaN$ quantum well at carrier densities of 1×10^{16} and 5.85×10^{16} m^{-2}. These values of carrier density correspond to the Mott (see section 4.10.3) and threshold carrier densities respectively. At low carrier density the variation of the screening field across the well is small, but at high carrier density there is a large variation. Hence the constant field approximation given by equation 2.6.5 accurately describes the low density case, but the approximation is poor at higher carrier densities.

Even though the use of the average screening field across the well as shown in Figure 4.6.1 (top), is a poor approximation at high carrier densities, it still may be valid if the effects of the screening on the field are small. In Figure 4.6.1 (bottom), the overall screened internal field using both the average and $z-$dependent screening processes, which was calculated using equation 2.5.1 is shown. It can be seen that the effect of the screening is large, reducing the internal field to almost half of its unscreened value, hence there are large differences in the screened internal field across the well obtained using the average and $z-$dependent methods.

By integrating over the screened internal field the change in potential across the well due to the average and $z-$dependent internal field is obtained and this is shown in Figure 4.6.2. It can be seen that there is correlation between the average and $z-$dependent values at both low and high values of carrier density, hence the average screening field is a valid approximation for the structures investigated in this work.

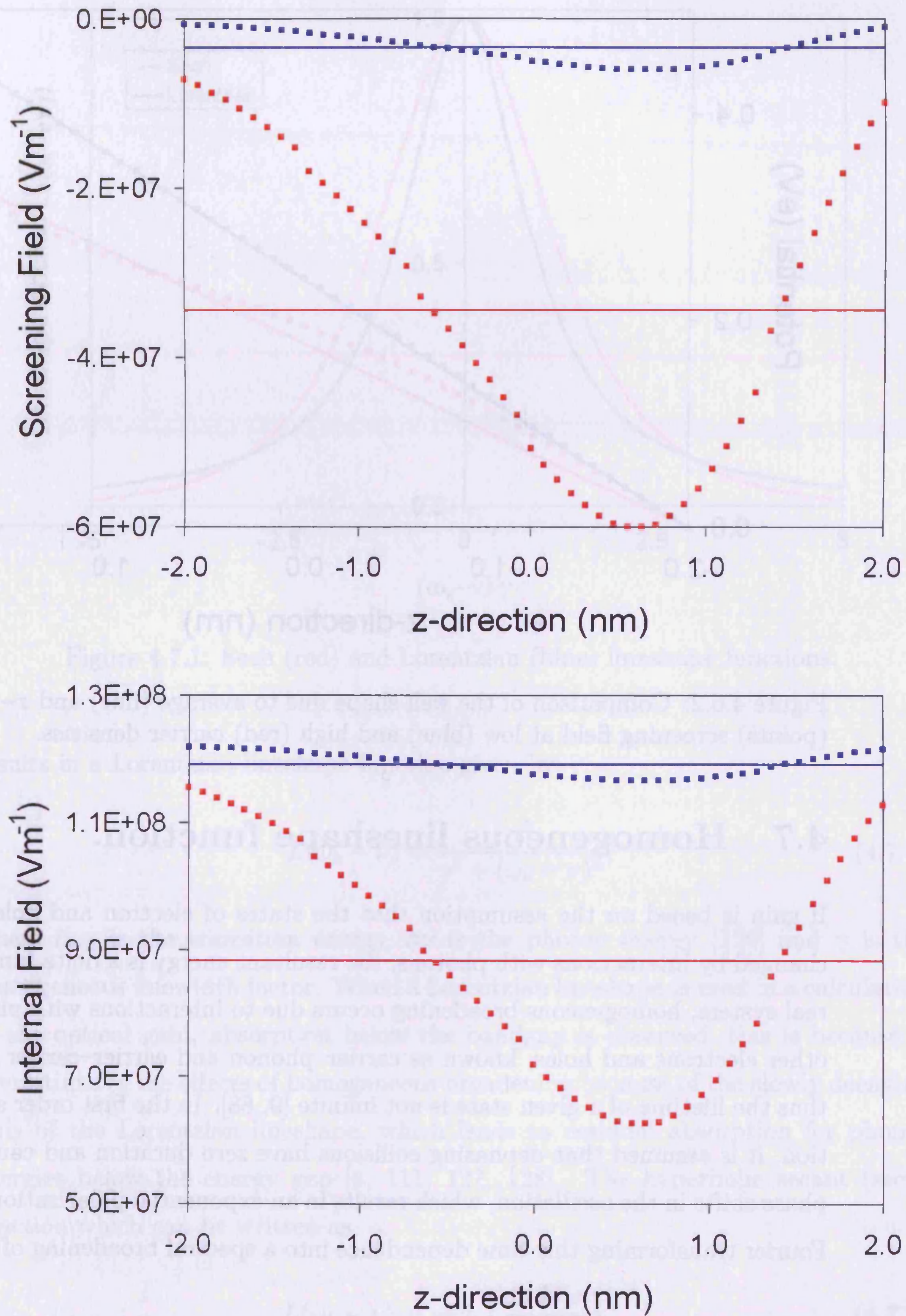

Figure 4.6.1: Comparison of the average (line) and $z-$dependent (points) for the screening field (top) and the screened internal field (bottom) at low (blue) and high (red) carrier densities.

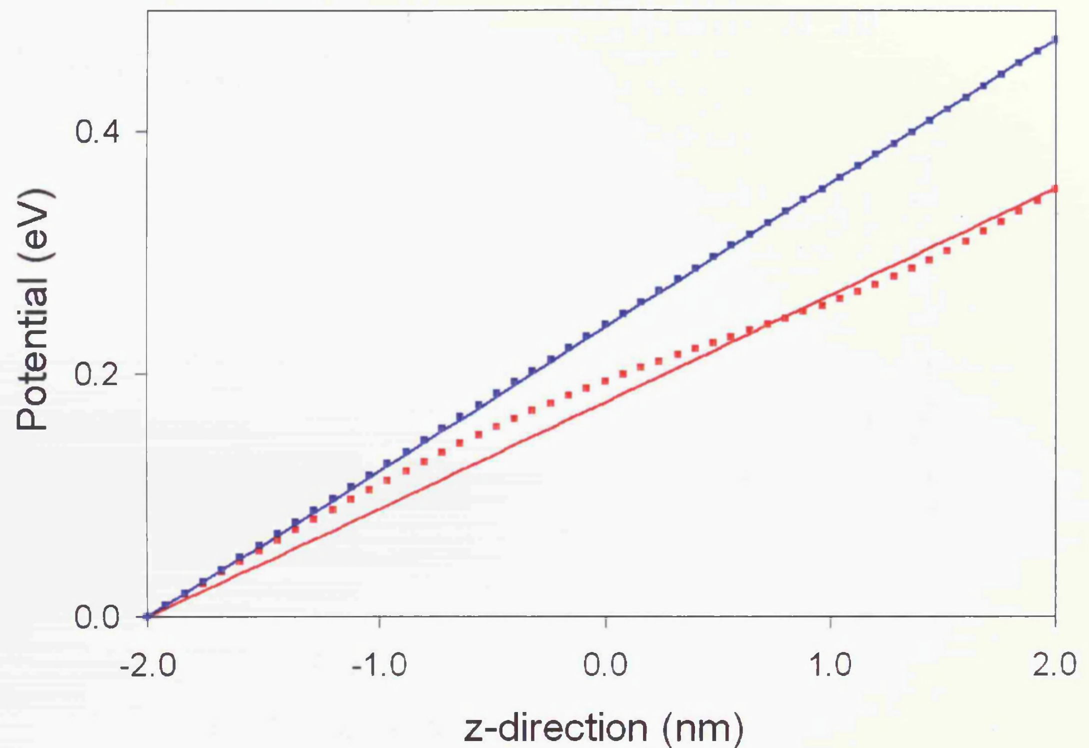

Figure 4.6.2: Comparison of the well shape due to average (line) and $z-$dependent (points) screening field at low (blue) and high (red) carrier densities.

4.7 Homogeneous lineshape function.

If gain is based on the assumption that the states of electron and holes are only changed by interactions with photons, the resultant energy is a delta function. In a real system, homogeneous broadening occurs due to interactions with phonons and other electrons and holes, known as carrier–phonon and carrier–carrier scattering, thus the lifetime of a given state is not infinite [9, 88]. In the first order approximation, it is assumed that dephasing collisions have zero duration and cause random phase shifts in the oscillation, which results in an exponential polarization decay [8]. Fourier transforming this time dependence into a spectral broadening of the energy

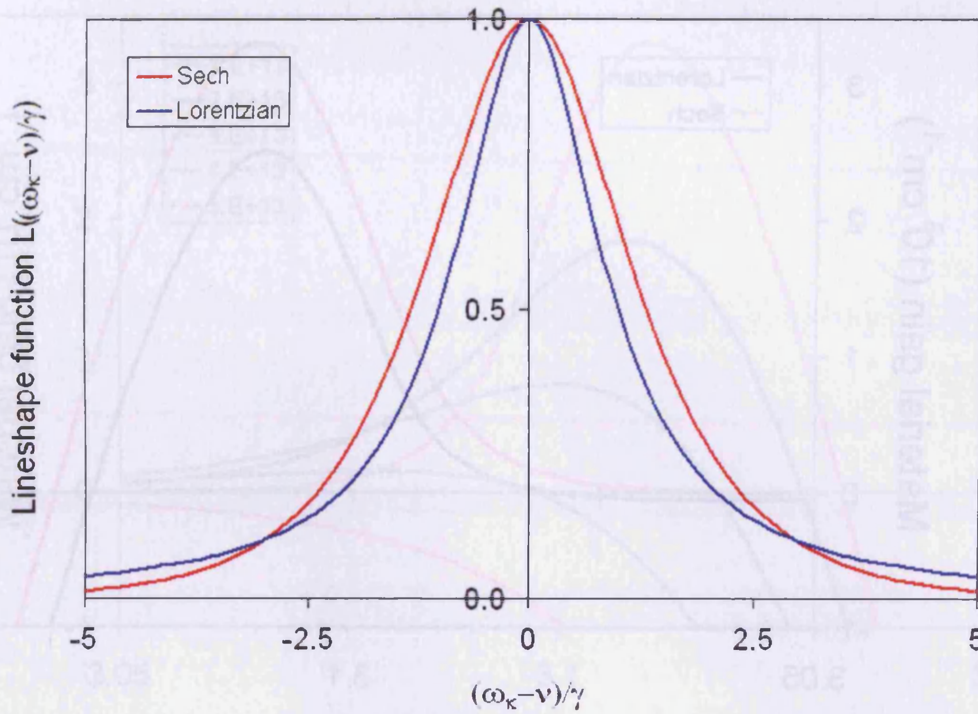

Figure 4.7.1: Sech (red) and Lorentzian (blue) lineshape functions.

results in a Lorentzian lineshape function given by

$$L(\omega_k - \nu) = \frac{\gamma^2}{\gamma^2 + (\omega_k - \nu)^2}, \tag{4.7.1}$$

where $\hbar\omega_k$ is the transition energy, $\hbar\nu$ is the photon energy [126] and γ is the homogeneous linewidth factor. When a Lorentzian lineshape is used in a calculation of the optical gain, absorption below the bandgap is observed, this is because it overestimates the effects of homogeneous broadening because of the slowly decaying tails of the Lorentzian lineshape, which leads to residual absorption for photon energies below the energy gap [8, 111, 127, 128]. The hyperbolic secant (sech) function which can be written as

$$L(\omega_k - \nu) = \text{sech}\left(\frac{\omega_k - \nu}{\gamma}\right), \tag{4.7.2}$$

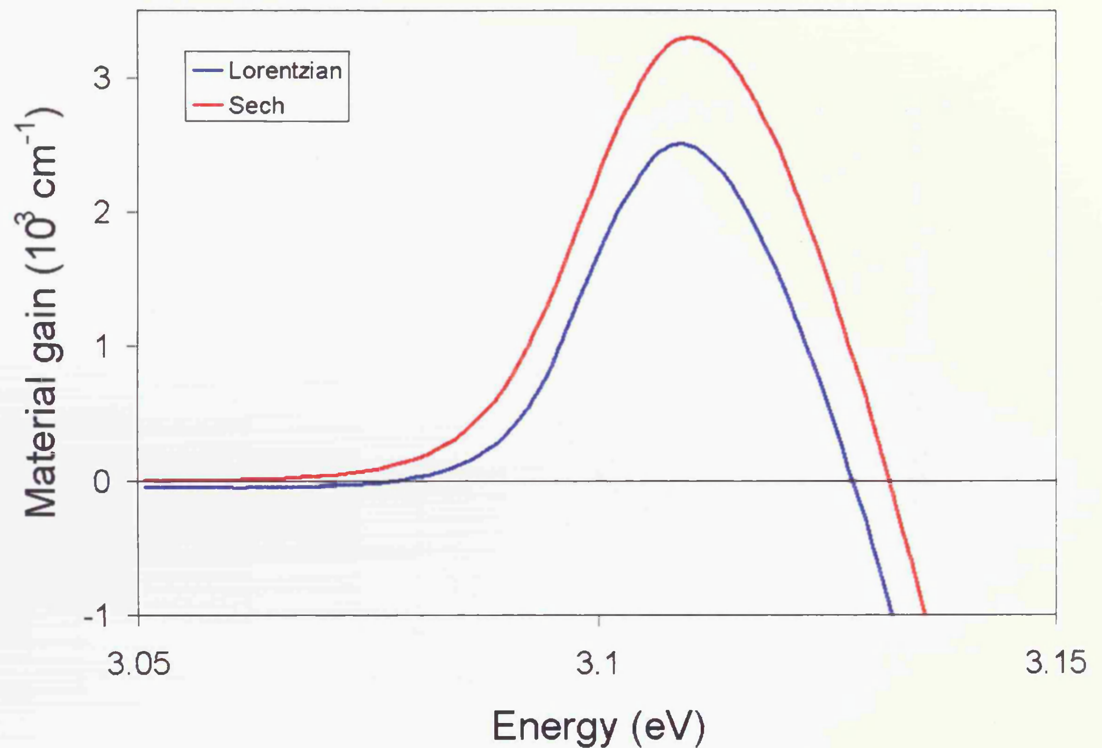

Figure 4.7.2: Gain spectra obtained using the sech and Lorentzian homogeneous lineshape functions.

decays away quicker and hence removes the absorption below the bandgap. The sech and Lorentzian functions are shown in Figure 4.7.1 and the slowly decaying tails of the Lorentzian function in comparison with the sech function can be clearly seen. In Figure 4.7.2, the gain spectra obtained using the sech and Lorentzian lineshape functions is shown and the absorption below the bandgap due to the slowly decaying tails of the Lorentzian lineshape can be seen.

Also, the sech lineshape function results in a larger peak gain than the Lorentzian lineshape for the same value of homogeneous linewidth factor, as shown in Figure 4.7.2. This is due to the effect of the long tails of the Lorentzian lineshape causing a reduction in the peak gain due to absorption at high energies. Increasing the homogeneous lineshape factor, as shown in Figure 4.7.3 for a sech function, causes a reduction in the gain peak. At large values of homogeneous lineshape

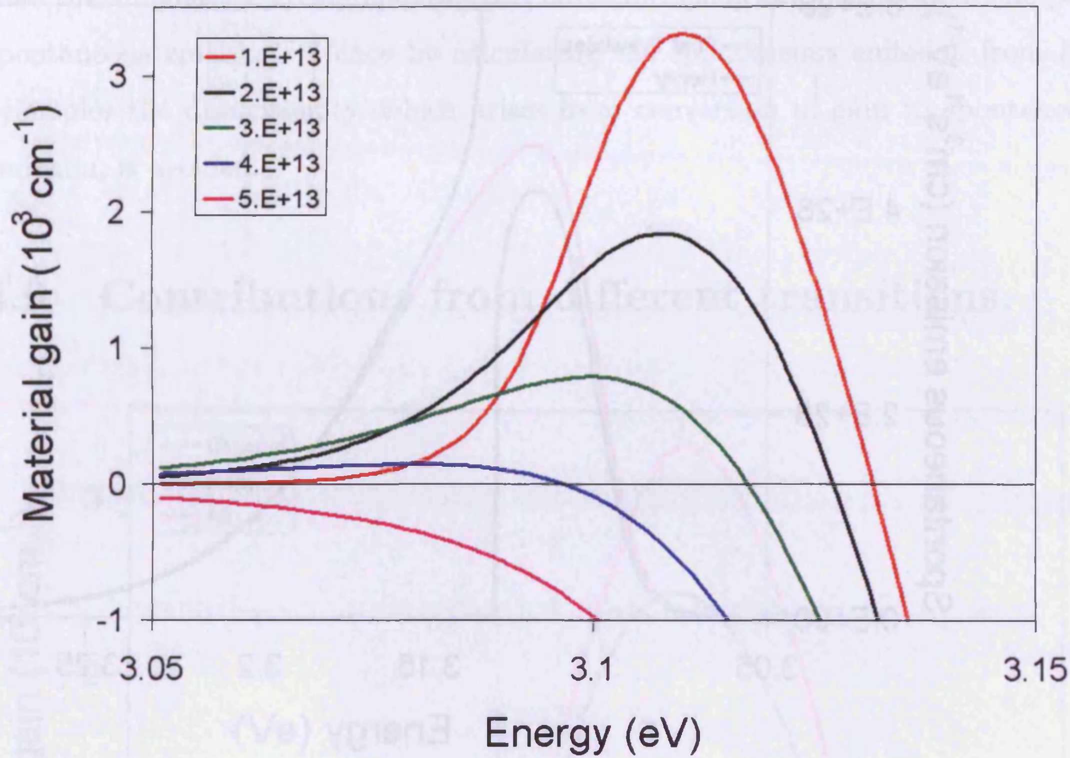

Figure 4.7.3: Gain spectra obtained using the sech lineshape function with values of the homogeneous lineshape factor in the range of γ =1.e13–5.e13 s^{-1}.

factor ($\gamma = 5 \times 10^{13}\text{s}^{-1}$) the broadening from the high energy region means that positive gain does not occur. The sech lineshape and a homogeneous linewidth value of $\gamma = 1 \times 10^{13}\text{s}^{-1}$ is commonly used [8, 88, 115, 126], which was obtained from curve fits of gain and spontaneous emission spectra to measurements, and corresponds to a 7 meV spread of the expected energy.

4.8 Spontaneous emission.

The spontaneous emission spectrum, $S(\omega)$, can be obtained from the gain spectra, $g(\omega)$, using the Henry formula [115]

$$S(\omega) = \frac{1}{\hbar}\left(\frac{n\omega}{\pi c}\right)^2 g(\omega)\left[1 - e^{\frac{\hbar\omega - \Delta F}{k_B T}}\right]^{-1}. \tag{4.8.1}$$

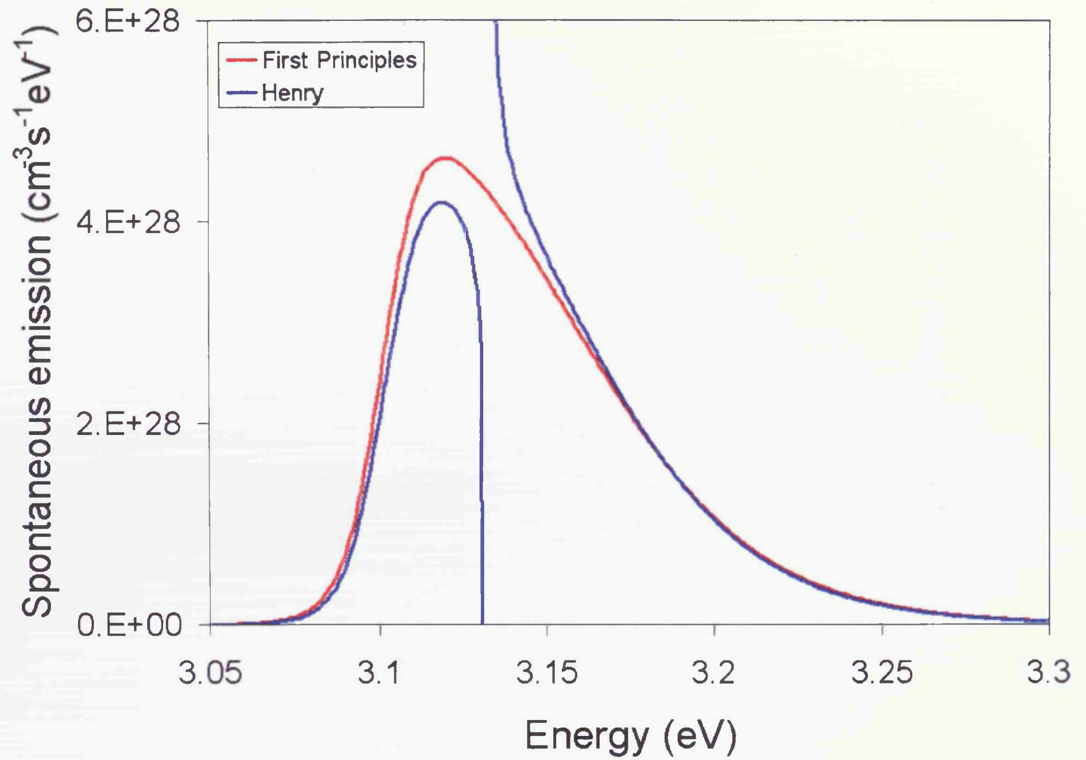

Figure 4.8.1: Spontaneous emission spectrum obtained using the Henry formula and from first principles.

Due to the homogeneous broadening of the gain spectra [20, 129], which was discussed in detail in section 4.7, the transparency point is no longer equal to the Fermi level separation, $E(g \rightarrow 0) \neq \Delta E_F$. Hence using equation 4.8.1 to obtain the spontaneous emission from the gain causes a singularity in the spontaneous emission spectrum, as shown in Figure 4.8.1. This singularity can be removed by using an equation originally developed from first principles by Jahnke and Koch [130] but here it is written as

$$S(\omega) = \frac{n\nu^3}{3\epsilon_0\omega\pi^3\hbar^2 c}\int_0^\infty k|\mu_k|^2 \frac{f_{ek}f_{hk}}{i(\omega_k - \nu) + \gamma}\frac{1}{1 - q(k)}\mathrm{d}k, \qquad (4.8.2)$$

which is in the same form as in the work of Wieczorek et al. [131] and is similar to the equation for gain in chapter 3. In addition, it can be seen in Figure 4.8.1

that the singularity in the spontaneous emission spectrum also reduces the peak spontaneous emission. Hence by calculating the spontaneous emission from first principles the discontinuity, which arises from conversion of gain to spontaneous emission, is avoided.

4.9 Contributions from different transitions.

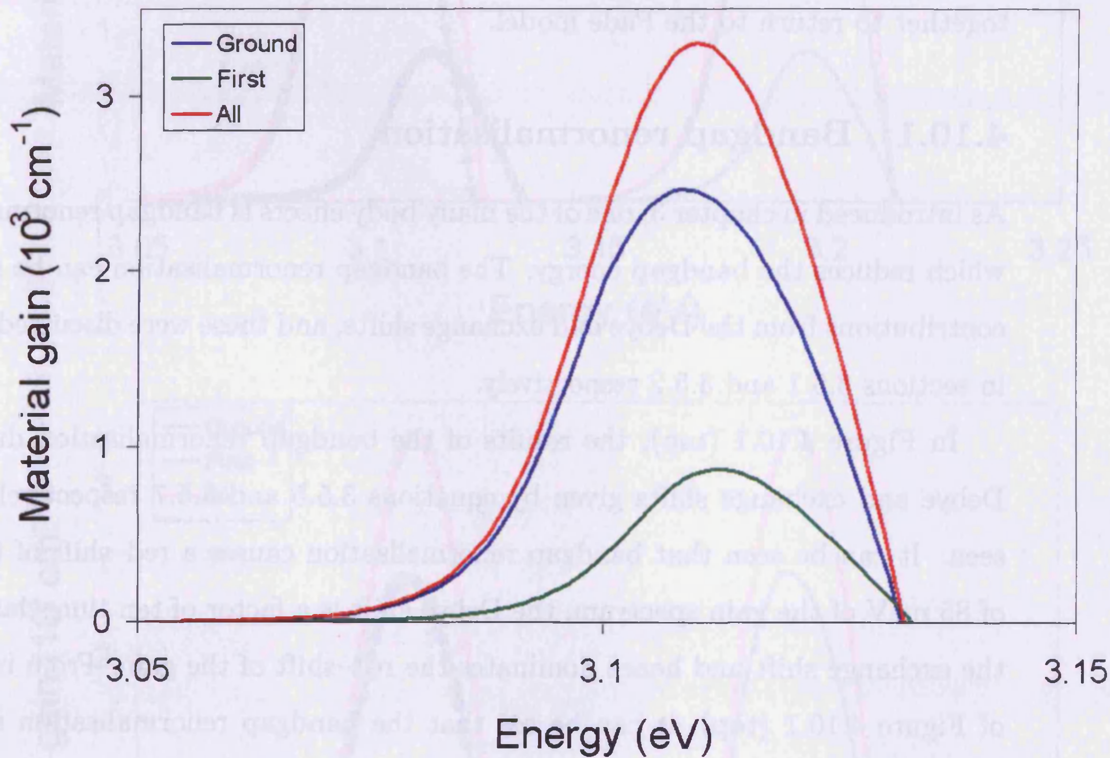

Figure 4.9.1: Contributions to the gain spectra from the ground and first transitions.

In Figure 4.9.1 the contributions to the gain from the different transitions can be seen. 75 % of the gain comes from the ground state transition with the remaining 25 % coming from the first order transition. Contributions from higher order transitions are negligible because of the small dipole matrix element. The effects of bandgap renormalisation on the different transitions is discussed in section 4.10.1.

4.10 Contributions to the Pade model.

In this section the effects of the contributions to the Pade model discussed in chapter 3 are investigated for an $In_{0.07}Ga_{0.93}N/GaN$ quantum well at a carrier density of $N = 5.85\times10^{16}$ m^{-2}. This is achieved by breaking the model down to the basic free carrier model, and then including separately bandgap renormalisation, screening of the internal field and Coulomb enhancement (sections 4.10.1–4.10.3) to assess the relative importance of each effect. Finally in section 4.10.4 all the effects are bought together to return to the Pade model.

4.10.1 Bandgap renormalisation.

As introduced in chapter 3, one of the many body effects is bandgap renormalisation, which reduces the bandgap energy. The bandgap renormalisation can be split into contributions from the Debye and exchange shifts, and these were discussed in detail in sections 3.5.1 and 3.5.2 respectively.

In Figure 4.10.1 (top), the results of the bandgap renormalisation due to the Debye and exchange shifts given by equations 3.5.5 and 3.5.7 respectively can be seen. It can be seen that bandgap renormalisation causes a red–shift of the order of 85 meV of the gain spectrum, the Debye shift is a factor of ten times larger than the exchange shift and hence dominates the red–shift of the gain. From inspection of Figure 4.10.1 (top), it can be see that the bandgap renormalisation results in the ground and first order transition having gain over differing energy ranges. This causes a smaller gain peak and broadens the gain spectrum, in comparison with the unrenormalised case. The minimum and maximum limits of positive gain are determined by the bandgap, E_g, and the Fermi level separation, ΔE_F, respectively [8]. Hence from this it can be established that the bandgap renormalisation results in each transition having a different Fermi level, and in the extreme case can cause the overall gain spectrum to have a multiple peak profile.

To overcome this issue the transition energy was renormalised, this is shown in Figure 4.10.1 (bottom) and it can be clearly seen that the transitions have the

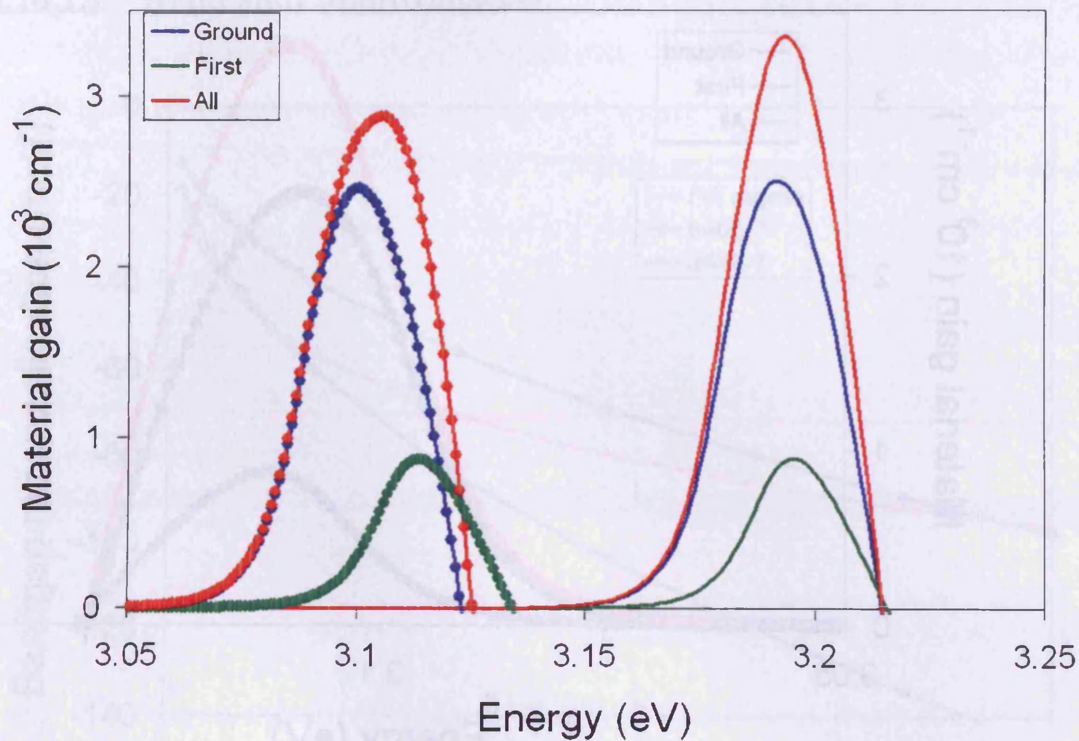

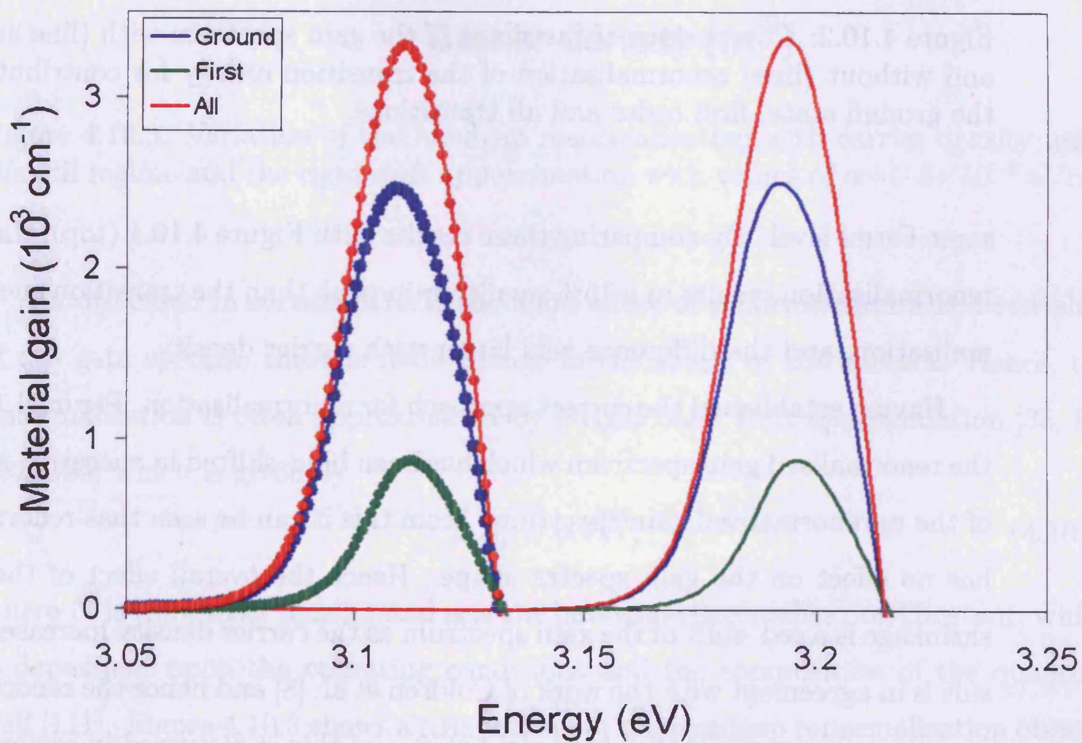

Figure 4.10.1: Gain spectrum with (line and points) and without (line) renormalisation of the bandgap (top) and transition (bottom) energy for contributions from the ground state, first order and all transitions.

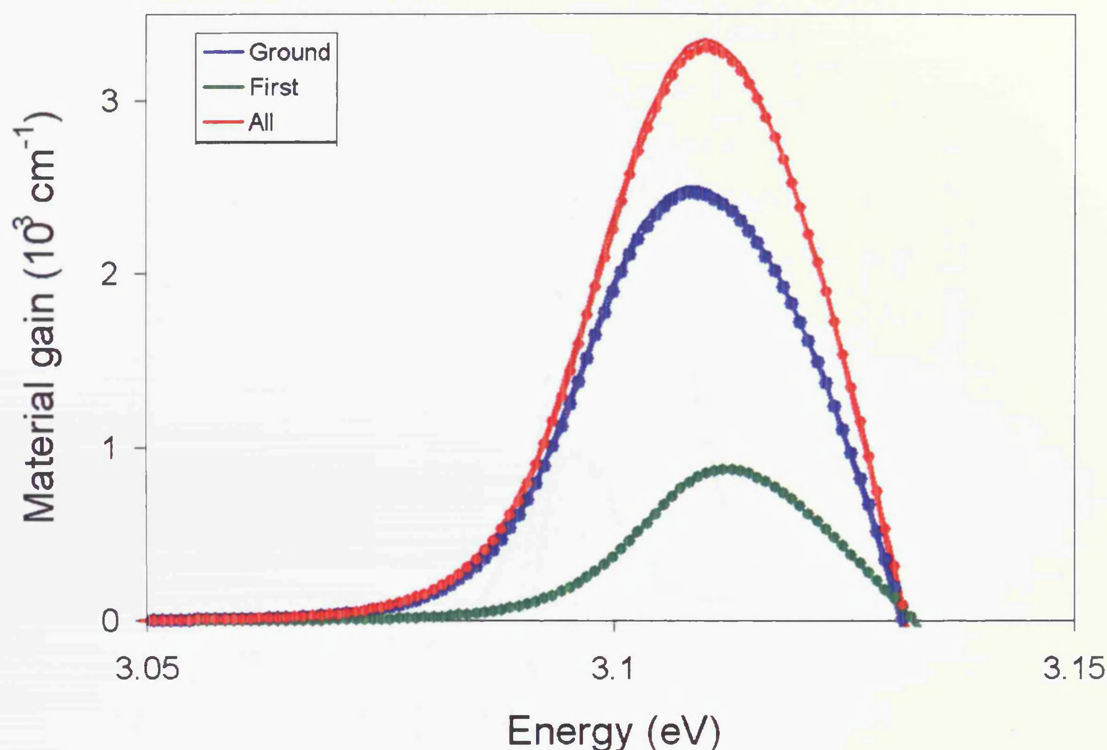

Figure 4.10.2: Comparison of the shape of the gain spectrum with (line and points) and without (line) renormalisation of the transition energy for contributions from the ground state, first order and all transitions.

same Fermi level. By comparing these results with Figure 4.10.1 (top), the bandgap renormalisation results in a 15% smaller gain peak than the transition energy renormalisation, and the difference gets larger with carrier density.

Having established the correct approach for renormalisation, Figure 4.10.2 shows the renormalised gain spectrum which has been blue–shifted in energy to match that of the unrenormalised gain spectrum. From this it can be seen that renormalisation has no effect on the gain spectra shape. Hence the overall effect of the bandgap shrinkage is a red–shift of the gain spectrum as the carrier density increases. This result is in agreement with the work of Coldren et al. [8] and hence the renormalisation is commonly approximated by a rigid shift and this is discussed in section 4.10.1.1.

4.10.1.1 Rigid shift approximation.

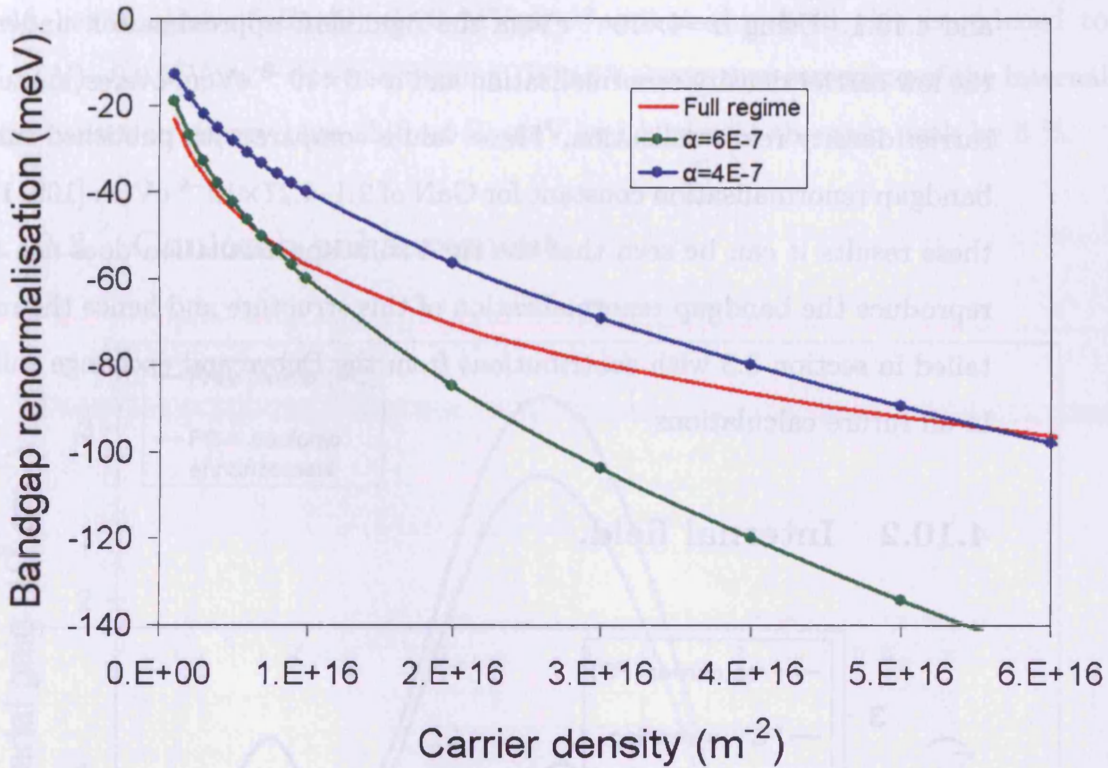

Figure 4.10.3: Variation of the bandgap renormalisation with carrier density using the full regime and the rigid shift approximation with values of α=4–6$\times10^{-8}$ eVcm.

As discussed in section 4.10.1, the main effect of renormalisation is a red–shift of the gain spectra, there is little change in the shape of the spectra. Hence, the renormalisation is often approximated by a rigid band shift approximation [35, 88, 132, 133] which is given by

$$\Delta E_g = \alpha\sqrt{N}, \quad (4.10.1)$$

where N is the carrier density and α is the bandgap renormalisation constant, which is dependent upon the operating conditions and the composition of the quantum well [111]. Figure 4.10.3 shows a comparison of the bandgap renormalisation obtaining using the full regime detailed in section 4.10.1 with the rigid shift approximation. The bandgap renormalisation constant, α, was used as an adjustable parameter and

values of α=4–6$\times10^{-8}$ eVcm are shown. It can be seen that for these results the rigid shift approximation does not accurately reproduce the model detailed in sections 3.5 and 4.10.1. Using α=4$\times10^{-8}$ eVcm the rigid shift approximation underestimates the low carrier density renormalisation and α=6$\times10^{-8}$ eVcm overestimates the high carrier density renormalisation. These values compare with published values of the bandgap renormalisation constant for GaN of 2.1–4.27$\times10^{-8}$ eVcm [109, 134]. From these results it can be seen that the rigid shift approximation does not accurately reproduce the bandgap renormalisation of this structure and hence the method detailed in section 3.5 with contributions from the Debye and exchange shifts is used in all future calculations.

4.10.2 Internal field.

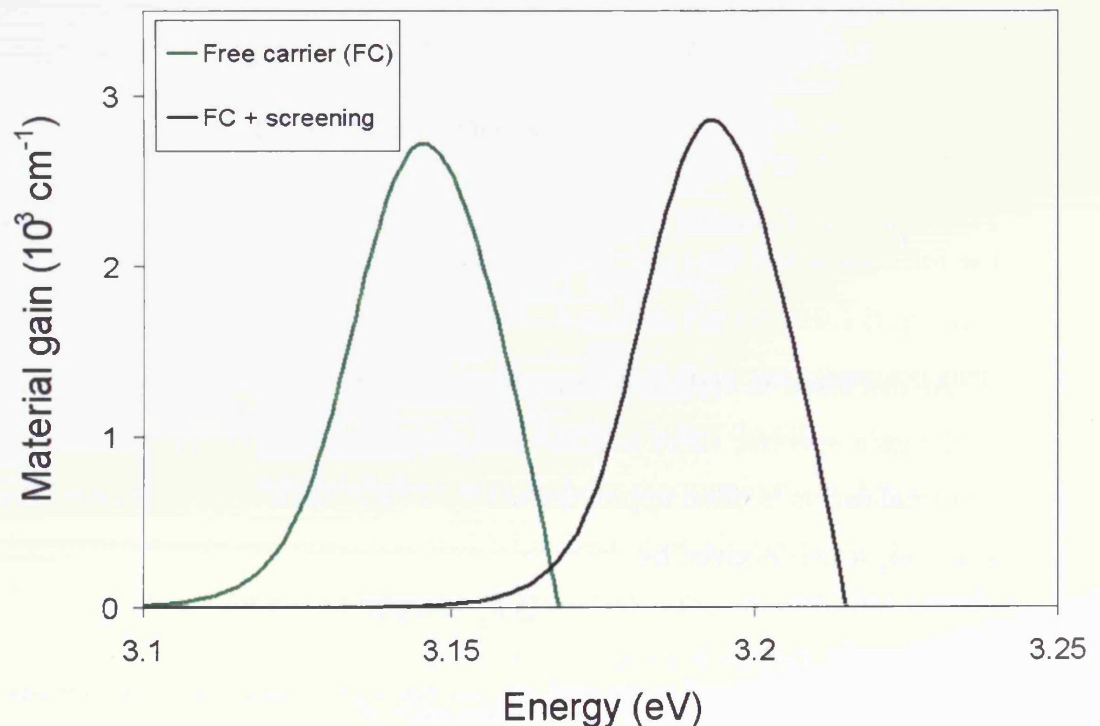

Figure 4.10.4: The gain spectrum calculated at the level of free carrier theory (FC) with and without screening of the internal field .

The effects of screening of the internal field which was discussed in chapter 2 and section 4.5 on the gain is shown in Figure 4.10.4. The unscreened internal field has a value of $E_{int}(0)$=1.23 MVcm^{-1} and at threshold this is reduced to $E_{int}(N)$=0.9 MVcm^{-1} due to screening. It can be seen that screening of the internal field causes an energy blue–shift of 50 meV and increases the gain peak by 5 %.

4.10.3 Coulomb enhancement.

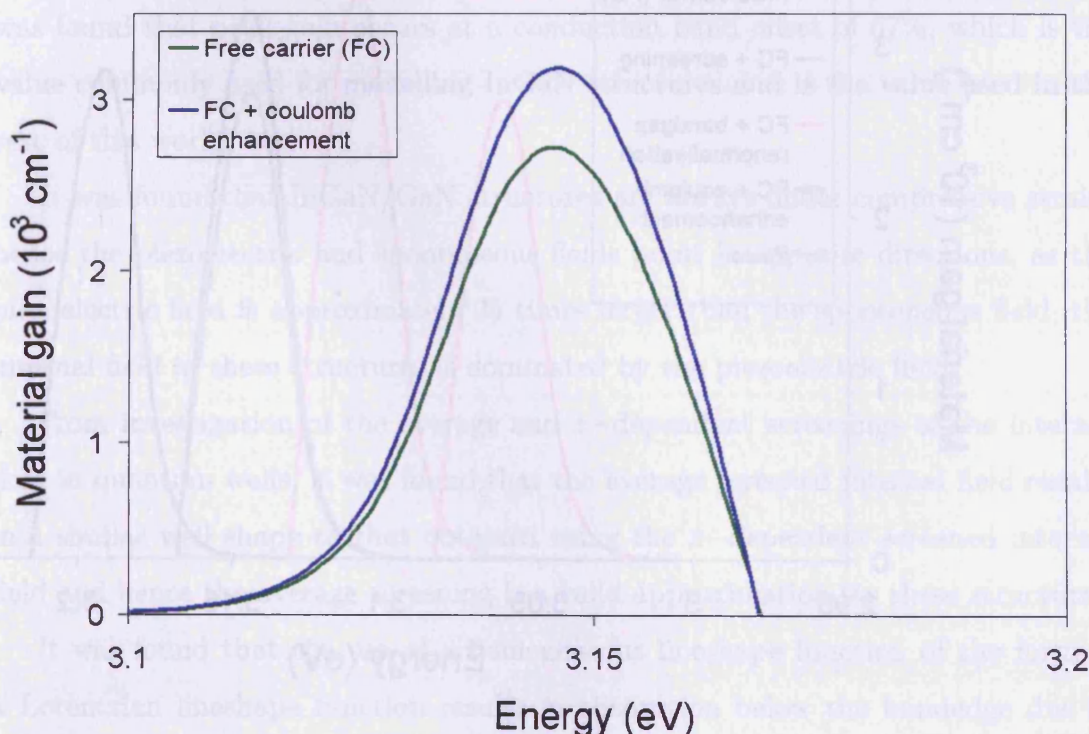

Figure 4.10.5: The gain spectrum calculated at the level of free carrier theory (FC), with and without Coulomb enhancement.

The Coulomb enhancement which was discussed in chapter 3, is given by the factor $\frac{1}{1-q(k)}$ in equation 3.3.22. In Figure 4.10.5, it can be seen that at threshold the Coulomb enhancement has no effect on the energy of the gain spectrum, but causes an increase in the gain of 18 % compared to the free carrier case. The Coulomb enhancement is only valid above the Mott density as it neglects the effects of bound

electron–hole states. The Mott density occurs when the screening length given by equation 3.4.23 is equal to the Bohr radius. The Mott density for this structure is $N = 1.0 \times 10^{16}\mathrm{m}^{-2}$, which corresponds to a value of approximately 3 nm for the Bohr radius and screening length.

4.10.4 Pade model.

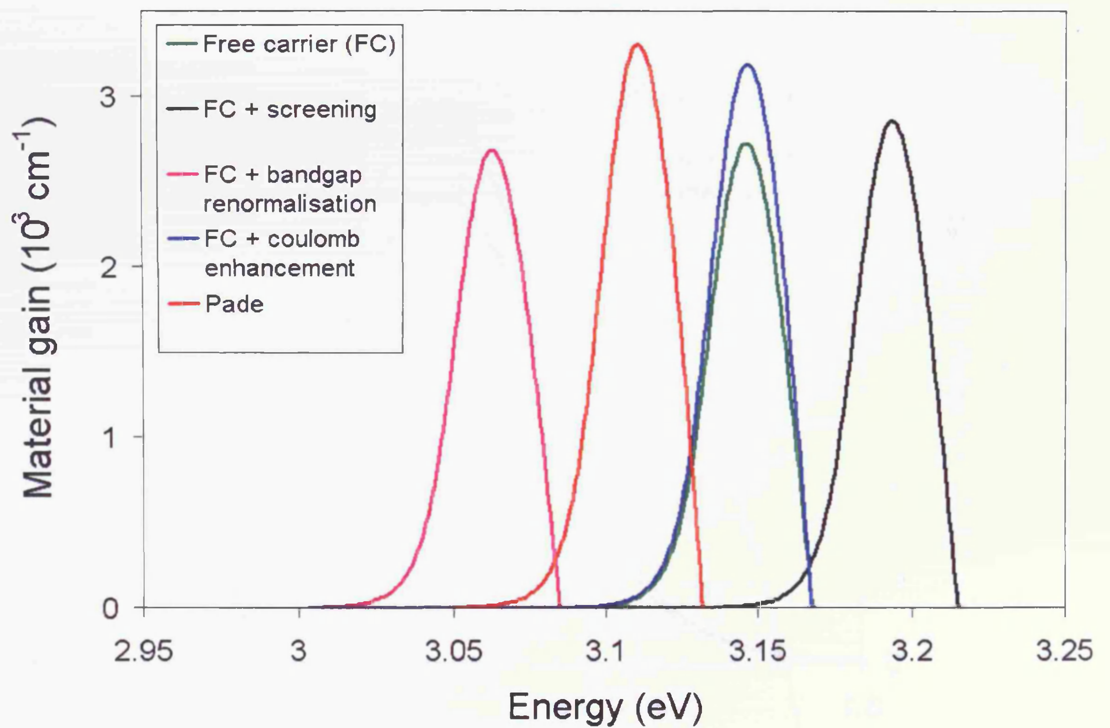

Figure 4.10.6: Gain spectra for different contributions to the Pade model : free carrier, bandgap renormalisation, screening of the piezoelectric field, Coulomb and full Pade.

The gain at the level of the Pade approximation is given by equation 3.3.22 and in Figure 4.10.6 the different contributions to the Pade model are shown. It can be seen that between the free carrier and the Pade models, there is a energy red–shift of 35 meV due to contributions from the bandgap renormalisation and screening of the internal field. In addition the gain is increased by 18 % mainly due to the

Coulomb enhancement.

4.11 Summary.

The bandgap of InGaN structures was calculated from interpolation from the binary values where a value for the bandgap of InN that does not follow the common–cation rule was used. A larger value of InN bandgap would blue–shift and reduce the intensity of the gain spectrum. From investigation of the band offset ratio it was found that peak gain occurs at a conduction band offset of 67%, which is the value commonly used for modelling InGaN structures and is the value used in the rest of this work.

It was found that InGaN/GaN structures are always under compressive strain, hence the piezoelectric and spontaneous fields point in opposite directions, as the piezoelectric field is approximately 25 times larger than the spontaneous field, the internal field in these structures is dominated by the piezoelectric field.

From investigation of the average and z−dependent screenings of the internal field in quantum wells, it was found that the average screened internal field results in a similar well shape to that obtained using the z−dependent screened internal field and hence the average screening is a valid approximation for these structures.

It was found that the use of a homogeneous lineshape function of the form of a Lorentzian lineshape function results in absorption below the bandedge due to the long tails of the Lorentzian function, this absorption was eliminated by the use of a sech lineshape function. The homogeneous lineshape function, contains the homogeneous lineshape factor, γ, which can be used to a certain extent to fit the gain peak, within the range of $\gamma = 1 - 3 \times 10^{13}\mathrm{s}^{-1}$. A value of $\gamma = 1 \times 10^{13}\mathrm{s}^{-1}$ is used in the rest of this work. It was found that the use of the Henry formula to obtain the spontaneous emission from gain, results in a discontinuity due to broadening effects, hence the spontaneous emission spectra presented in this thesis were calculated using the first principles approach.

The effects on the gain spectra of the different contributions to the Pade model

were investigated. It was found that between the free carrier and the Pade models at the threshold carrier density of $N = 5.85 \times 10^{16}\mathrm{m}^{-2}$, there is a energy red-shift of 180 meV due to contributions from the bandgap renormalisation and the screened internal field, and the gain is increased by 18 % mainly due to the Coulomb enhancement. In addition the rigid shift approximation, which is proportional to the square root of the carrier density, was found to be a poor approximation for the bandgap renormalisation in this structure. Also because the Coulomb enhancement is only valid above the Mott density, the model can only be used above a carrier density of $N = 1 \times 10^{16}\mathrm{m}^{-2}$ for this structure.

Chapter 5

Measurement of the internal field.

The internal field in InGaN based quantum wells, as discussed in chapter 2, is of the order of MVcm^{-1} which is almost an order of magnitude larger than in other III–V materials such as GaAs [48, 49, 135]. This internal field skews and breaks the symmetry of the well, causing spatial separation of the electron and hole wavefunctions [74, 80]. This reduction in the electron hole overlap function affects the emission wavelength [136], the oscillator strength [71] and the recombination lifetimes [66, 94], hence an accurate value of the internal field is essential in understanding the properties of these devices. The majority of approaches to determine the internal field, have relied upon counteracting the quantum confined Stark effect with an externally applied reverse bias and measuring properties of the quantum well as a function of this applied reverse bias. The method of reverse bias photocurrent absorption is discussed in section 5.2 and the calculation of the internal field from the reverse bias is detailed in section 5.3. Using these methods there have been large reported differences between the theoretical and experimental results [65]. I believe this is due to an inappropriate approximation for the electric field within the depletion region, which is used in the analysis of experimental data, and in section 5.4 a more exact method is proposed and comparison with published work is made in section 5.5.

Using this method, in section 5.6.1 the strength of the internal field of another

InGaN *p–i–n* structure is measured, using reverse bias photocurrent absorption spectroscopy detailed in section 5.6.2 and using microscopic theory based on the screened Hartree–Fock approximation detailed in section 5.6.3. In section 5.7 comparisons between the theoretical results and experimental photocurrent absorption measurements are made. Finally in section 5.8 the subject is reviewed and conclusions made.

5.1 Introduction.

Table 5.1.1: Internal field in InGaN/GaN quantum wells.

% In	Field MVcm^{-1}
3	0.11 [82]
5	0.3 [87]
7	1.1 [137]
9	1.4 [137]
10	0.35 [136]
10	0.9 [93]
12	1.6 [138]
13	1.1 [74]
15	0.5 [83]
15	2.1 [66, 139]
16	1.2 [65]
18	1.1 [140]
20	2.1 [66]
22	3.1 [138]
23	1.7 [68]
23	1.9 [68]
25	1.4 [61]

The strain induced piezoelectric field strongly affects the electronic and optical properties, hence it should be taken into account when designing and fabricating nitride based devices [65, 73]. However, the data concerning the physical properties of InGaN is still evolving and is sometimes controversial. Studies completed previously, with results summarised in table 5.1.1 and Figure 5.1.1, display a large

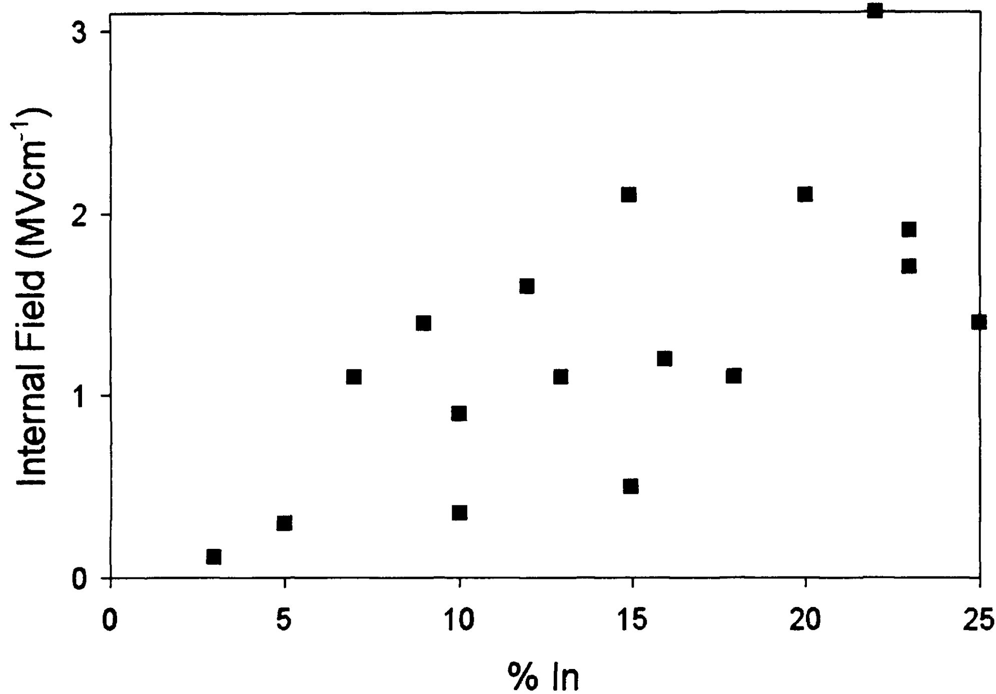

Figure 5.1.1: The increase in internal field with % In from published results [61, 65, 66, 68, 82, 83, 87, 93, 136, 137, 139? , 140].

spread of values for the internal field. As described in sections 2.3 and 4.5 the internal field should increase with increasing indium content and this is the broad trend observed in figure 5.1.1. Of course some allowances must be made for the uncertainty in the indium content and material quality [3], but the spread in the experimentally determined data is very large,

As discussed in chapter 2, the spontaneous polarization is small at InGaN/GaN interfaces, hence the internal field in these structures is dominated by the piezoelectric field [61, 141, 142]. Samples with similar indium concentrations are expected to have similar internal fields [4], but reported values of the internal field [66, 83], for the same nominal indium content can vary up to a factor of four, which is far greater than the expected error due to unintended variations in the indium content.

The method of reverse bias has previously been used to measure the internal field [65, 66, 68, 137]; this is done by varying the reverse bias and measuring the change in an observed property of the structure. In the work of Jho et al. [66],

Takeuchi et al. [65] and Lai et al. [68] the method of photoluminescence has been used and the shifts in the energy of the photoluminescence peak measured. Renner et al. [137] performed electroabsorption measurements and the minimum of the absorbed light power according to the Franz–Keldysh effect was observed.

5.2 Reverse bias photocurrent.

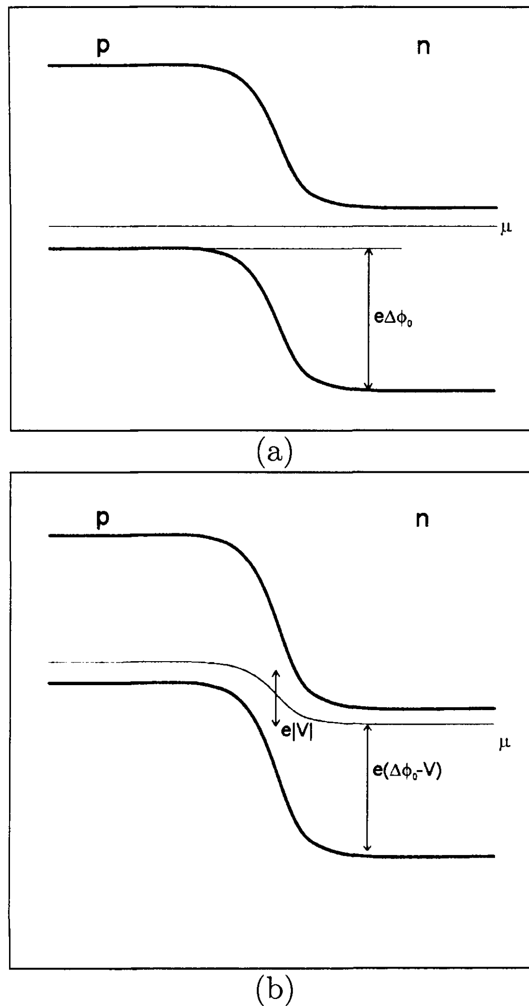

Figure 5.2.1: A p–i–n junction under zero bias (a) and reverse bias (b) [143].

The method of reverse bias photocurrent is one approach to investigating the internal field and in this section a broad introduction is presented. The experimental work performed by Pope [63], using reverse bias photocurrent is presented in

section 5.6.2 and contains more explicit details.

Photocurrent absorption is the generation of electron hole pairs, when the sample is illuminated with incident light of photon energy larger than the energy bandgap. The internal *p–i–n* field within the device, separates the electron hole pairs and the resulting current is measured, this is covered in further detail in section 5.6.2. By applying a reverse bias, V, the *p–i–n* junction exhibits rectifying behaviour and by comparing figures 5.2.1 (a) and (b), it can be seen that as the internal *p–i–n* field within the device is increased, the efficiency of the sweeping away of the electron hole pairs is increased. Neglecting the internal field, the measured signal, which corresponds to the extracted photogenerated carriers, is expected to increase with reverse bias, reaching a plateau when all the electron hole pairs are swept out.

The internal field present in the well due to strain, is opposed by the field across the *p–i–n* junction, hence the reverse bias opposes the internal field reducing the effect of the induced quantum confined Stark effect and this is shown in Figure 5.2.2. At low bias the well is skewed due to the internal field, and increasing the reverse bias causes an increase in the amplitude and energy of the absorption peak, until at a critical bias the contributions from the applied bias and the internal field are equal and opposite. At this critical bias, the quantum well is square [12, 118] and the overlap of electron and hole wavefunctions, the amplitude of the absorption, and the ground state transition energy are maximised. At higher bias the well is skewed in the opposite sense, as the bias dominates the effective internal field and the amplitude and energy of the absorption peak decrease. The change in the well shape due to the internal and applied fields is shown in Figure 5.2.2, for small, critical and large values of applied bias, from left to right respectively.

Therefore with increasing reverse bias, the absorption intensity increases, reaches a maximum value at the critical reverse bias and then decreases again. Similarly, the energy of the peak absorption reaches a maximum value and then decreases again as the reverse bias is increased. The energy shift of the photoluminescence peak of InGaN/GaN devices with increasing applied reverse bias, has been observed in

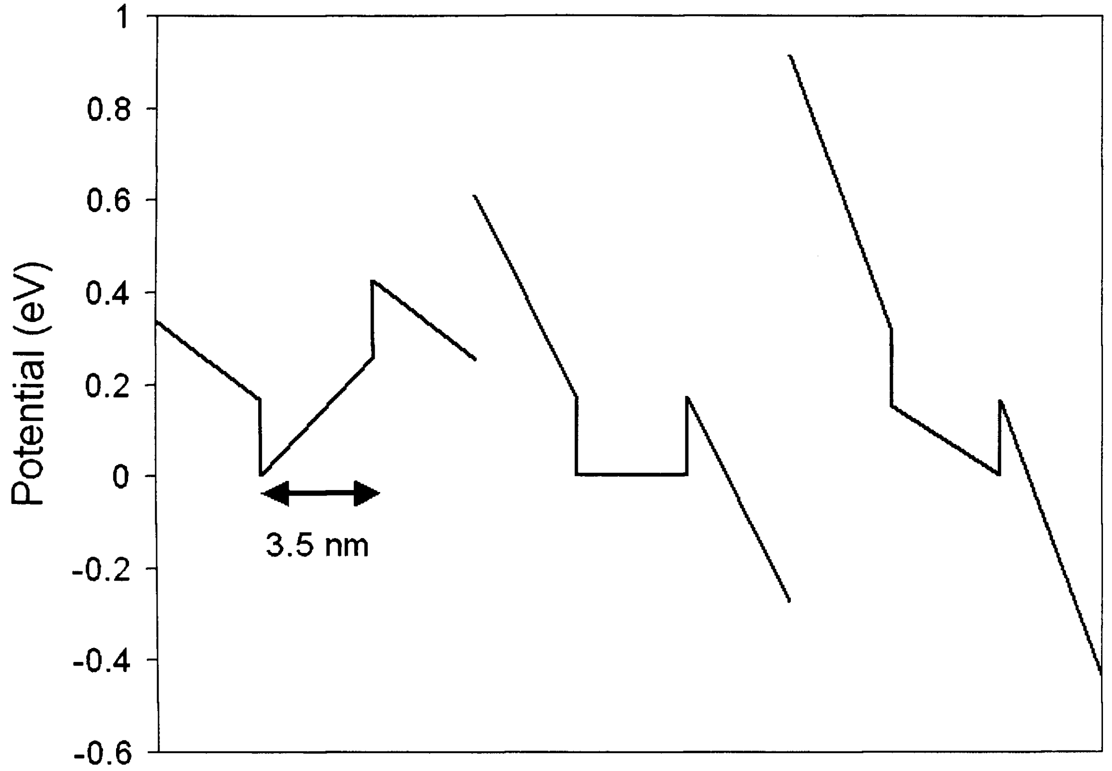

Figure 5.2.2: Well shape due to the internal and applied fields for small, critical and large values of applied bias, from left to right.

many published works [65, 66, 68, 79]. Hence, by observing this plateau region with respect to the reverse bias, the internal field in InGaN structures can be derived and this is discussed in section 5.3.

5.3 Effective internal field.

As discussed in section 5.2, the applied reverse bias opposes the internal field, hence the effective internal field, E, in the well is related to the reverse bias, V, using [66]

$$E(V) = \frac{\Delta\phi_0 - V - E_{int}N_wL_w}{d_u + d_d(V)/2} + E_{int}, \tag{5.3.1}$$

where E_{int}, N_w, $\Delta\phi_0$, d_d and d_u are the internal field, number of quantum wells, built–in potential and the depletion and active widths respectively. The internal

field E_{int}, is the sum of the fields due to the piezoelectric effect and the spontaneous polarization, but as discussed in chapter 2 and section 5.1, the spontaneous polarization contribution is small. At the critical bias, when the well is square, equation 5.3.1 simplifies as the effective internal field is zero, $E = 0$. For a *p–i–n* structure the width of the active i–region, d_u, is given by

$$d_u = N_w L_w + (N_w + 1) L_b, \tag{5.3.2}$$

where L_w and L_b are the widths of the well and barrier regions respectively. Previously, the value of the internal field, E_{int}, obtained using the experimental method detailed in section 5.2 and equation 5.3.1, has been up to a factor of two smaller than that obtained from theoretical calculations. I believe this is due the fact that the active region is not taken into account when calculating the penetration of the electric field into the doped regions, which is given by the depletion width, d_d. The depletion width, d_d, in equation 5.3.1, varies with the applied bias, V, of the junction, hence to understand this relationship fully the spatial variation of charge and field in a *p–i–n* junction has to be taken into account and this is investigated in section 5.4.

5.4 Depletion width.

The p and n–doping of GaN is normally done with Mg and Si which replace a Ga and N atom respectively. As is well known when the p–type and n–type materials are placed in contact with each other, there is a net diffusion of electrons into the p–type material and holes into the n–type material. This is caused by the concentration gradients of electrons and holes and occurs until the chemical potentials are equalised [45]. A consequence of this is that a region of the n–type layer of width, d_n, is depleted of electrons and positive charge is located on the ionised donor. Similarly for the p–type layer, there is a negative charge region of width, d_p. The depletion width, d_d, which appears in equation 5.3.1, is dependent

on the applied bias and is written as

$$d_d(V) = d_p(V) + d_n(V), \tag{5.4.1}$$

which is the sum of the individual p and n−type depletion widths. The depletion width can be calculated using methods based on the p–n and p–i–n approximations, this is discussed in sections 5.4.1 and 5.4.2 respectively, and comparisons with a simulation software package are also made.

5.4.1 Depletion width: p–n junction approximation.

It is a common assumption in the calculation of the internal field [65, 66] that the depletion width, d_d, in a p–i–n structure can be approximated using the abrupt p–n junction approximation. This derivation is covered in the work of Hook and Hall [49] for example and here the result is just quoted as

$$d_d(V) = \sqrt{\frac{2\epsilon\epsilon_0\Delta\phi}{e(N_A + N_D)}\left(\frac{N_A}{N_D} + \frac{N_D}{N_A}\right)}, \tag{5.4.2}$$

where N_A and N_D are the acceptor and donor doping densities and $\Delta\phi$ is the difference in the electrostatic potential, which is discussed in section 5.4.2. For this equation to be valid i.e. for the p–n approximation to accurately describe a p–i–n junction, the field across the active region must be zero or the active region must be very small $d_u \rightarrow 0$.

However, there is a constant field, $E \neq 0$, across the active region for all values of reverse bias, which can be verified using one of the many modelling packages that are available that self consistently solve the Poisson and Schrodinger equations, for example Simwin^{TM} [144]. Simwin^{TM} is based upon a one dimensional drift diffusion simulator and uses equations based on the electrical, optical and the thermal properties, to simultaneously converge on the solution. In Figure 5.4.1, the field across the p–i–n structure [65], obtained using Simwin^{TM} is shown and the constant field, $E \neq 0$, in the active region can be clearly seen.

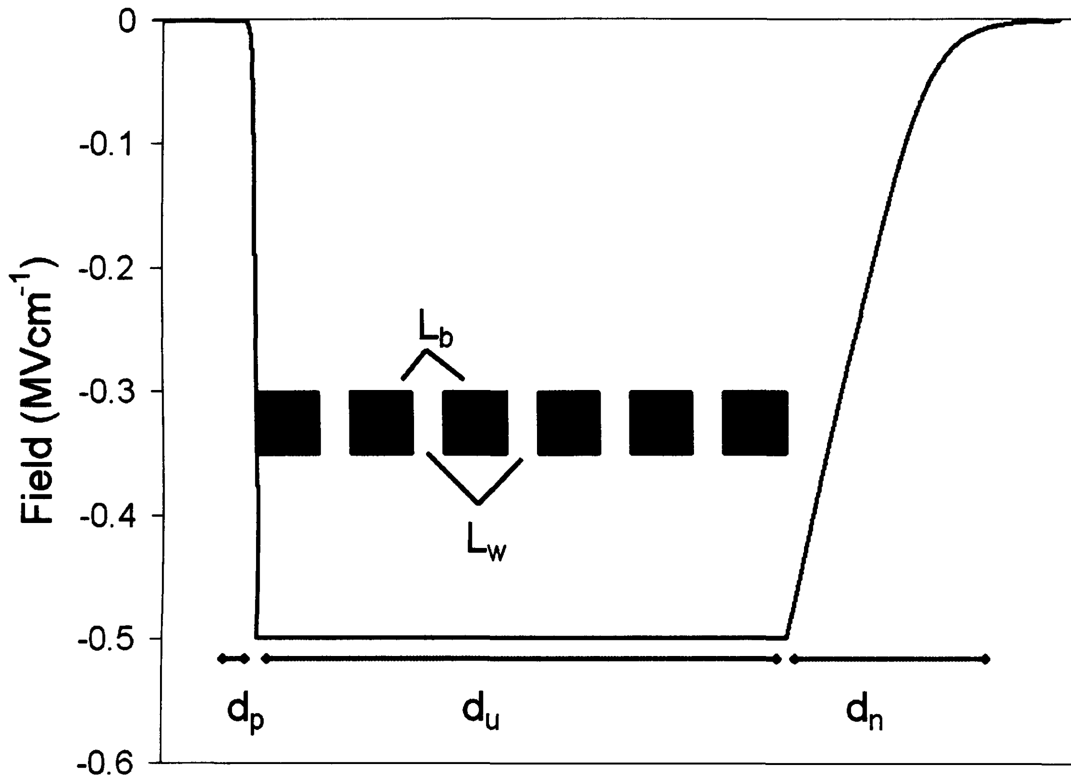

Figure 5.4.1: Calculation of the field across the *p–i–n* structure [65] using Simwin^{TM} [144], with a schematic of the active region superimposed for reference.

In the work of Takeuchi et al. [65], the *p–n* junction approximation was used to describe a *p–i–n* junction and in Figure 5.4.2 this approximation is compared with Simwin^{TM} for a range of applied biases. It is clear that the values obtained for the depletion width from the *p–n* approximation are up to a factor of two times larger than those obtained using Simwin^{TM}, and hence the *p–n* approximation does not produce accurate results for this structure. The observed constant field, $E \neq 0$, across the active region in Figures 5.4.1 and 5.4.2, is the main cause of the discrepancy between the results obtained using the *p–n* junction approximation and Simwin^{TM}. This is due to the fact that residual doping level in the *i*—region is very small and any applied voltage is dropped entirely across the *i*—region [12]. The *p–n* junction approximation would be valid for this structure if the field rapidly fell to zero at the *p–i* interface and rose again at the *i–n* interface i.e the field across the

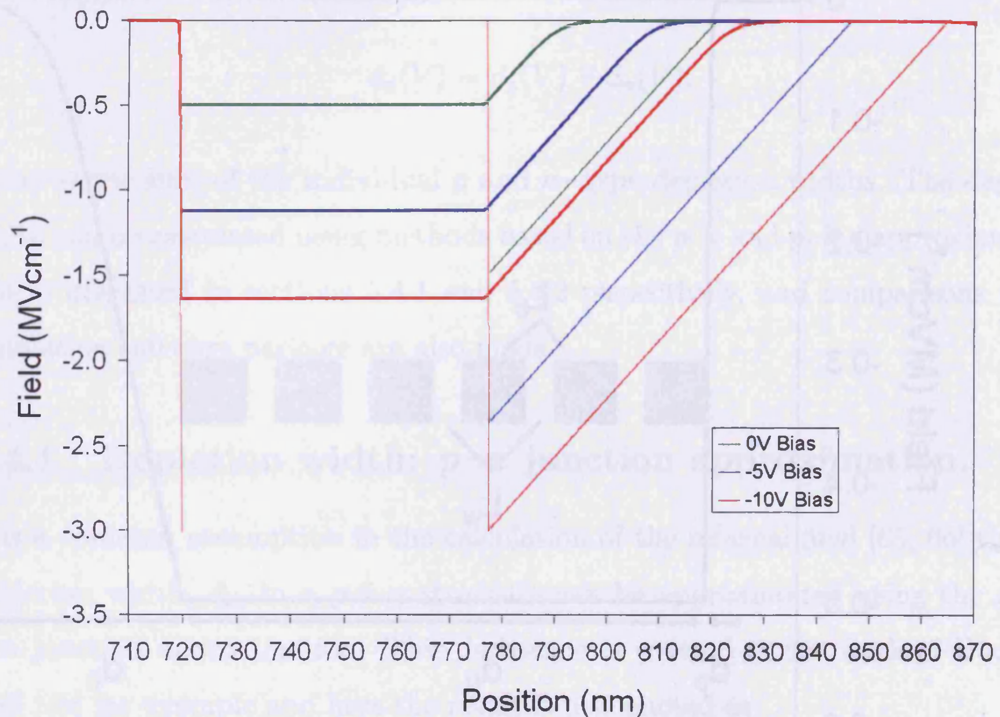

Figure 5.4.2: The electric field across a p–i–n structure (p–i interface at 720 nm) using Simwin^{TM} [144] (thick lines) and an analytic method based on the p–n approximation (equation 5.4.2) (thin lines), at biases of 0, -5 and -10 V.

active region was zero, or if the width of the active region was small $d_u \rightarrow 0$. In both of these situations there is no contribution to the voltage from the active region. Neither of these cases apply to the structure used by Takeuchi et al. [65], hence the p–n junction approximation overestimates the depletion width and the maximum field in the well. Although Simwin^{TM} provides a solution for the depletion width, the simulation needs to rerun for each new value of applied bias and the solution for the depletion width read off the resulting graphical display. An analytic model which can be included in equation 5.3.1 for the total field across a p–i–n junction would offer huge gains in time and simplicity. Hence in section 5.4.2, an equation for the depletion width which includes the constant non–zero field across the active region is developed.

5.4.2 Depletion width: *p–i–n* method.

As discussed in section 5.4.1, the *p–n* junction approximation overestimates the depletion width. Hence in this section, an equation for the depletion width, based on the *p–i–n* junction method, incorporating a constant field in the active region is derived. This is done by using Poisson's equation to relate the field and potential difference across the structure. The difference in electrostatic potential of a *p–i–n* junction can be written as

$$\begin{aligned} \Delta\phi &= \phi(\infty) - \phi(-\infty) \\ &= \Delta\phi_0 - V, \end{aligned} \tag{5.4.3}$$

where $\Delta\phi_0$ is the built in voltage and V is the applied bias, where forward bias $V > 0$ and reverse bias $V < 0$. The built in voltage, $\Delta\phi_0$, can be derived from the Fermi level separation

$$\begin{aligned} e\Delta\phi_0 &= \mu_n - \mu_p \\ &= E_g + k_B T \ln\left(\frac{N_D N_A}{N_C N_V}\right), \end{aligned} \tag{5.4.4}$$

where N_C and N_V are the density of states in the conduction and valence bands, and T and k_B are the temperature and Boltzman's constant respectively [145]. Using the intrinsic electron carrier concentration

$$n_i = \sqrt{N_C N_V} e^{\left(\frac{-E_g}{2k_B T}\right)}, \tag{5.4.5}$$

and substituting into equation 5.4.4 gives the built–in potential as [45]

$$\Delta\phi_0 = \frac{k_B T}{e} \ln\left(\frac{N_D N_A}{n_i^2}\right). \tag{5.4.6}$$

From investigations using Simwin^{TM}, which are shown in Figure 5.4.2, it can be seen that there is a constant non–zero field, $E_i \neq 0$, across the active region, d_u and

a linear reduction of the field across the p and n type depletion regions, given by d_p and d_n respectively. Hence the depletion approximation which assumes that the p and n regions have well defined edges and that the carrier density falls to zero very rapidly at the depletion boundary is valid for this situation. The charge contained in the p and n regions is equal, hence [45]

$$N_A e d_p = N_D e d_n, \tag{5.4.7}$$

where N_A and N_D are the acceptor and donor doping densities respectively. As the charge must be equal on both sides of the junction, the weaker doped side must have a larger depletion width and this can be seen in Figure 5.4.2. Hence the doping impurities are ionised further from the junction in the lighter doped material, to equal the charge in the more heavily doped side [30].

Using 5.4.7, the charge density for a p–i–n structure can be written as

$$\rho(z) = \begin{cases} -N_A e & -d_p < z < 0 \\ 0 & 0 < z < d_u \\ +N_D e & d_u < z < d_u + d_n \\ 0 & -d_p > z > d_u + d_n, \end{cases} \tag{5.4.8}$$

where $z = 0$ is defined as the p–i interface. By using Poisson's equation

$$\frac{\mathrm{d}^2\phi}{\mathrm{d}z^2} = -\frac{\rho(z)}{\epsilon\epsilon_0}, \tag{5.4.9}$$

the electric field can be written as

$$E(z) = -\frac{\mathrm{d}\phi}{\mathrm{d}z} = \begin{cases} -\frac{N_A e}{\epsilon\epsilon_0}(z + d_p) & -d_p < z < 0 \\ -\frac{N_A e}{\epsilon\epsilon_0} d_p & 0 < z < d_u \\ +\frac{N_D e}{\epsilon\epsilon_0}(z - d_u - d_n) & d_u < z < d_u + d_n \\ 0 & -d_p > z > d_u + d_n, \end{cases} \tag{5.4.10}$$

where the assumption that there is a constant field in the i region $(0 < z > d_u)$ has been used.

The difference in electrostatic potential given by equation 5.4.3, can be equated to the integral of the electric field

$$\Delta\phi = -\int_{-\infty}^{\infty} E(z)\mathrm{d}z, \tag{5.4.11}$$

this can be rewritten as

$$\Delta\phi = -\int_{-d_p}^{d_u+d_n} E(z)\mathrm{d}z, \tag{5.4.12}$$

as there is only a field present across the p and n type depletion regions and the active region. By further splitting, the integral can be rewritten as

$$\Delta\phi = -\int_{-d_p}^{0} E(z)\mathrm{d}z - \int_{0}^{d_u} E(z)\mathrm{d}z - \int_{d_u}^{d_n+d_u} E(z)\mathrm{d}z, \tag{5.4.13}$$

and by substitution of equation 5.4.10 gives

$$\Delta\phi = \frac{e}{\epsilon\epsilon_0} \left[+N_A \int_{-d_p}^{0} (z + d_p)\mathrm{d}z + N_A \int_{0}^{d_u} d_p \mathrm{d}z - N_D \int_{d_u}^{d_u+d_n} (z - d_u - d_n)\mathrm{d}z \right], \tag{5.4.14}$$

were uniform doping is assumed. Performing the integration gives

$$\Delta\phi = \frac{e}{2\epsilon\epsilon_0} \left(N_A d_p^2 + 2 d_n N_D d_u + N_D d_n^2 \right). \tag{5.4.15}$$

The constant field across the active region, E_i, can be found by integrating the charge density in the p type depletion region, $\rho = -N_A e$, over the width of the p type depletion region, which can be written as

$$E_i = -\frac{eN_A}{\epsilon\epsilon_0} d_p. \tag{5.4.16}$$

Thus, by substitution of equation 5.4.7 into equation 5.4.15, the potential can be rewritten as

$$\Delta\phi = -\frac{eN_A}{\epsilon\epsilon_0}d_p\left(d_u + \frac{d_p + d_n}{2}\right), \quad (5.4.17)$$

and by substitution of equation 5.4.7, this can be written as a quadratic in terms of d_n

$$0 = \frac{d_n^2}{2}\frac{N_A + N_D}{N_A} + d_u d_n - \frac{\Delta\phi\epsilon\epsilon_0}{eN_D}. \quad (5.4.18)$$

Solving using the quadratic formula [146], the n type depletion width can be written as [147]

$$d_n = \frac{-d_u \pm \sqrt{d_u^2 + 2(\frac{N_D+N_A}{N_A})\frac{\Delta\phi\epsilon\epsilon_0}{eN_D}}}{(\frac{N_D+N_A}{N_A})}, \quad (5.4.19)$$

and using equation 5.4.7 for the charge contained in each region, the p type depletion width, d_p, can be similarly written as

$$d_p = \frac{-d_u \pm \sqrt{d_u^2 + 2(\frac{N_D+N_A}{N_A})\frac{\Delta\phi\epsilon\epsilon_0}{eN_D}}}{(\frac{N_D+N_A}{N_D})}. \quad (5.4.20)$$

By the use of equations 5.4.1, 5.4.19 and 5.4.20 the total depletion width can be written as

$$d_d = -d_u \pm \sqrt{d_u^2 + 2\left(\frac{N_D + N_A}{N_A N_D}\right)\frac{\Delta\phi\epsilon\epsilon_0}{e}}, \quad (5.4.21)$$

which is the sum of the p–type and n–type depletion regions. By comparison with equation 5.4.2, which is the depletion width obtained using the p–n approximation, equation 5.4.21 can be rewritten as

$$d_{d_{(p-i-n)}} = -d_u \pm \sqrt{d_u^2 + d_{d_{(p-n)}}^2}, \quad (5.4.22)$$

which is the depletion width under the p–i–n junction model $d_{d_{(p-i-n)}}$ in terms of the active region d_u and the depletion width under the p–n approximation $d_{d_{(p-n)}}$. The depletion width, equation 5.4.21, obtained using the p–i–n junction model, can be simplified to equation 5.4.2, which was obtained using the p–n junction

approximation, either if the active region is infinitely narrow, $d_u \rightarrow 0$, or if the field across the active region is zero, in both cases there is no contribution to the voltage from the active region. As either of these situations do not apply to a p–i–n structure it is not consistent with the use of equation 5.3.1 or even a modified form of equation 5.3.1 where $d_u = 0$.

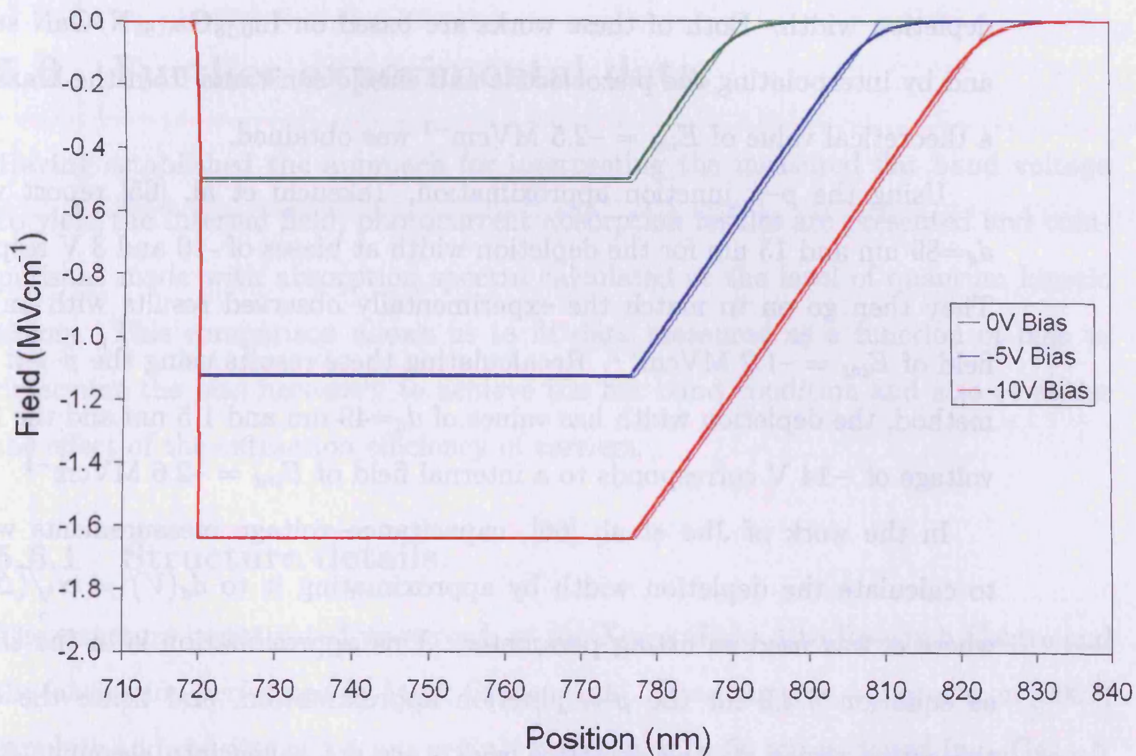

Figure 5.4.3: The electric field across a p–i–n structure (p–i interface at 720 nm) using Simwin^{TM} [144] (thick lines) and the p–i–n model (thin lines), at biases of 0, -5 and -10 V.

In Figure 5.4.3, the field across the structure using the p–i–n junction model given by equation 5.4.21 and Simwin^{TM} are compared. There is close agreement of the field and depletion width, between the two methods for all values of reverse bias. Having established the correct analytic approach to calculate the depletion width and hence the internal field, published work is reassessed in section 5.5.

5.5 Published results.

Applying these methods to published results is difficult, as in most cases the details published were insufficient to reassess the data.

However, in the case of Takeuchi et al. [65] and Jho et al. [66], we are able to reinterpret the experimental data including the effect of the active region on the depletion width. Both of these works are based on $In_{0.15}Ga_{0.85}N/GaN$ structures and by interpolating the piezoelectric and elastic constants from the binary values a theoretical value of $E_{int} = -2.5$ MVcm^{-1} was obtained.

Using the *p–n* junction approximation, Takeuchi et al. [65] report values of d_d=89 nm and 13 nm for the depletion width at biases of -10 and 3 V respectively. They then go on to match the experimentally observed results with an internal field of $E_{int} = -1.2$ MVcm^{-1}. Recalculating these results using the *p–i–n* junction method, the depletion width has values of d_d=49 nm and 1.5 nm and the flat band voltage of -14 V corresponds to a internal field of $E_{int} = -2.6$ MVcm^{-1}.

In the work of Jho et al. [66], capacitance–voltage measurements were used to calculate the depletion width by approximating it to $d_d(V) = \alpha\sqrt{(}\Delta\phi_0 - V)$ where α was used as fitting parameter. This approximation is in the same form as equation 5.4.2 for the *p–n* junction approximation, and hence the effects of the active region on the depletion width are not taken into account. At reverse biases of 0 V and –20 V Jho et al. calculate values of approximately 40 nm and 120 nm for the depletion width. The same values are obtained for a 20% indium structure even though the width of the active region is over twice as large as in the 15% indium structure. This compares to values of d_d=17 nm and 77 nm for the 15%, and 6 nm and 35 nm for the 20% indium structures, obtained using the *p–i–n* junction method. Hence from this we establish that the *p–n* junction approximation overestimates the depletion width by up to 60% in comparison to the *p–i–n* junction method for these structures. The 20% sample does not display the flat band condition within the reverse bias range presented in the paper by Jho et al, but for the 15% sample the flat band condition occurs at a voltage of

approximately –17 V. Using the *p–i–n* junction method we find that the flat band at –17 V for the 15% In sample can be fitted using a internal field of E_{int} = –2.6 MVcm^{-1}. Thus by including the effect of the active *i*–region, close correlation between the internal field determined using experimental and theoretical methods is observed.

5.6 Further experimental data.

Having established the approach for interpreting the measured flat band voltage to yield the internal field, photocurrent absorption results are presented and comparisons made with absorption spectra calculated at the level of quantum kinetic theory. This comparison allows us to fit data measured as a function of bias to determine the bias necessary to achieve the flat band condition and also to assess the effect of the extraction efficiency of carriers.

5.6.1 Structure details.

The structure investigated was grown at the Xerox, Palo Alto Research Centre and the fabrication performed by Mark Dineen [148]. The structure was grown on (0001) sapphire and consists of a 4 μm *p*–GaN buffer layer, a 50 nm *p*–doped $In_{0.02}Ga_{0.98}N$ defect reduction layer, 500 nm of $Al_{0.07}Ga_{0.93}N$ and 100 nm *p*–GaN. The active region consists of five 3.5 nm $In_{0.1}Ga_{0.9}N$ quantum wells embedded between 6.5 nm $In_{0.01}Ga_{0.99}N$ barriers. A 20 nm $Al_{0.2}Ga_{0.8}N$ barrier was used help prevent carrier leakage, the device was completed with 100 nm *n*–doped GaN, 500 nm of *p*–doped $Al_{0.07}Ga_{0.93}N$ and topped with 100 nm of *p*–GaN [148, 149]. The levels of donor (*n*–type) and acceptor (*p*–type) doping in the sample were $N_D = 2 \times 10^{18}$ cm^{-3} (Si) and $N_A = 1 \times 10^{20}$ cm^{-3} (Mg), respectively. As higher doping levels result in smaller depletion widths [12], the *n*–type depletion width is much smaller than the *p*–type for this sample. The composition and dimensions of the quantum well and barrier regions were obtained using X–ray diffraction of the sample [150], hence the

values are accurate to ±1 % and ±0.1 nm respectively [151].

5.6.2 Experimental details.

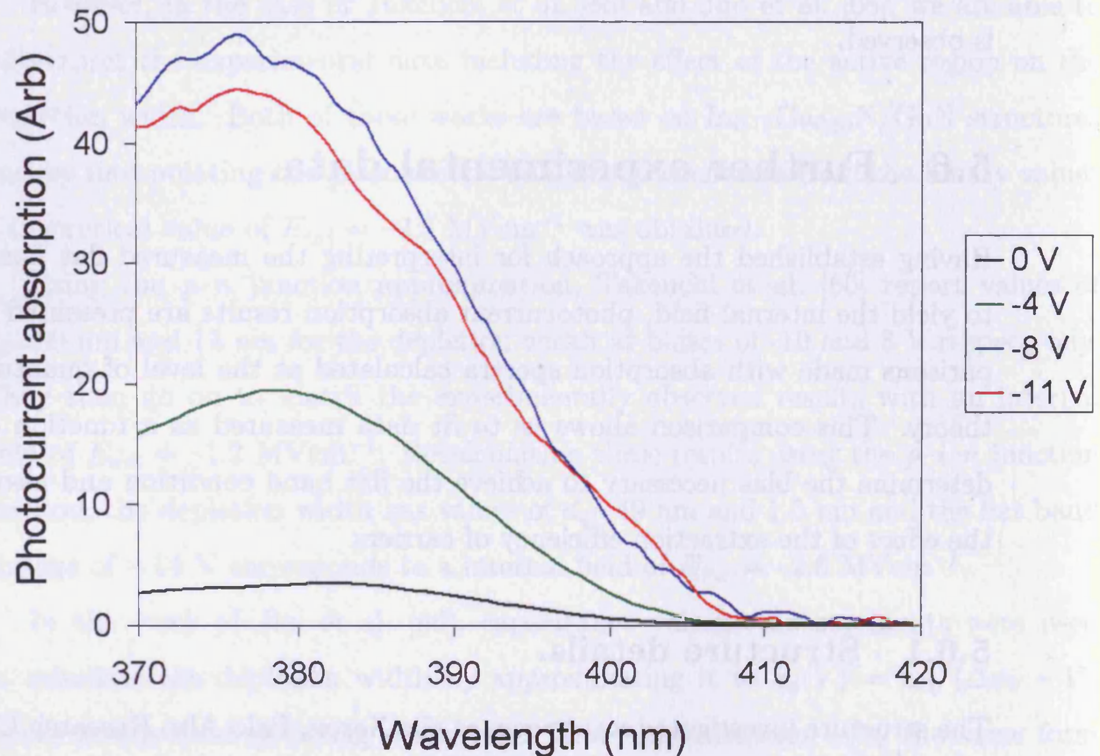

Figure 5.6.1: The experimental photocurrent absorption spectrum at reverse biases of 0, –4, –8 and –11 V [63].

The magnitude and energy of the peak of the absorption spectra as a function of reverse bias at room temperature were measured by Pope [63], using photocurrent absorption measurements as detailed in section 5.2, a method similar to the photovoltage experiments performed by Smowton et al. and Blood et al. [152, 153].

Monochromatic light obtained using a white light source and a monochromator, was passed through a collimator and focused on the end facet of the sample and a external DC bias was applied to the sample. The photo–generated signal was then sent to a lock–in amplifier, which amplifies the current and converts it to a voltage signal. The absorption spectrum was then obtained by rotation of the

monochromator. The effects of noise due to electric signals and background light were minimised by encasing the sample in a metal box.

A selection of the experimental absorption spectra for reverse biases of 0, –4, –8 and –11V is shown in Figure 5.6.1, from this the shift in energy and intensity due to the reverse bias was extracted. As can be seen the intensity increases with reverse bias until the critical bias is reached at –8 V, and at –11 V the intensity has decreased again Which is caused by dominance of the internal field at low bias and reverse bias at high bias. A low excitation power was used to obtain the photoluminescence spectra, this was done to minimise the effects of free carrier screening [138], which is discussed in section 2.5. Since the magnitude of the measured absorption signal depends upon the extraction of carriers from the device, which may be incomplete at low values of reverse bias [154], a bias dependent measured absorption signal at small bias is expected.

5.6.3 Theory.

In section 5.3, an analytical method to calculate the average effective field of a multi quantum well structure due to contributions from the applied bias and the internal field was developed. Hence the effect of the applied bias on the absorption spectra for a quantum well device can be investigated. Thus for each value of reverse bias, the depletion width, d_d and the average effective field, E, were calculated using equations 5.4.21 and 5.3.1 respectively. The effect of the field on the absorption spectra as a function of reverse bias was calculated using equation 3.3.22. As a low carrier density of 10^{10} cm^{-2} was used, the screening effects discussed in section 2.5 cause a reduction of less than 0.2% in the internal field. This agrees with the work of Jho et al. [66], who reported that screening effects only becomes important at carrier densities above 10^{12} cm^{-2}. Also as the quantum wells in the sample investigated are sufficiently thin, reduction of the internal field due to strain relaxation can be neglected.

5.7 Results.

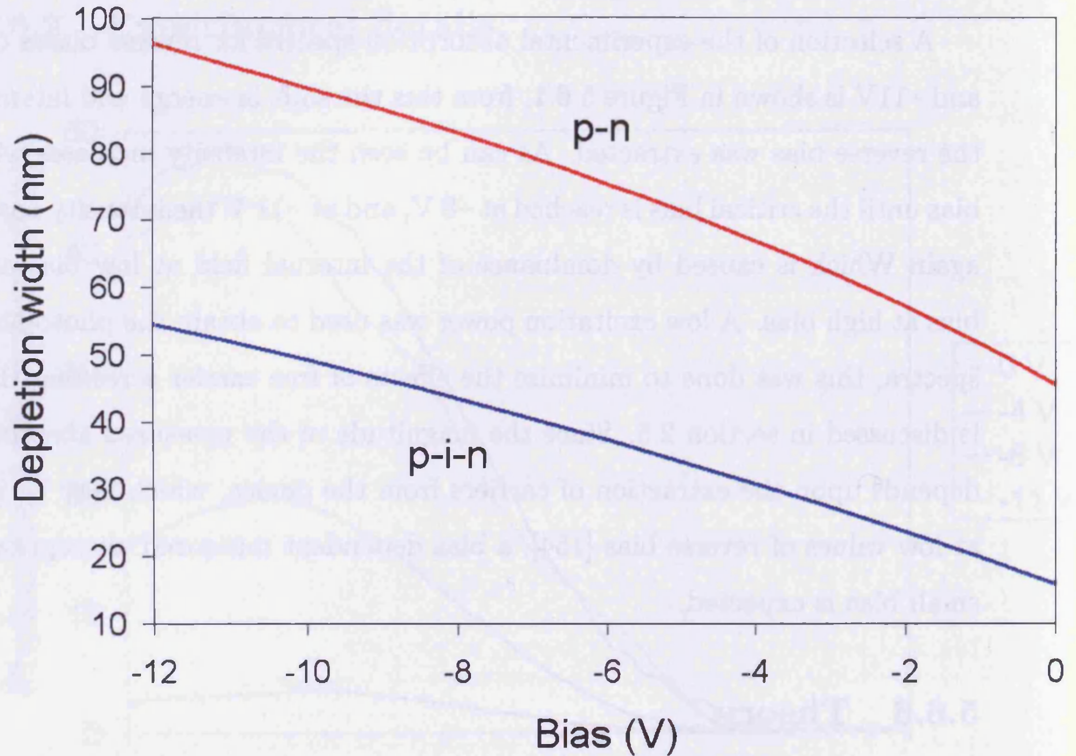

Figure 5.7.1: The depletion width, d_d, as a function of reverse bias V, using the p–n (red) approximation and p–i–n method (blue)

Using the p–i–n method given by equation 5.4.21, the depletion width d_d of the $In_{0.1}Ga_{0.9}N$ sample detailed in section 5.6.1, as a function of applied reverse bias V is shown in Figure 5.7.1. The depletion width obtained using the p–n approximation is also shown for comparison and demonstrates that the use of the p–n approximation significantly over estimates the depletion width and consequently leads to an underestimation of the internal field due to the piezoelectric effect and spontaneous polarization using equation 5.3.1.

The experimentally determined energy of the peak absorption is shown in Figure 5.7.2 (top) as a function of the applied reverse bias. The experimental data is fitted using the theoretical model where the internal field is the fitting parameter and the best fit is calculated for an internal field of E_{int} = −1.9 MVcm^{-1}. Which

Figure 5.7.2: Energy (top) and amplitude (bottom) of the peak absorption as a function of applied reverse bias V for measured (symbols) and calculated (line) values.

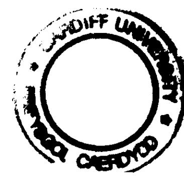

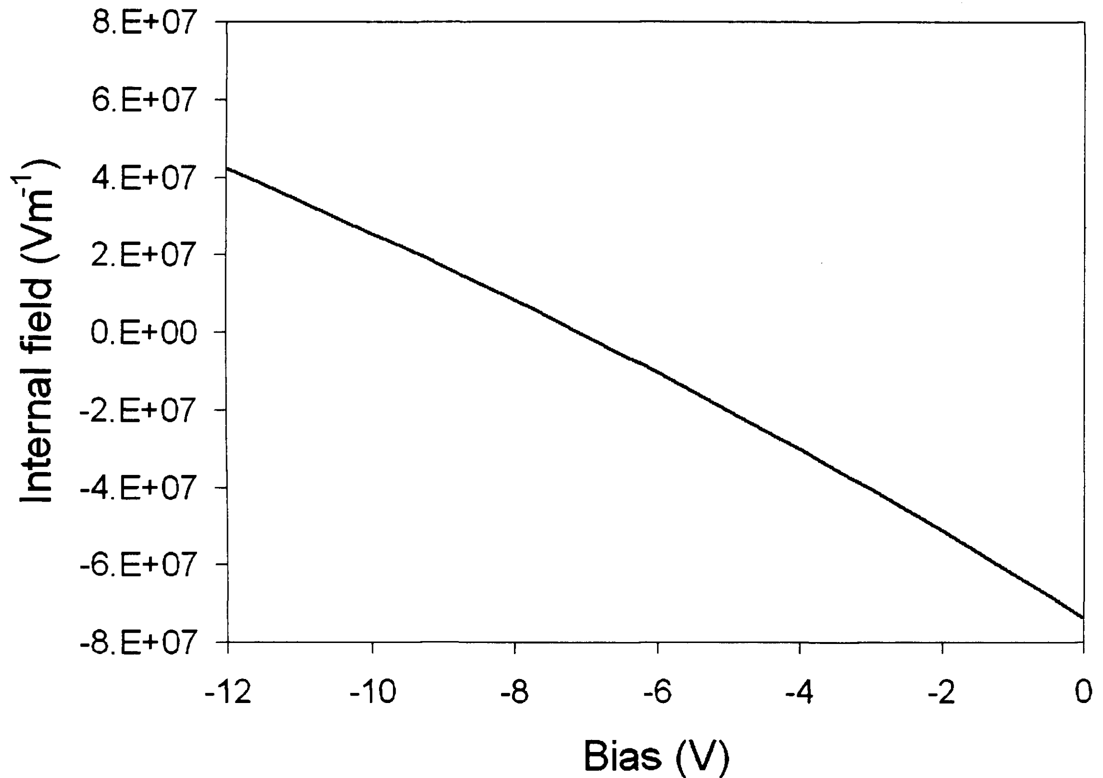

Figure 5.7.3: Variation of the internal field as a function of applied reverse bias V.

compares with –1.8 MVcm^{-1} obtained using the calculation when the material constants are obtained by interpolating the binary values, as discussed in section 5.5. The flat band condition (square well), occurs at a critical bias of approximately –8 V.

A comparison of the experimental and calculated results for the amplitude of the measured peak absorption is shown in Figure 5.7.2 (bottom) and shows there is good agreement at high values of bias but poor agreement at low bias. At low bias there is incomplete extraction of the carriers as discussed in section 5.6.2 and hence there is a reduction in the apparent absorption using photocurrent spectroscopy [154]. The comparison indicates that measurements of the amplitude of absorption using photocurrent spectroscopy are inappropriate to determine the internal field.

Having fitted the experimental energy shift with a field of E_{int} = –1.9 MVcm^{-1}, the variation of the internal field given by equation 5.3.1, is shown in Figure 5.7.3.

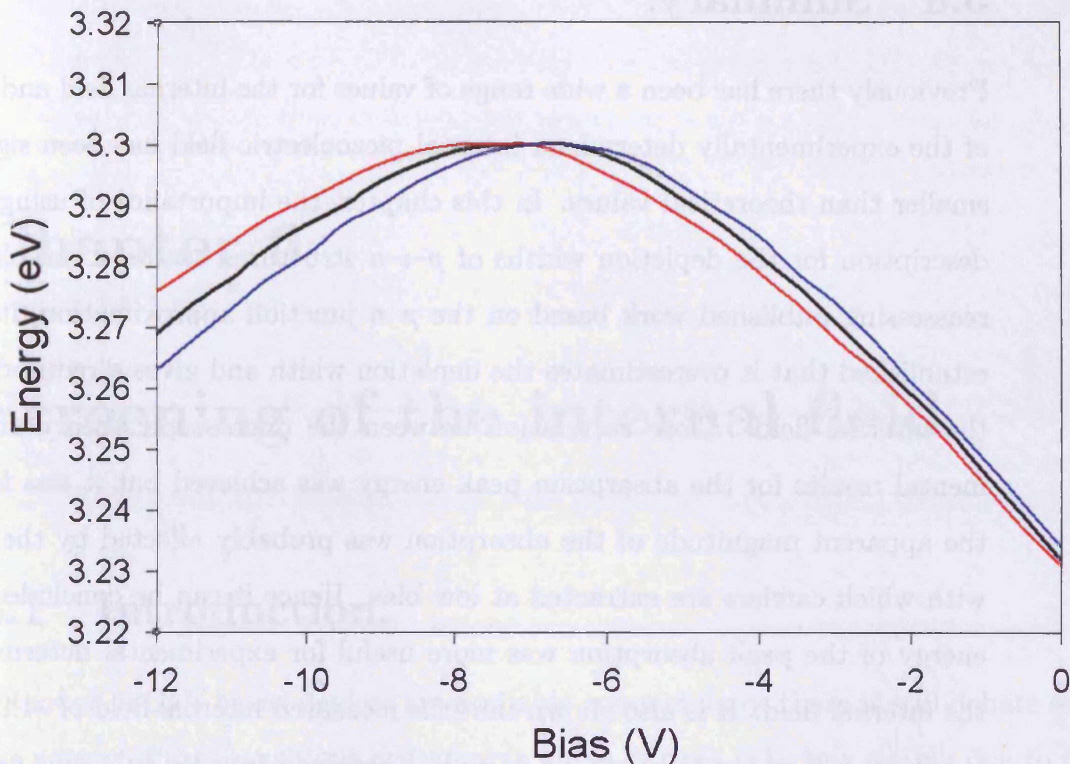

Figure 5.7.4: A comparison of the fit to the experimental results (black line) and variations due to a 10% reduction (red line) and 10% increase (blue line) in the donor doping.

The relationship is almost linear within the range shown, and the change in sign of the field at –8 V, corresponds to the critical bias and the square well condition.

As the acceptor doping is much larger than the donor doping in this structure, $N_A >> N_D$, the total depletion width, d_d, is dominated by the d_n term. In Figure 5.7.4, the effects of 10% variation in the donor doping, N_D, is shown. A 10% reduction increases the depletion width and hence the flat band condition shifts to a higher value of reverse bias, likewise a 10% increase reduces the depletion width shifting the flat band condition to a smaller reverse bias. Hence from this we can establish that variations in the donor doping have a small effect on the energy shifts with reverse bias.

5.8 Summary.

Previously there has been a wide range of values for the internal field and the value of the experimentally determined internal piezoelectric field has been significantly smaller than theoretical values. In this chapter, the importance of using a correct description for the depletion widths of p–i–n structures has been established. By reassessing published work based on the p–n junction approximation, it has been established that it overestimates the depletion width and gives a reduced value for the internal field. Close correlation between the microscopic theory and experimental results for the absorption peak energy was achieved but it was found that the apparent magnitude of the absorption was probably affected by the efficiency with which carriers are extracted at low bias. Hence it can be concluded that the energy of the peak absorption was more useful for experimental determination of the internal field. It is also shown that the measured internal field of –1.9 $MVcm^{-1}$ is within 5 % of the field of –1.8 $MVcm^{-1}$ obtained from calculations using piezoelectric and elastic constants interpolated from the binaries listed in the work of Martin et al. [124].

Chapter 6

Screening of the internal field.

6.1 Introduction.

Although InGaN based devices are available commercially, there is still debate over the nature of the transitions occurring in these devices, which is mainly due to the resultant effects of the large electric field in the quantum wells [79]. As discussed in chapter 2, the internal field skews the well causing spatial separation of the electron and hole distributions, which reduces the wavefunction overlap integral, thereby reducing both the gain and the spontaneous recombination rate at a given injected carrier density [155], hence the optical properties of these structures are determined by the interactions of band–filling, bandgap renormalisation and screening of the internal field [94]. At the high injected carrier densities that lasers and LEDs operate under, the consideration of these competing processes in the analysis of data and modelling of these devices is difficult. To simplify the problem, it is assumed that the internal field is completely screened at threshold [156], hence the well can be assumed to be square and the wavefunction overlap integral is close to unity. Although work has been performed on the effect of the internal field on properties such as emission wavelength [157], little experimental work provides information on the effects of the internal field in typical laser structures at threshold. However, the relationship between gain and intrinsic current due to a partially–

screened internal field is dependent on the well width, as reported in the theoretical work of Park et al. [155] and Chow et al. [94], this differs considerably from that of square wells. Hence a knowledge of the dependence of the properties of real quantum well structures upon injected carrier density is therefore of considerable importance for the understanding and design of laser structures.

In this chapter an investigation of strained quantum well structures using the theoretical Pade model to analyse the results of time–resolved optical pumping experiments carried out at the University of Sheffield is presented. By modelling the change in the energy–integrated intensity and the energy shifts of the peak intensity with respect to time, a greater understanding of the screening of the internal field and its effects on the dipole matrix element, lifetime and gain of these structures is achieved.

In section 6.2, the experimental results obtained by Olaizola Izquierdo [64] using time–resolved photoluminescence spectroscopy are summarised. Previously the results of time–resolved experiments have been modelled using a stretched exponential function and this is discussed in section 6.3. In section 6.4 the details of a theoretical method are presented, which models the time evolution of both the energy of the peak intensity and the energy–integrated intensity due to variations in the carrier density during pumping and recombination processes. In section 6.5, comparisons between the experimental time–resolved photoluminescence and theoretical results are presented and in section 6.6 the calculations are extended to higher carrier densities. Finally in section 6.7, the results are summarised and conclusions drawn.

6.2 Photoluminescence spectroscopy.

Time–resolved photoluminescence spectroscopy is often used [4, 12, 48, 93, 139, 158, 159], to study the dynamic recombination processes in quantum wells. Photoluminescence experiments are performed by illuminating the sample with a laser or bright lamp, with a photon energy greater than that of the bandgap of the sample,

$h\nu > E_g$. The resulting photoluminescence is emitted at lower frequencies and in all directions, a fraction of the emitted light is collected with a lens and is focused onto the entrance slit of a spectrometer. Using a photomultiplier tube or a charge coupled device (CCD), the spectrum then can be recorded [12]. Time–resolved photoluminescence spectroscopy experiments are performed by exciting the sample with a very short light pulse from an ultrafast pulse laser and recording the emission spectrum as a function of time; 1 ps or better time resolution is possible with the use of a streak camera [12]. Photocarriers excited by the ultrashort pulse go through several scattering and relaxation processes before reaching thermal equilibrium. Pumping initially creates electrons in high energy states in the conduction band, they rapidly lose energy by emitting phonons, causing a cascade of transitions within the conduction band. Strong electron–phonon coupling occurs and scattering (primarily carrier–carrier scattering) events are on the time–scale of 100 fs. Interband transitions (conduction to valence band) occur on a longer timescale, hence electrons quickly relax to the bottom of the conduction band and wait a relatively long time until they recombine, hence they form thermal distributions [12]. Thus the final carrier decay dynamics (interband) occur on a much longer timescale than the initial interactions (intraband) [66] and, regardless of the pumping energy, luminescence is observed at energies close to the band gap on a ps timescale [12].

The InGaN/GaN single quantum well devices listed in table 6.2.1 were examined at room temperature by Olaizola Izquierdo at the University of Sheffield [64], using a 20 mW Ti:sapphire laser which delivered a pulse of energy 0.25 nJ and a pulse width of 130 fs. The sample was probed with light of wavelength 355 to 370 nm and maximum PL was observed at 362.5 nm, which is the same wavelength as used in the work of Onuma et al.[118]. The pump wavelength of 362.5 nm (3.42 eV) is slightly less than the bandgap of bulk GaN (3.44 eV), this can be explained by the silicon doping ($1 \times 10^{17}\text{cm}^{-3}$) of the structure as discussed in chapter 1.

As illustrated in Figure 6.2.1, the electrons and holes in the GaN barriers are captured by the InGaN quantum well. The samples were grown by MOVPE on sapphire substrates and the composition and thickness determined by studying

calibration samples with X–ray diffraction.

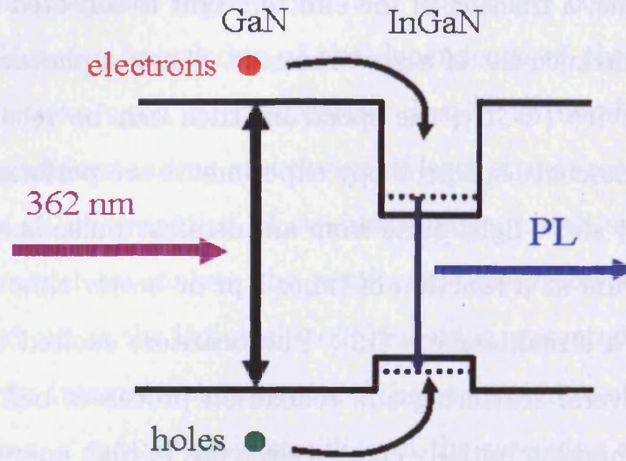

Figure 6.2.1: Optical pumping of InGaN/GaN quantum wells.

Table 6.2.1: Device structure.

Material	Width (nm)
GaN	290
$In_{0.07}Ga_{0.93}N$	3 & 4
GaN:Si	2000
GaN Buffer	1000

From examining the shifts in the energy of the peak photoluminescence with time which is presented in Figure 6.2.2 for the 3 nm and 4 nm quantum wells, it can be seen that there is an initial blue–shift in the peak photoluminescence energy followed by a red–shift, with the maximum energy occurring at a time of 400 ps. In Figure 6.2.3 the time evolution of the energy–integrated intensity is shown and it can be seen that the intensity increases and then decreases with time. The time–scale has an arbitrary zero and hence does not relate to the pumping pulse.

The energy shifts of the spectra with pumping are well documented in the published literature [4, 48, 84, 85, 94, 160] and the reduction in the intensity of the energy–integrated intensity with time can be described using a stretched exponential lineshape function and this is discussed in further detail in section 6.3.

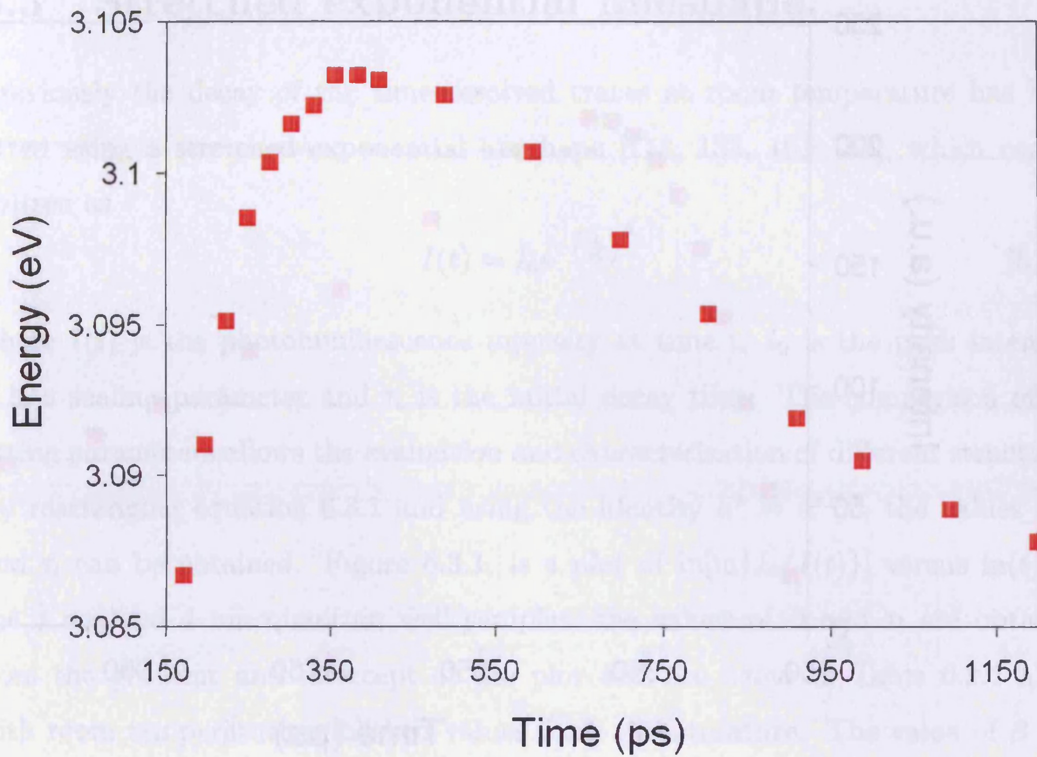

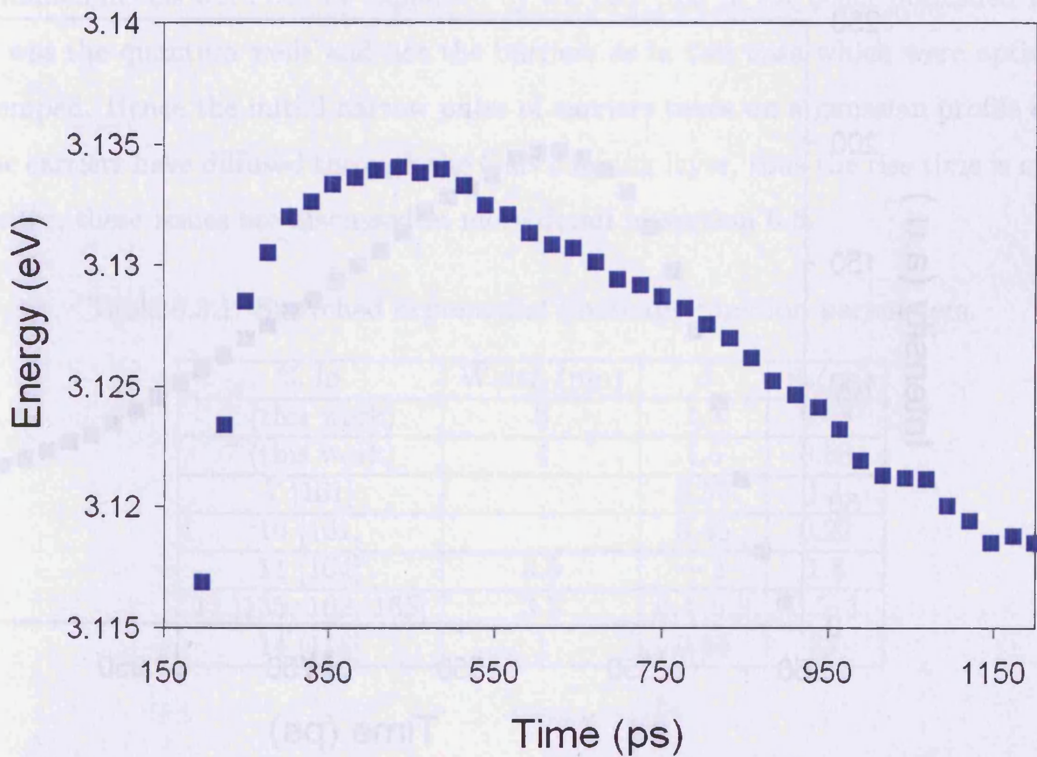

Figure 6.2.2: Experimental time evolution of the peak energy for 3 nm (top) and 4 nm (bottom) quantum well structures [64].

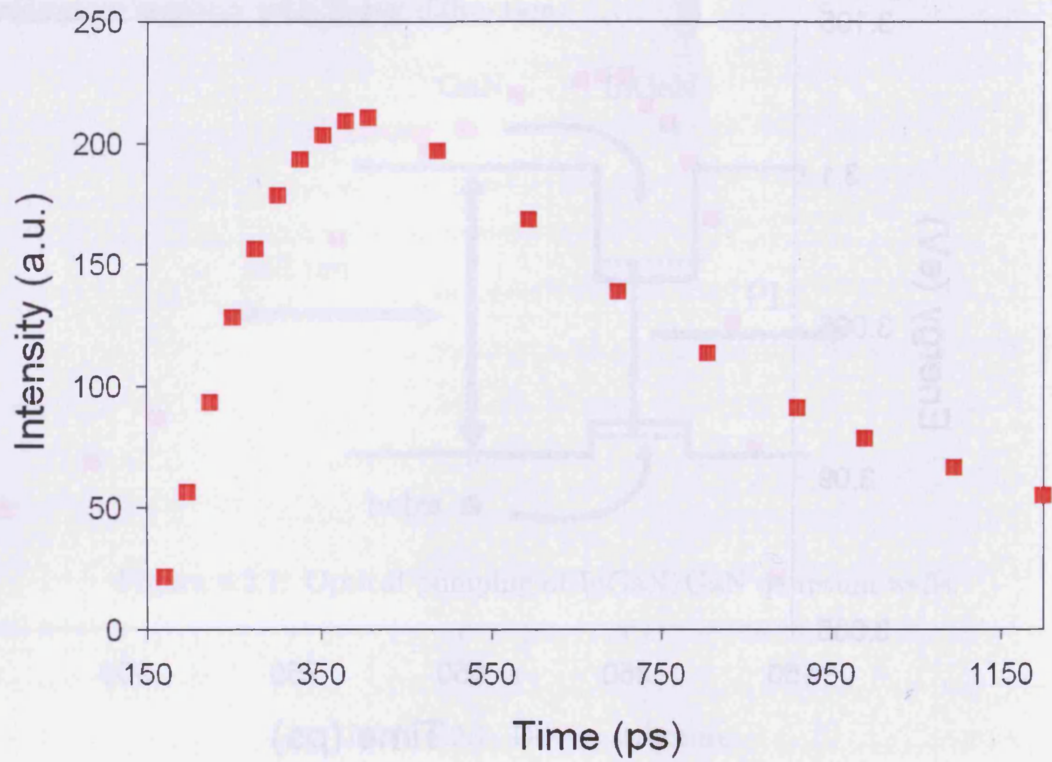

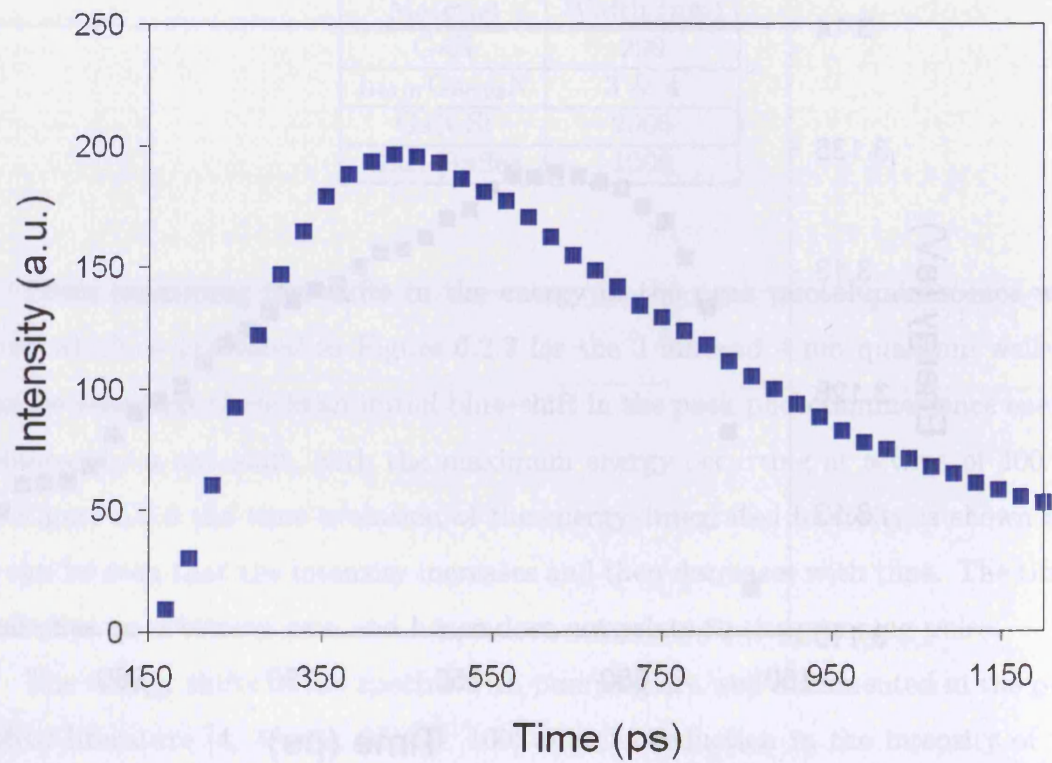

Figure 6.2.3: Experimental time evolution of the energy–integrated intensity for 3 nm (top) and 4 nm (bottom) quantum well structures [64].

6.3 Stretched exponential lineshape.

Previously the decay of the time–resolved traces at room temperature has been fitted using a stretched exponential lineshape [118, 135, 161–163], which can be written as

$$I(t) = I_0 e^{-\left(\frac{t}{\tau_i}\right)^\beta}, \tag{6.3.1}$$

where $I(t)$ is the photoluminescence intensity at time t, I_0 is the peak intensity, β is a scaling parameter and τ_i is the initial decay time. The comparison of the fitting parameters allows the evaluation and characterisation of different structures. By rearranging equation 6.3.1 and using the identity $a^x = e^{x \ln a}$, the values of β and τ_i can be obtained. Figure 6.3.1, is a plot of $\ln[\ln\{I_0/I(t)\}]$ versus $\ln(t)$ for the 3 nm and 4 nm quantum well samples, the values of β and τ_i are obtained from the gradient and intercept of the plot and are listed in Table 6.3.1 along with room temperature published values from the literature. The value of $\beta > 1$ obtained in this work can be explained by the fact that in the other published work it was the quantum wells and not the barriers as in this case which were optically pumped. Hence the initial narrow pulse of carriers takes on a gaussian profile once the carriers have diffused through the GaN capping layer, thus the rise time is much longer, these issues are discussed in more detail in section 6.5.

Table 6.3.1: Stretched exponential lineshape function parameters.

% In	Width (nm)	β	τ_i (ns)
7 (this work)	3	1.3	0.58
7 (this work)	4	1.5	0.58
7 [161]		0.55	1.1
10 [161]		0.45	0.22
11 [164]	3.5	~ 1	1.8
11 [135, 162, 165]	3.5	0.4–0.8	0.5–3
14 [118]	1	0.85	37

The fit between the experimental results and the stretched exponential lineshape given by equation 6.3.1 for the intensity decay can be seen in Figure 6.3.2. The

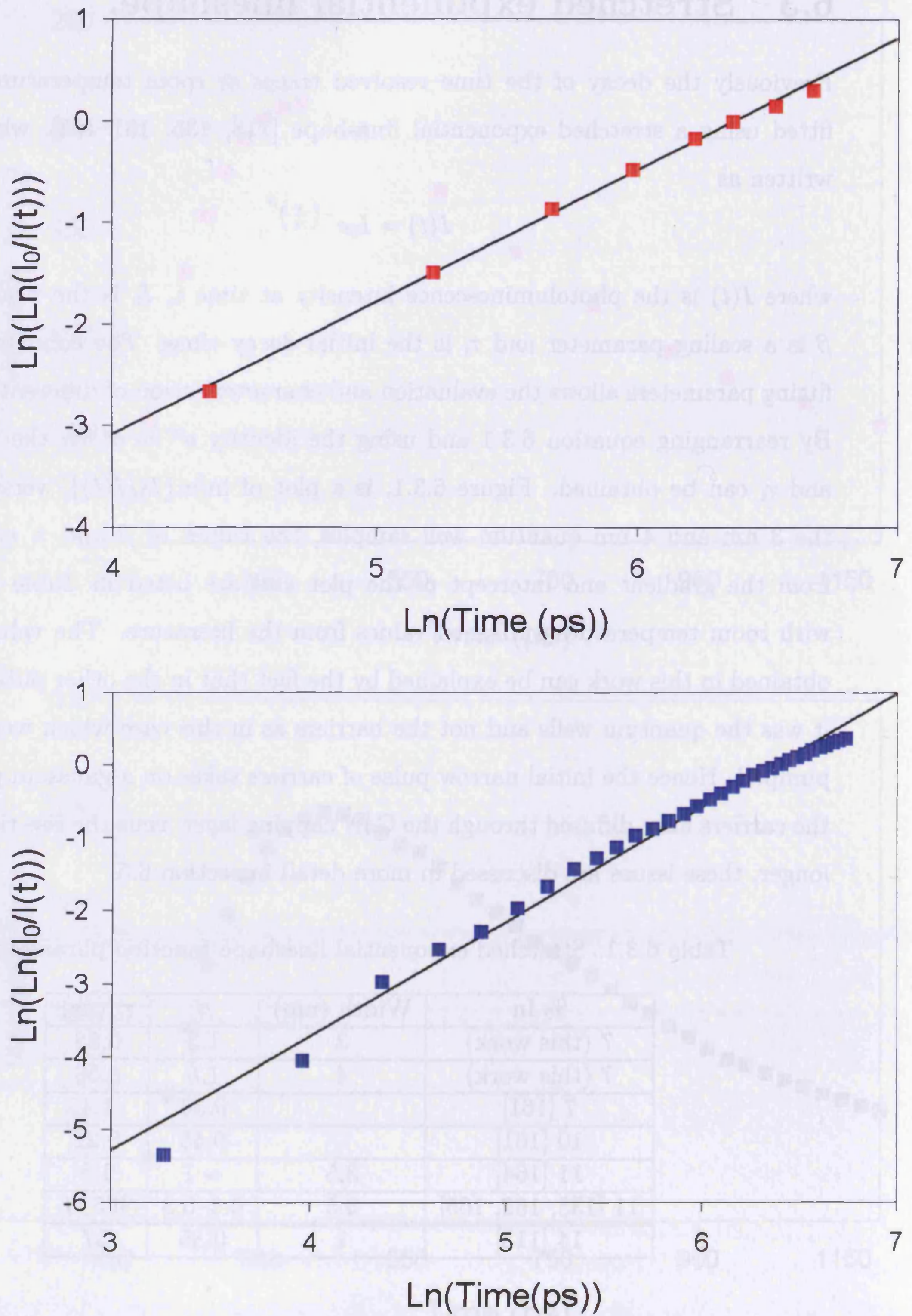

Figure 6.3.1: Fitting the intensity decay of the 3 nm (top) and 4 nm (bottom) quantum wells using the stretched exponential lineshape function [64].

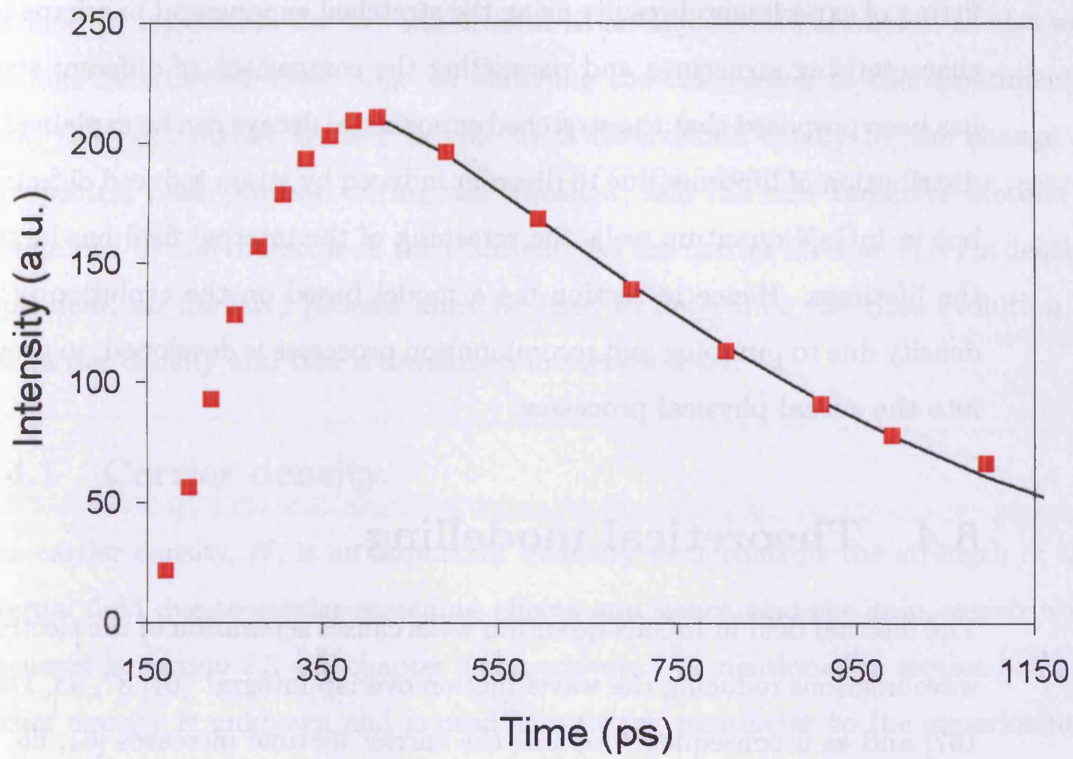

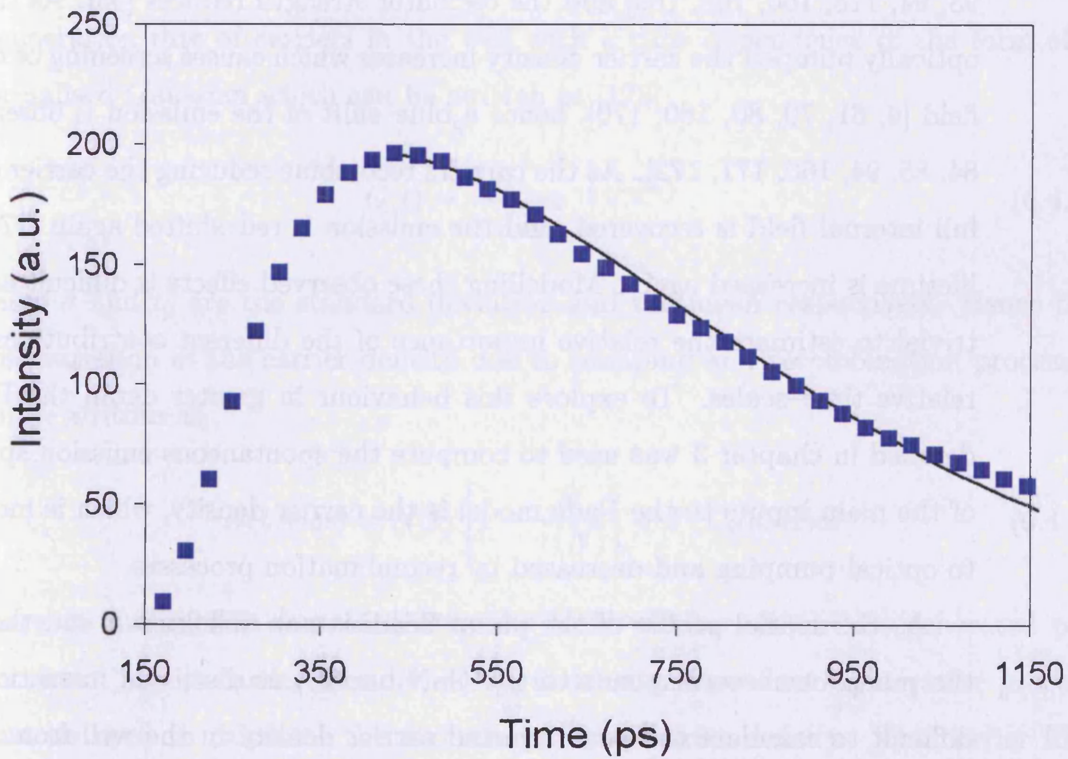

Figure 6.3.2: Comparison of the experimental results [64] and the stretched line-shape function for the intensity decay of the 3 nm (top) and 4 nm (bottom) quantum wells.

fitting of experimental results using the stretched exponential lineshape is useful for characterising structures and permitting the comparison of different structures. It has been proposed that the stretched exponential decays can be explained by a broad distribution of lifetimes due to disorder induced by strain induced defects [118, 162], but in InGaN quantum wells the screening of the internal field has large effects on the lifetimes. Hence in section 6.4 a model based on the evolution of the carrier density due to pumping and recombination processes is developed, to provide insight into the actual physical processes.

6.4 Theoretical modelling.

The internal field in InGaN quantum wells causes separation of the electron and hole wavefunctions reducing the wavefunction overlap integral [61, 87, 93, 118, 131, 166, 167] and as a consequence of this the carrier lifetime increases [61, 66, 70, 73, 85, 93, 94, 118, 160, 168, 169] and the oscillator strength reduces [93]. As the device is optically pumped the carrier density increases which causes screening of the internal field [4, 61, 70, 80, 160, 170], hence a blue–shift of the emission is observed [4, 48, 84, 85, 94, 160, 171, 172]. As the carriers recombine reducing the carrier density the full internal field is recovered, and the emission is red–shifted again [172], and the lifetime is increased again. Modelling these observed effects is difficult as it is non–trivial to estimate the relative importance of the different contributions and their relative time–scales. To explore this behaviour in greater detail the Pade model detailed in chapter 3 was used to compute the spontaneous emission spectra. One of the main inputs to the Pade model is the carrier density, which is increased due to optical pumping and decreased by recombination processes.

As the spatial profile of the pump beam is not well–known and the energy of the pump beam corresponds to the GaN barrier, as discussed in section 6.2, it is difficult to calculate the peak injected carrier density in the well from the optical pulse characteristics with any certainty since this is determined by processes of diffusion in the barrier and capture into the well. Consequently the number of

carriers, N, injected in the well was treated as an adjustable parameter, as also was the non–radiative lifetime, τ_{NR}. In matching the calculation to the experimental data, the peak carrier density for the fit is determined chiefly by the change in the spectral peak position during the transient, and the non–radiative lifetime is determined by the timescale of the transient. As the carrier lifetime $\tau(N)$ is density dependent, an iterative process must be used to determine the time evolution of the carrier density and this is developed in section 6.4.1.

6.4.1 Carrier density.

The carrier density, N, is an important quantity as it controls the strength of the internal field due to carrier screening effects and hence also the gain, which were discussed in section 2.5 and chapter 3 respectively. As mentioned in section 6.4, the carrier density is unknown and is used as a fitting parameter to the experimental results. It is assumed that the optical pumping discussed in section 6.2, causes a generation rate of carriers in the well with a time dependence of the form of a normalised Gaussian which can be written as [173]

$$G(t) = \frac{1}{\sigma\sqrt{2\pi}} e^{-\frac{1}{2}\left(\frac{t-t_0}{\sigma}\right)^2}, \tag{6.4.1}$$

where σ and t_0 are the standard deviation and the mean respectively. Hence the time variation of the carrier density due to pumping and recombination processes can be written as

$$N(t+\delta t) = N(t)\left[1 - \frac{\delta t}{\tau(N)}\right] + P(L_w)G(t)\delta t \tag{6.4.2}$$

where δt is the time step, and P is the total number of carriers generated per unit area. As the carrier lifetime, $\tau(N)$, is density dependent an iterative process must be used to calculate the evolution of the carrier density. The carrier lifetime is determined by radiative and non–radiative effects and this is discussed in section 6.4.2.

6.4.2 Lifetime.

The interband lifetime, τ, is determined by the effects of the recombination of excess carriers which can be split into the radiative, τ_R, and non–radiative, τ_{NR}, interband lifetimes and hence the overall lifetime can be written as [45, 60, 64, 160]

$$\frac{1}{\tau(N)} = \frac{1}{\tau_R(N)} + \frac{1}{\tau_{NR}}. \tag{6.4.3}$$

The radiative lifetime is calculated using

$$\tau_R(N) = \frac{N}{w_{sp}(N)}, \tag{6.4.4}$$

where the spontaneous emission rate, w_{sp}, can be written as

$$w_{sp}(N) = \int_0^{\infty} S(\omega, N)\mathrm{d}\omega, \tag{6.4.5}$$

which is the integration of the spontaneous emission, $S(\omega, N)$, over the whole energy range with contributions from all the bands [94]. It was found that the spontaneous emission was dominated by contributions from the ground and first transitions, in the ratio of 3:1. The issues concerning the calculation of the spontaneous emission were discussed in section 4.8. The internal field decreases the wavefunction overlap integral of electrons and holes, this reduces the spontaneous emission and hence increases the radiative lifetime. The non–radiative lifetime, τ_{NR}, is determined by non–radiative recombination centers, i.e. non–radiative defects and threading dislocations, which are induced by the lattice mismatch induced strain [4, 118]. It is assumed that the non–radiative lifetime is constant, independent of carrier density and wavefunction overlap [160], and it is used as a fitting parameter to the experimental data shown in section 6.2. In the work of Kalliakos et al. [160], it is shown that the lifetime is dominated by radiative recombination at low temperatures and non–radiative recombination at room temperature. This is due to the carriers having a small thermal energy, $k_B T$, at low temperature and hence they

have insufficient energy to find the defects in the lattice.

The internal radiative quantum efficiency can be written as the ratio of the rate of radiative recombination to the total recombination rate [12, 60]

$$\eta = \frac{R_R}{R_R + R_{NR}}, \tag{6.4.6}$$

this can be rewritten in terms of the radiative and non–radiative lifetimes as [45]

$$\begin{aligned} \eta &= \frac{1/\tau_R}{1/\tau_R + 1/\tau_{NR}} \\ &= \frac{1}{1 + \tau_R/\tau_{NR}}. \end{aligned} \tag{6.4.7}$$

As the internal field decreases the wavefunction overlap integral of electrons and holes, the radiative lifetimes are longer in strained structures and hence the internal field results in structures with a lower recombination efficiency [86].

6.5 Time–resolved results.

The theoretical method detailed in section 6.4, calculates the carrier density at each point in time due to pumping and recombination processes, which was used as an input in the Pade model detailed in chapter 3, allowing the spontaneous emission spectra to be calculated. As the spontaneous emission rate determines the radiative lifetime, given by equation 6.4.4, the radiative lifetime is density dependent. Hence, an iterative process was used to obtain the new carrier density at each point in time. The values of pump, P, non–radiative lifetime, τ_{nr}, mean, t_0 and standard deviation, σ, were used as adjustable parameters to allow fitting of the energy shift of the peak intensity and the energy–integrated intensity. The pump parameter was used to obtain the correct blue–shift in energy of the peak intensity and the non–radiative lifetime was used to match the red–shift. The mean and standard deviation control the shape and position of the Gaussian given by equation 6.4.1. As the carriers are generated in the GaN capping layer which is 290 nm thick, the rise time (shown in

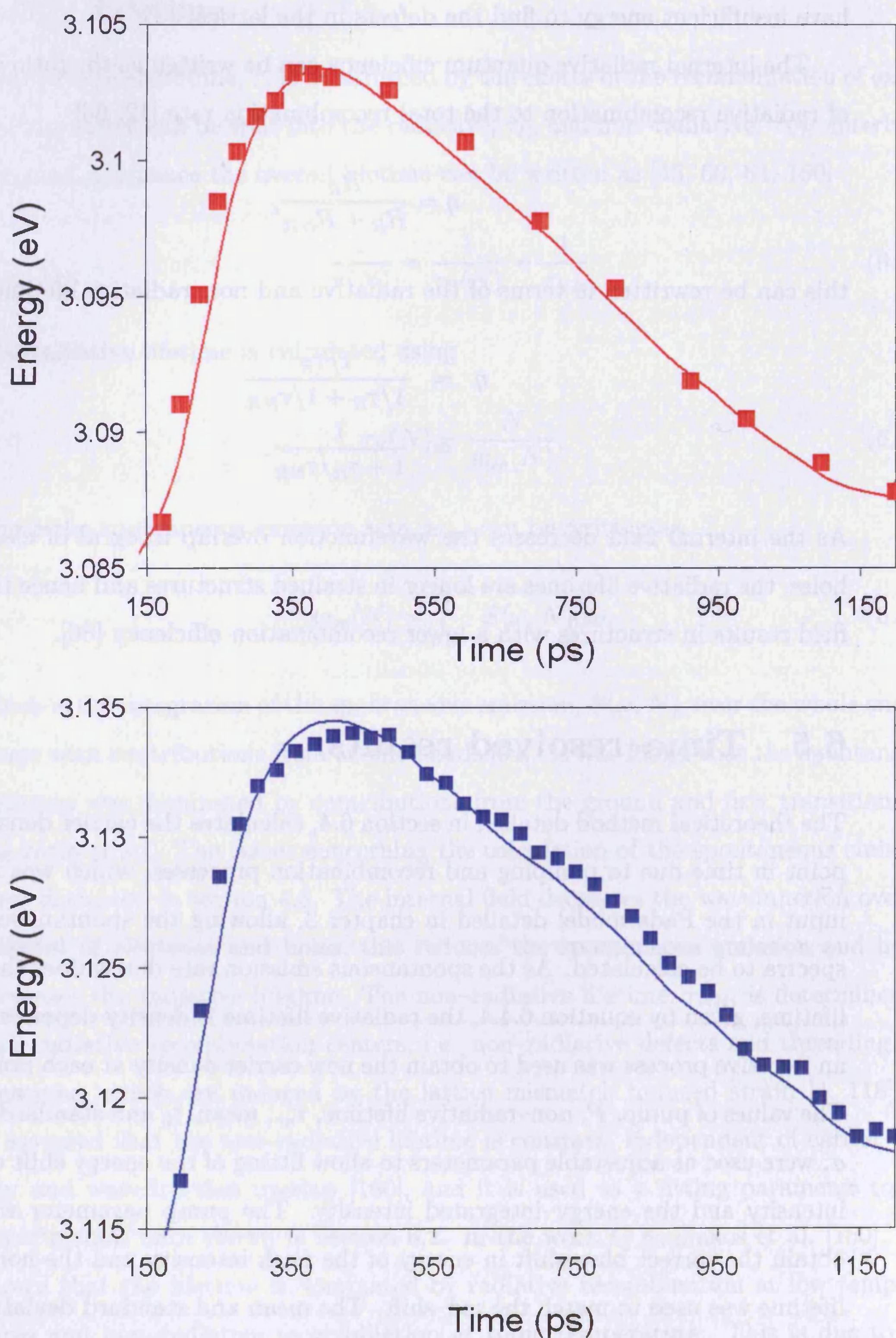

Figure 6.5.1: The experimental [64] (points) and theoretical (line) time evolution of the energy of the peak intensity for 3 nm (top) and 4 nm (bottom) quantum well structures.

Figure 6.5.1) is long of the order of 200 ps, this compares to similar work performed by Olaizola Izquierdo [64] where direct pumping of the quantum well resulted in rise times of 2 ps. This is because initially the incident laser beam whether pumping the barriers or the quantum well results in a delta profile of carriers, but in the case of barrier pumping once the carriers have diffused across the GaN layer the pulse has dispersed and becomes gaussian like. Using the value of absorption coefficient of 1×10^7 m^{-1} [174, 175], it can be calculated approximately 10 % of the carriers absorbed by the GaN capping layer are actually captured by the well. Hence the rise time which has been modelled here using a Gaussian lineshape is a convolution of the laser pulse width, diffusion processes in the GaN capping layer and capture by the quantum well. The time evolution of the energy of the peak intensity of the 3 nm and 4 nm quantum wells is shown in Figure 6.5.1, using the parameters listed in table 6.5.1. These results were obtained using an iterative procedure, at each point in time the spontaneous emission spectrum and rate were calculated, from this the radiative lifetime was obtained which was combined with the constant non–radiative lifetime to obtain the overall lifetime. Hence the new carrier density could be calculated by taking into account the changes due to pumping and recombination, this was used to calculate the spontaneous emission spectrum at the next time step. The close correlation between the experimental work performed by Olaizola Izquierdo [64] and fitted theoretical results can be seen. The experimental results for the 3 nm and 4 nm structures were fitted using a Gaussian with the same shape and temporal position, and similar values of the non–radiative lifetime but the 3 nm structure was pumped to a much higher carrier density than the 4 nm. The difference in pumping rate required to fit the data for the two samples may arise from differences in the spot size, sample reflectivity or layer thickness resulting in different internal carrier generation and collection rate into the well.

In addition to accurately modelling the energy shift, the time evolution of intensity also shows the same trend for both the 3 nm and 4 nm quantum wells, as shown in Figure 6.5.2.

Having modelled the time evolution of the energy shift in figure 6.5.1 (top) we

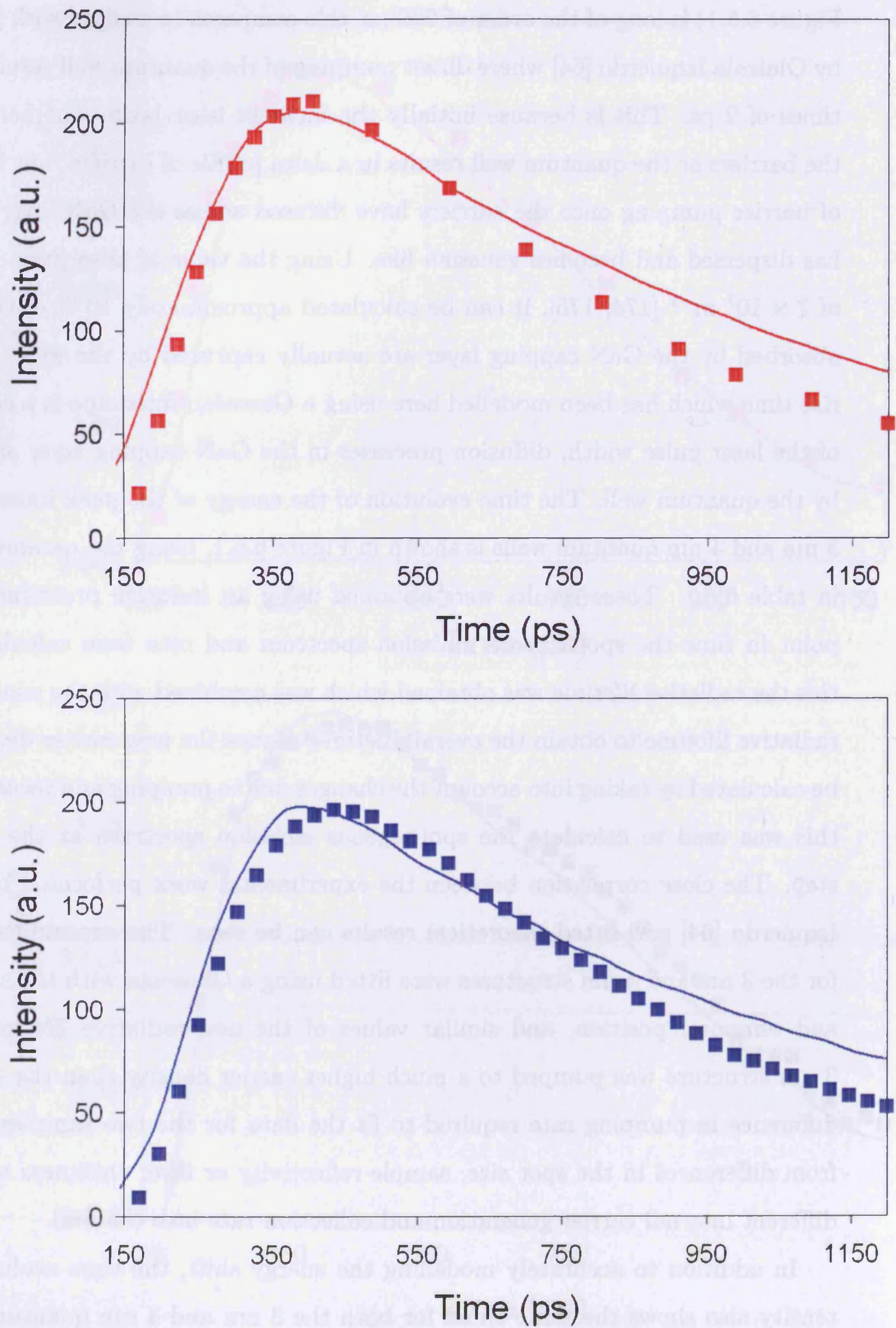

Figure 6.5.2: The experimental [64] (points) and theoretical (line) time evolution of the energy–integrated intensity for 3 nm (top) and 4 nm (bottom) quantum well structures.

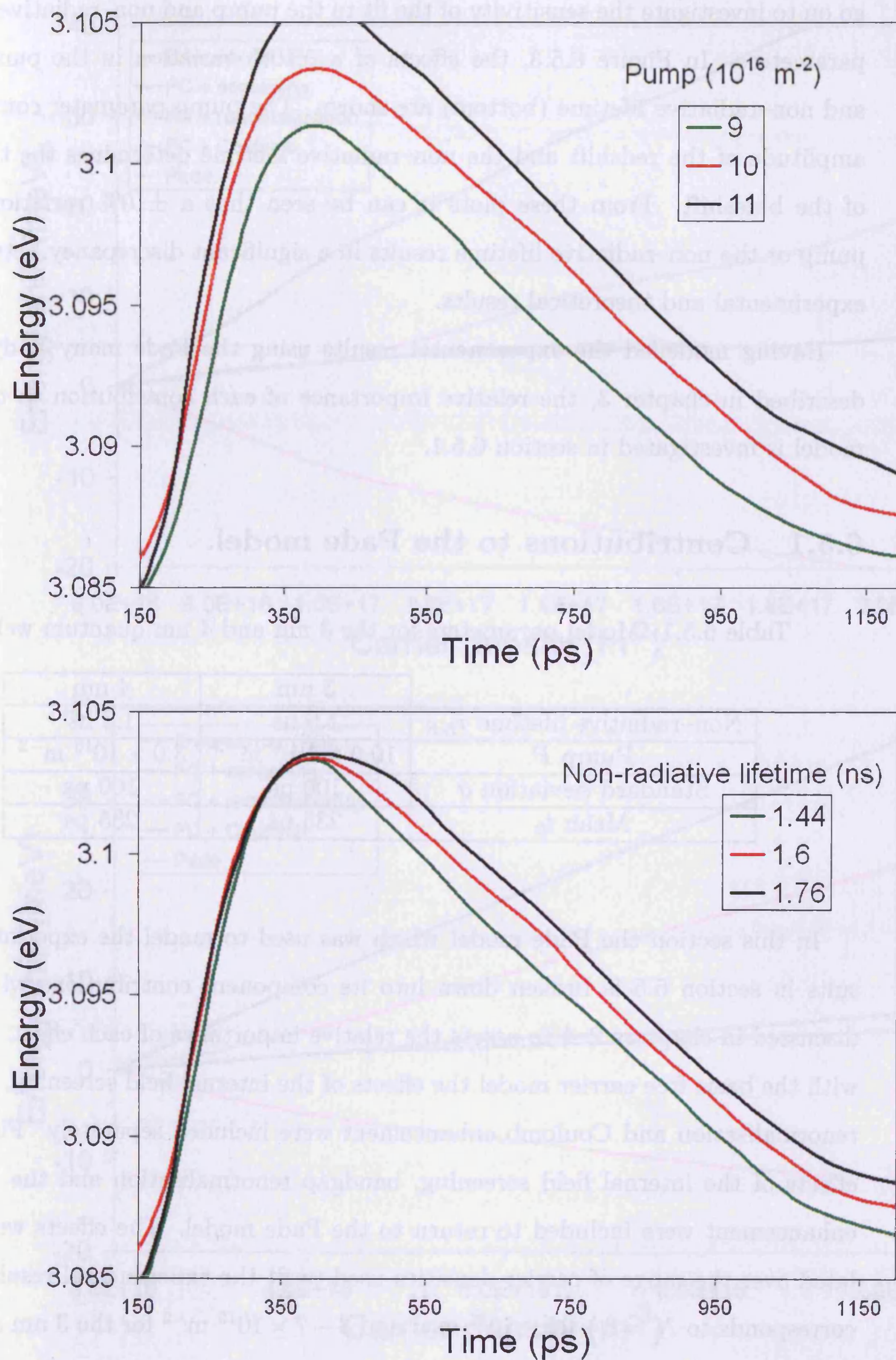

Figure 6.5.3: The sensitivity of the theoretical fit to the experimental energy of the peak intensity for the pump (top) and non–radiative lifetime (bottom) parameters for the 3 nm quantum well structure.

go on to investigate the sensitivity of the fit to the pump and non–radiative lifetime parameters. In Figure 6.5.3, the effects of a $\pm 10\%$ variation in the pump (top) and non–radiative lifetime (bottom) are shown. The pump parameter controls the amplitude of the redshift and the non–radiative lifetime determines the timescale of the blueshift. From these plots it can be seen that a $\pm 10\%$ variation in the pump or the non–radiative lifetime results in a significant discrepancy between the experimental and theoretical results.

Having modelled the experimental results using the Pade many–body theory described in chapter 3, the relative importance of each contribution to the Pade model is investigated in section 6.5.1.

6.5.1 Contributions to the Pade model.

Table 6.5.1: Model parameters for the 3 nm and 4 nm quantum wells.

	3 nm	4 nm
Non–radiative lifetime τ_{NR}	1.6 ns	1.8 ns
Pump P	10.0×10^{16} m^{-2}	3.0×10^{16} m^{-2}
Standard deviation σ	100 ps	100 ps
Mean t_0	235 ps	235 ps

In this section the Pade model which was used to model the experimental results in section 6.5 is broken down into its component contributions which were discussed in chapters 2–4 to assess the relative importance of each effect. Starting with the basic free carrier model the effects of the internal field screening, bandgap renormalisation and Coulomb enhancement were included separately. Finally the effects of the internal field screening, bandgap renormalisation and the Coulomb enhancement were included to return to the Pade model. The effects were calculated over the range of carrier densities used to fit the experimental results, which corresponds to $N = 6 - 20 \times 10^{16}$ m^{-2} and $3 - 7 \times 10^{16}$ m^{-2} for the 3 nm and 4 nm quantum well structures, respectively.

As shown Figure 6.5.4 and summarised in Table 6.5.2, the free carrier model

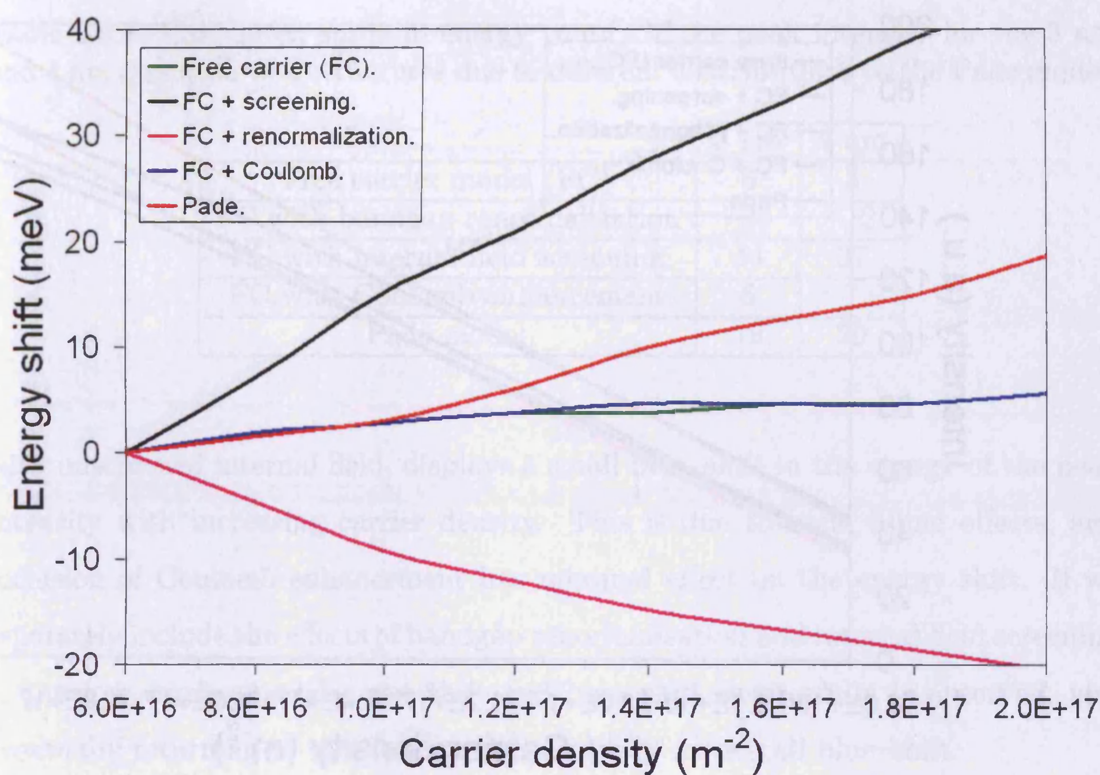

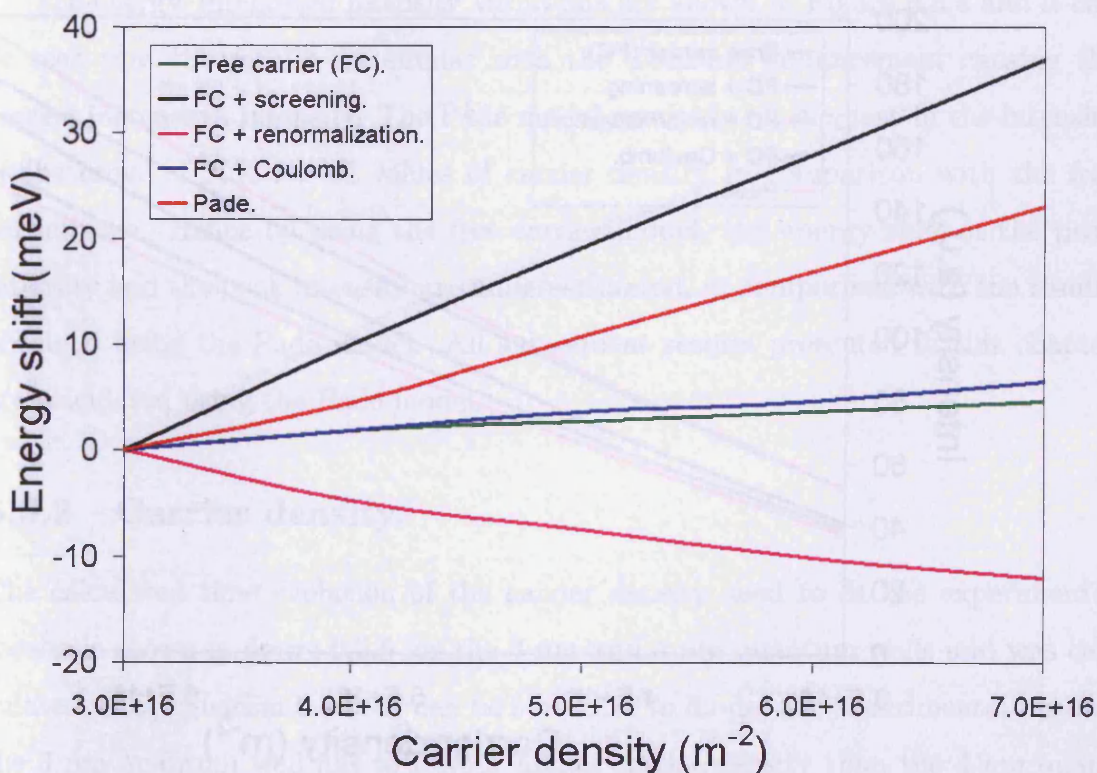

Figure 6.5.4: Energy shift of the peak intensity with carrier density due to contributions to the Pade model for the 3 nm (top) and 4 nm (bottom) quantum well structures.

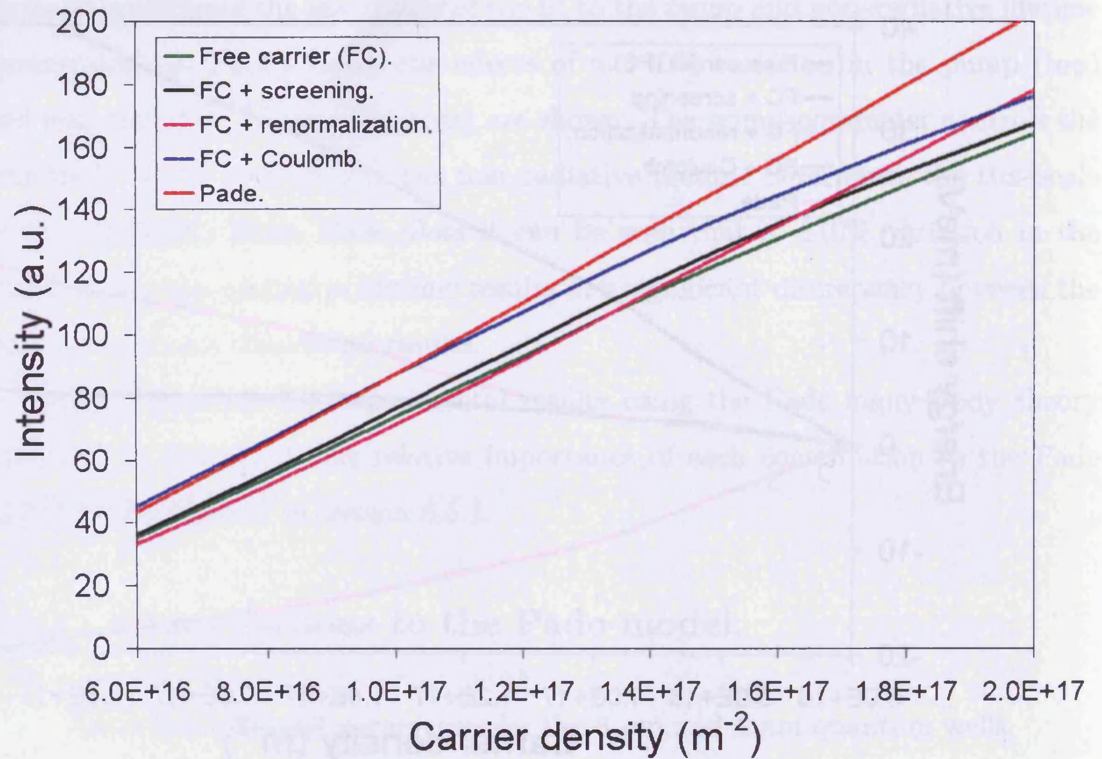

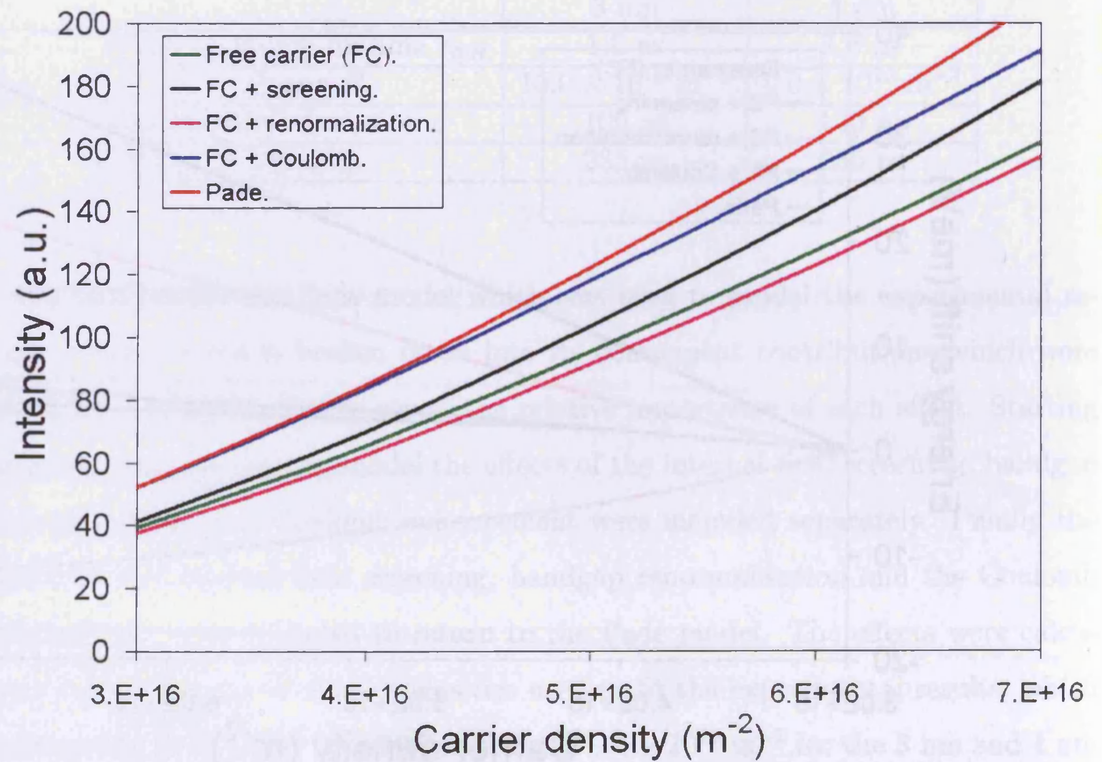

Figure 6.5.5: Variation of the energy–integrated intensity with carrier density due to contributions to the Pade model for the 3 nm (top) and 4 nm (bottom) quantum well structures.

Table 6.5.2: Calculated shifts in energy (meV) of the peak intensity for the 3 nm and 4 nm quantum well structures due to different contributions to the Pade model.

	3 nm	4 nm
Free carrier model (FC)	6	5
FC with bandgap renormalisation	–20	–12
FC with internal field screening	44	37
FC with Coulomb enhancement	6	7
Pade model	18	20

with unscreened internal field, displays a small blue–shift in the energy of the peak intensity with increasing carrier density. This is due to band filling effects, and inclusion of Coulomb enhancement has minimal effect on the energy shift. If we separately include the effects of bandgap renormalisation and internal field screening in the free carrier model a red–shift and blue–shift respectfully is observed, and eventually returning to the Pade model results in an overall blue–shift.

The energy–integrated intensity variations are shown in Figure 6.5.5 and it can be seen that the results are similar with the Coulomb enhancement causing the biggest increase in intensity. The Pade model results in an increase in the intensity of the order of 20% for all values of carrier density in comparison with the free carrier case. Hence by using the free carrier model, the energy shift of the peak intensity and the peak intensity are underestimated, in comparison with the results obtained using the Pade model. All subsequent results presented in this chapter are calculated using the Pade model.

6.5.2 Carrier density.

The calculated time evolution of the carrier density used to fit the experimental results is shown in figure 6.5.6 for the 3 nm and 4 nm quantum wells and was calculated using equation 6.4.2. It can be seen that to model the experimental results, the 3 nm quantum well has to have a higher carrier density than the 4 nm quantum well, peaking at values of $N = 2.0 \times 10^{17}$ m^{-2} and 7.0×10^{16} m^{-2} respectively.

Comparison with the experimental data in figure 6.5.1 shows that the behaviour of the emission peak follows closely the time evolution of the carrier density, with the peak blue–shifting with increasing carrier density. The difference in pumping rate required to fit the data for the two samples may arise from differences in the spot size, sample reflectivity or layer thickness resulting in different internal carrier generation and collection rate into the well.

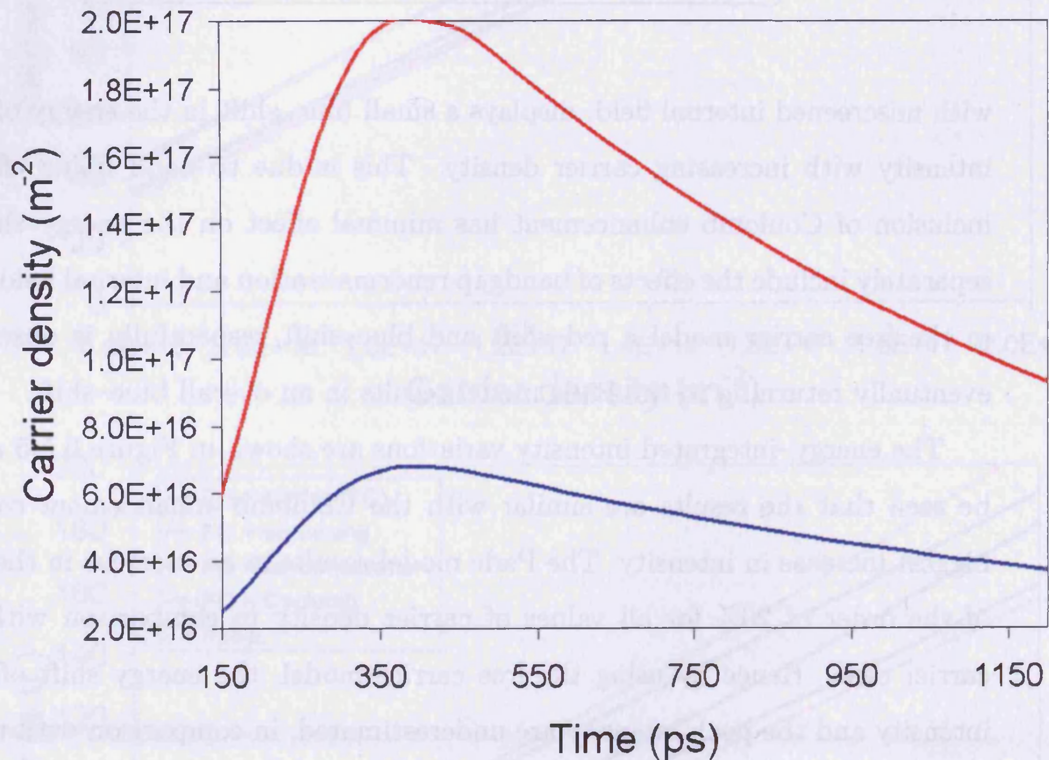

Figure 6.5.6: The modelled time evolution of the carrier density, N, for 3 nm (red) and 4 nm (blue) quantum well structures.

6.5.3 Screened internal field.

As the unscreened internal field, $E_{int}(0)$, is determined by the composition of the well, it has the same value for both the 3 nm and 4 nm quantum wells, and using equation 2.2.1 a value of $E_{int}(0) = -1.23$ MVcm^{-1} was calculated. The screened internal field, $E_{int}(N)$, given by equation 2.5.1, is shown in Figure 6.5.7 for the

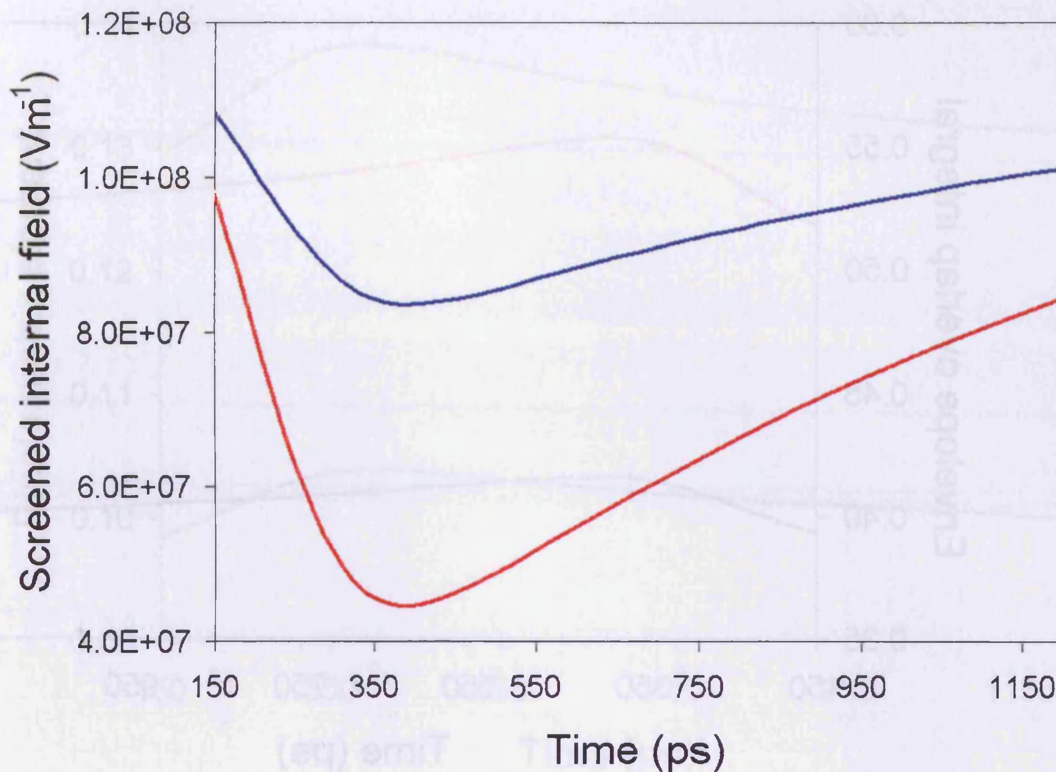

Figure 6.5.7: The modelled time evolution of the screened internal field for 3 nm (red) and 4 nm (blue) quantum well structures.

3 nm and 4 nm quantum wells, and over the range shown the internal field displays a peak reduction of 55% and 30% due to screening for the 3 nm and 4 nm quantum wells respectively.

6.5.4 Wavefunction overlap integral and dipole matrix.

As the internal field is screened, the spatial separation of the electron and hole wavefunction is reduced, hence an increase in the wavefunction overlap integral and thus the dipole matrix element is expected. As discussed in section 6.5.3 the internal field is strongly screened at the peak carrier density, hence a large variation in the wavefunction overlap integral and the dipole matrix element is expected.

The wavefunction overlap integral, is given by $\left|\int_{-\infty}^{\infty} U_e(z)U_h(z)\mathrm{d}z\right|^2$, where $U_e(z)$ and $U_h(z)$ are the ground state electron and hole envelope functions [8]. For an ideal

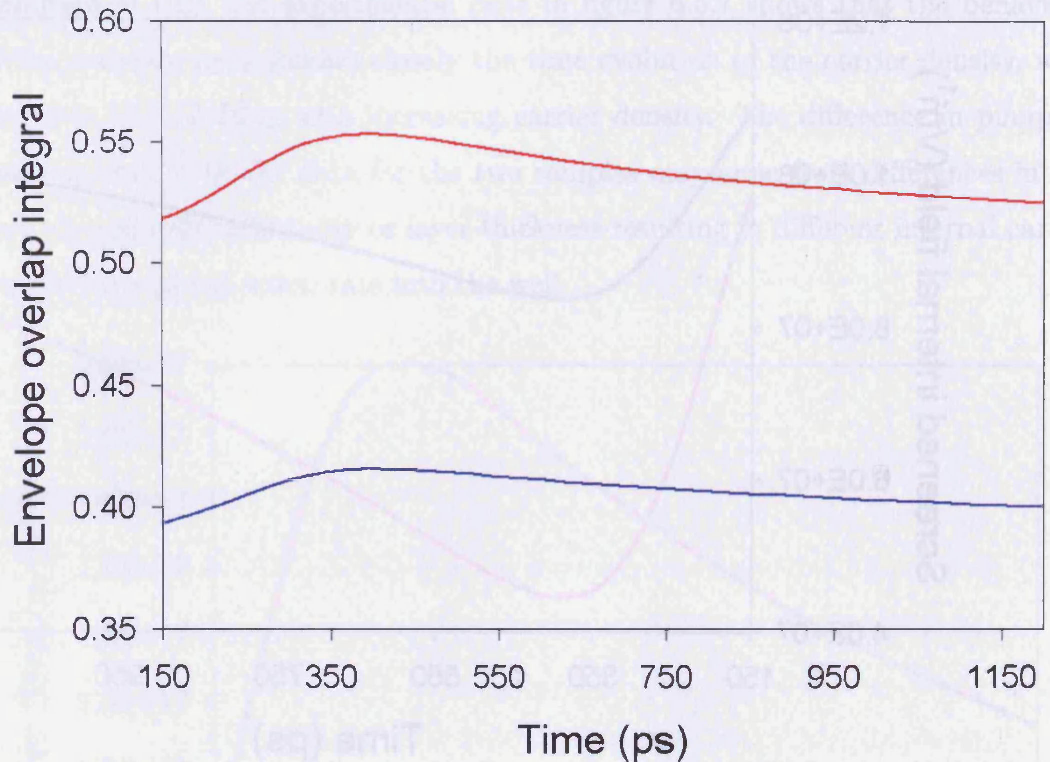

Figure 6.5.8: Modelled time evolution of the wavefunction overlap integral for the 3 nm (red) and 4 nm (blue) quantum well structures.

square well values of the wavefunction overlap integral of ~ 1 and ~ 0 are expected for allowed and forbidden transitions respectively. Due to different effective masses and barrier heights in the conduction and valence bands, the wavefunction overlap integral has values of 0.88 and 0.92 for square 3 nm and 4 nm quantum wells respectively. When the effect of the unscreened internal field is included, the parity rules no longer apply and the values drop to 0.5091 and 0.3851 respectively. In Figure 6.5.8 the time evolution of the wavefunction overlap integral is shown for the 3 nm and 4 nm quantum well structures and an increase of 15% and 5% respectively is observed.

The dipole matrix element which appears in equation 3.3.22 for gain, was investigated by looking at the change in $\left|\frac{\mu^{TE}}{\mu_{\text{Bulk}}}\right|^2$, which is the ratio of the quantum well and bulk dipole matrix elements. The dipole matrix element is proportional

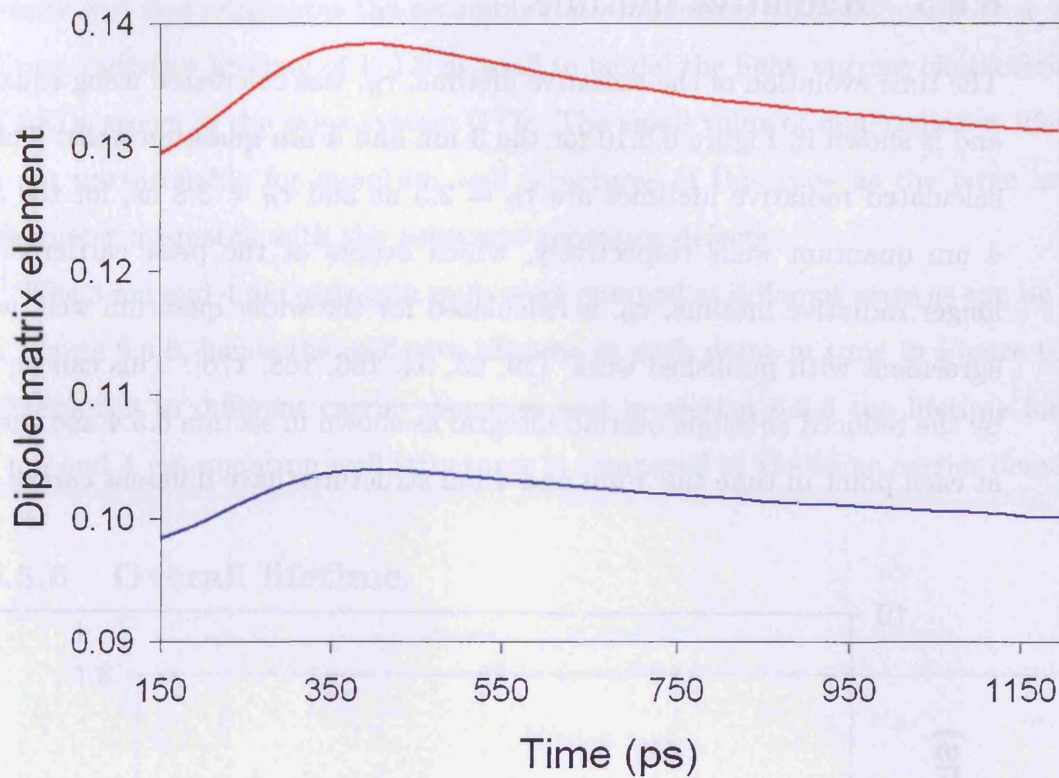

Figure 6.5.9: Modelled time evolution of the relative dipole matrix element for the 3 nm (red) and 4 nm (blue) quantum well structures.

to the wavefunction overlap integral and hence follows the same trends. Neglecting the internal field i.e. the square well case, the relative dipole matrix element has values of 0.22 and 0.23, including the unscreened internal field, $E_{int}(0)$, reduces the values to 0.1273 and 0.0963 for the 3 nm and 4 nm quantum wells respectively. In Figure 6.5.9 the time evolution of the relative dipole matrix element is shown for the 3 nm and 4 nm quantum well structures and an increase of 15% and 5% respectively is observed.

Hence even though there is a large change in the internal field due to screening the change in the wavefunction overlap integral and the relative dipole matrix element is small by comparison. The investigation of the wavefunction overlap integral and the relative dipole matrix element at higher carrier densities is covered in section 6.6.2.

6.5.5 Radiative lifetime.

The time evolution of the radiative lifetime, τ_R, was calculated using equation 6.4.4 and is shown in Figure 6.5.10 for the 3 nm and 4 nm quantum wells. The shortest calculated radiative lifetimes are τ_R = 2.5 ns and τ_R = 3.8 ns, for the 3 nm and 4 nm quantum wells respectively, which occurs at the peak carrier density. A longer radiative lifetime, τ_R, is calculated for the wider quantum well, which is in agreement with published work [79, 93, 94, 166, 168, 176]. This can be explained by the reduced envelope overlap integral as shown in section 6.5.4 and the fact that at each point in time the 3 nm and 4 nm structures have different carrier densities.

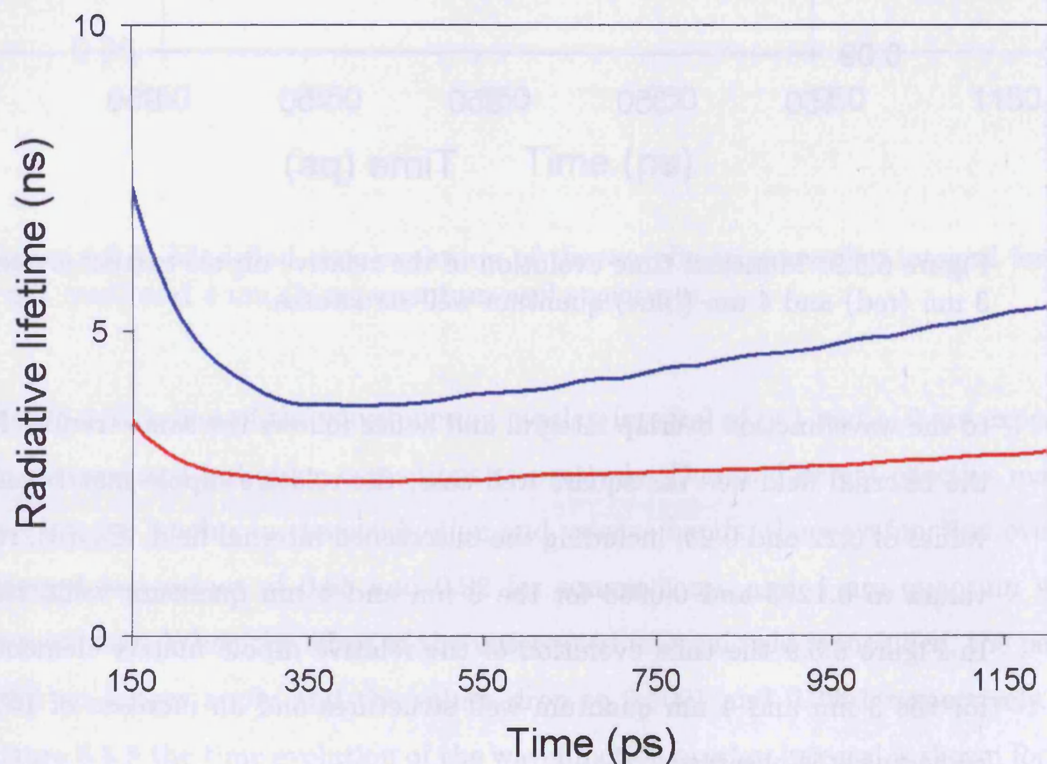

Figure 6.5.10: The modelled time evolution of the radiative lifetime, τ_R, for the 3 nm (red) and 4 nm (blue) quantum well structures.

A constant value for the non–radiative lifetime of τ_{NR} = 1.6 ns and 1.8 ns for the 3 nm and 4 nm quantum wells respectively was used to fit the experimental

results and this dominates the recombination processes. This compares to a value of non–radiative lifetime of 1–1.5 ns used to model the light–current characteristics of LEDs grown in the same system [177]. The small value of non–radiative lifetime is not unreasonable for quantum well structures of this type as the large lattice parameter mismatch with the substrate generates defects.

The 3 nm and 4 nm quantum wells were pumped at different rates as can be seen in Figure 6.5.6, hence the radiative lifetime at each point in time in Figure 6.5.10 corresponds to different carrier densities and in section 6.6.3 the lifetime for the 3 nm and 4 nm quantum well structures is compared at the same carrier densities.

6.5.6 Overall lifetime.

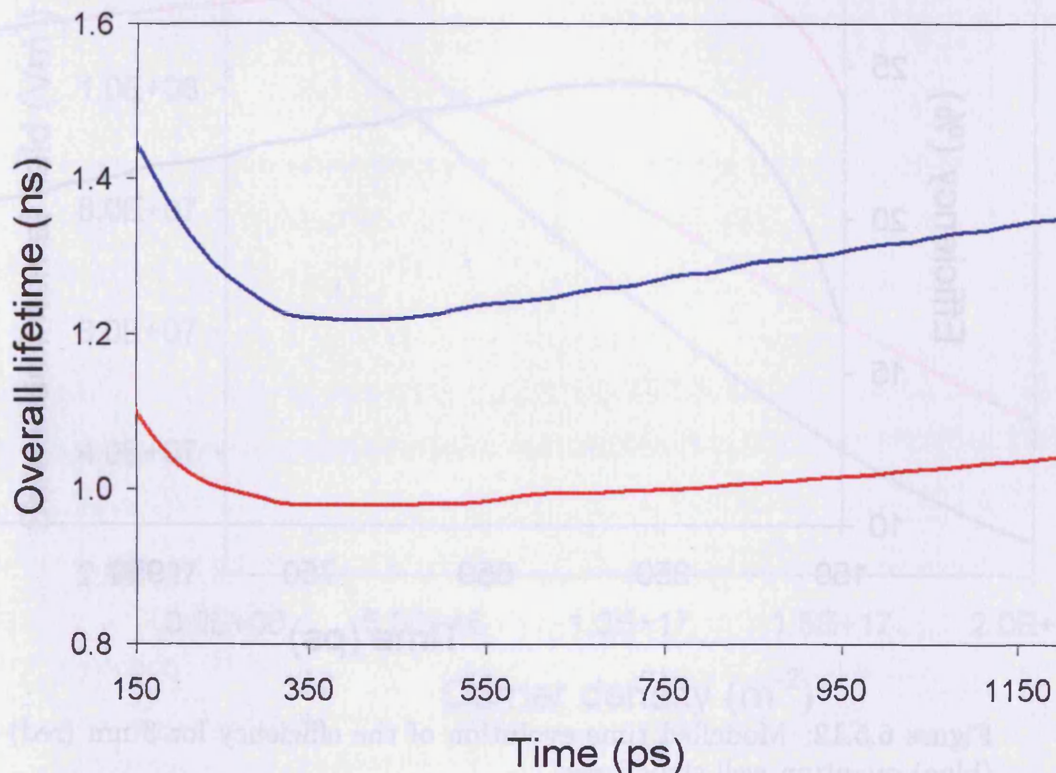

Figure 6.5.11: Modelled time evolution of the overall lifetime, τ, for 3 nm (red) and 4 nm (blue) quantum well structures.

The overall lifetime as a function of time is shown in Figure 6.5.11, this was

calculated using the values of radiative lifetime presented in Figure 6.5.10, the non–radiative lifetimes of τ_{NR} = 1.6 ns and 1.8 ns for the 3 nm and 4 nm quantum wells respectively and equation 6.4.3. The shortest lifetimes of 1.0 ns and 1.2 ns for the 3 nm and 4 nm quantum well respectfully are calculated at 400 ps which corresponds to the peak in carrier density. The variations in the overall lifetime are small as it is dominated by the non–radiative lifetime, which is assumed to be constant independent of carrier density and hence time.

6.5.7 Efficiency.

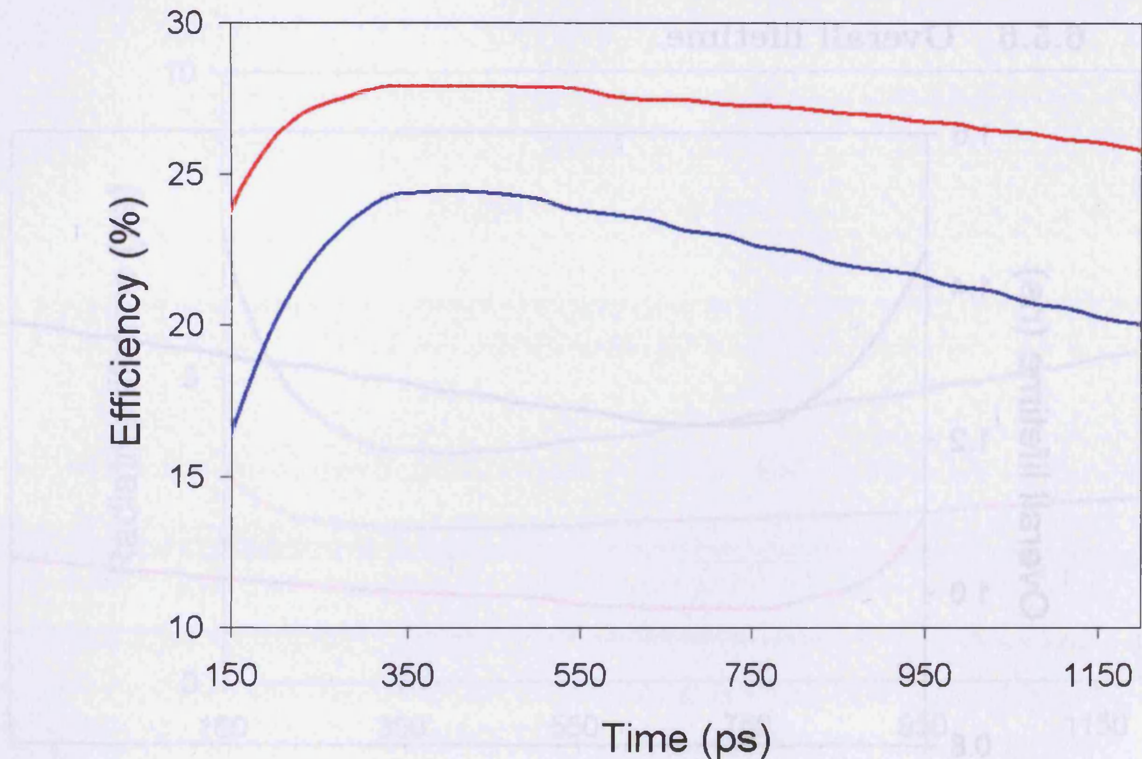

Figure 6.5.12: Modelled time evolution of the efficiency for 3 nm (red) and 4 nm (blue) quantum well structures.

As a consequence of the structures being dominated by the non–radiative lifetime as detailed in sections 6.5.5 and 6.5.6, the efficiency, η, which was discussed in section 6.4.2 is always small. The efficiency is shown in Figure 6.5.12, and peaks at

a value of 28% and 25% for the 3 nm and 4 nm quantum wells, respectively.

6.6 Extrapolation to high carrier density.

Having modelled the experimental work performed by Olaizola Izquierdo [64] and presented the time dependence of key properties such as the internal field, relative dipole matrix element, lifetime and efficiency in section 6.5, we go on to investigate these issues at higher carrier densities typical of lasing action.

6.6.1 Screened internal field.

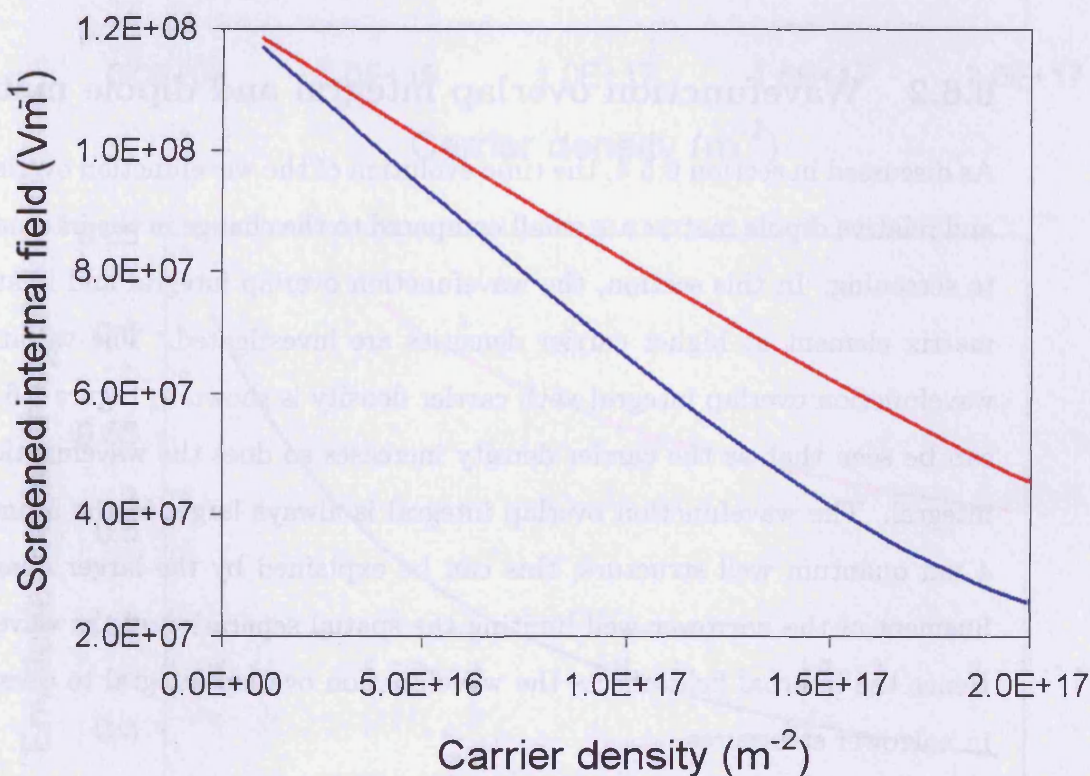

Figure 6.6.1: Variation of the screened internal field with carrier density for 3 nm (red) and 4 nm (blue) quantum well structures.

As discussed in section 6.5.3, the unscreened internal field, $E_{int}(0)$, is independent of the quantum well width if strain relaxation has not taken place, hence the

unscreened internal field has a value of $E_{int}(0) = -1.23$ MVcm^{-1} for both the 3 nm and 4 nm quantum wells. In Figure 6.6.1, which shows the screening of the internal field, $E_{int}(N)$, with carrier density, it can be seen that there is a reduction in the screened internal field with carrier density, for the 3 nm and 4 nm quantum wells. At a low carrier density of $N = 1.0 \times 10^{16}$ m^{-2}, which is the Mott density as discussed in section 4.10.3, the screened internal field in the 3 nm and 4 nm quantum wells is similar, but the 4 nm structure experiences a larger rate of change in the screening field with carrier density, hence the screened internal field at the same carrier density is always smaller in the wider well. At a reference carrier density of $N = 2.0 \times 10^{17}$ m^{-2} the internal field is reduced to 37% and 20% of the unscreened value due to screening for the 3 nm and 4 nm quantum wells, respectively.

6.6.2 Wavefunction overlap integral and dipole matrix.

As discussed in section 6.5.4, the time evolution of the wavefunction overlap integral and relative dipole matrix are small compared to the change in the internal field due to screening. In this section, the wavefunction overlap integral and relative dipole matrix element at higher carrier densities are investigated. The variation of the wavefunction overlap integral with carrier density is shown in Figure 6.6.2 (top), it can be seen that as the carrier density increases so does the wavefunction overlap integral. The wavefunction overlap integral is always larger in the 3 nm than the 4 nm quantum well structure, this can be explained by the larger quantum confinement of the narrower well limiting the spatial separation of the wavefunctions. Hence the internal field affects the wavefunction overlap integral to a lesser extent in narrower structures.

At a carrier density of $N = 2 \times 10^{17}$ m^{-2} both structures have a wavefunction overlap value of close to 0.61, but at the same carrier density there is a smaller screened internal field in the 4 nm than the 3 nm quantum well structure as seen in Figure 6.6.1. Hence the variation of the wavefunction overlap integral with screened internal field is shown in Figure 6.6.2 (bottom). The wavefunction overlap integral

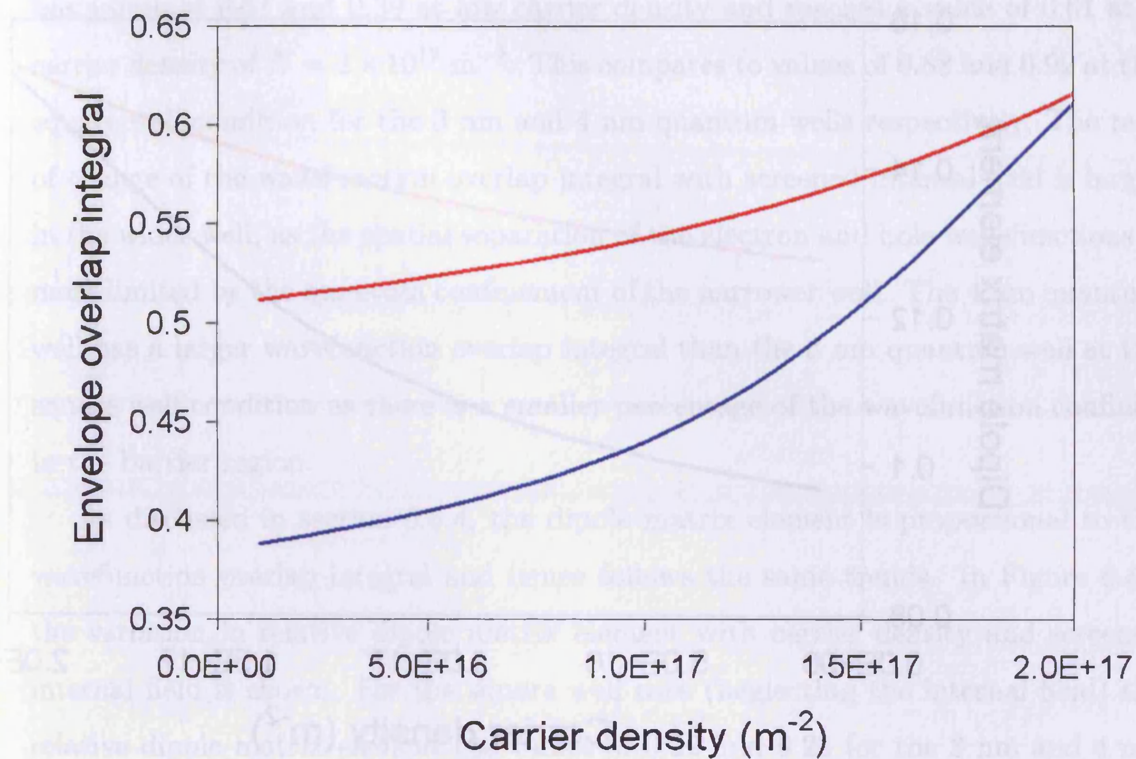

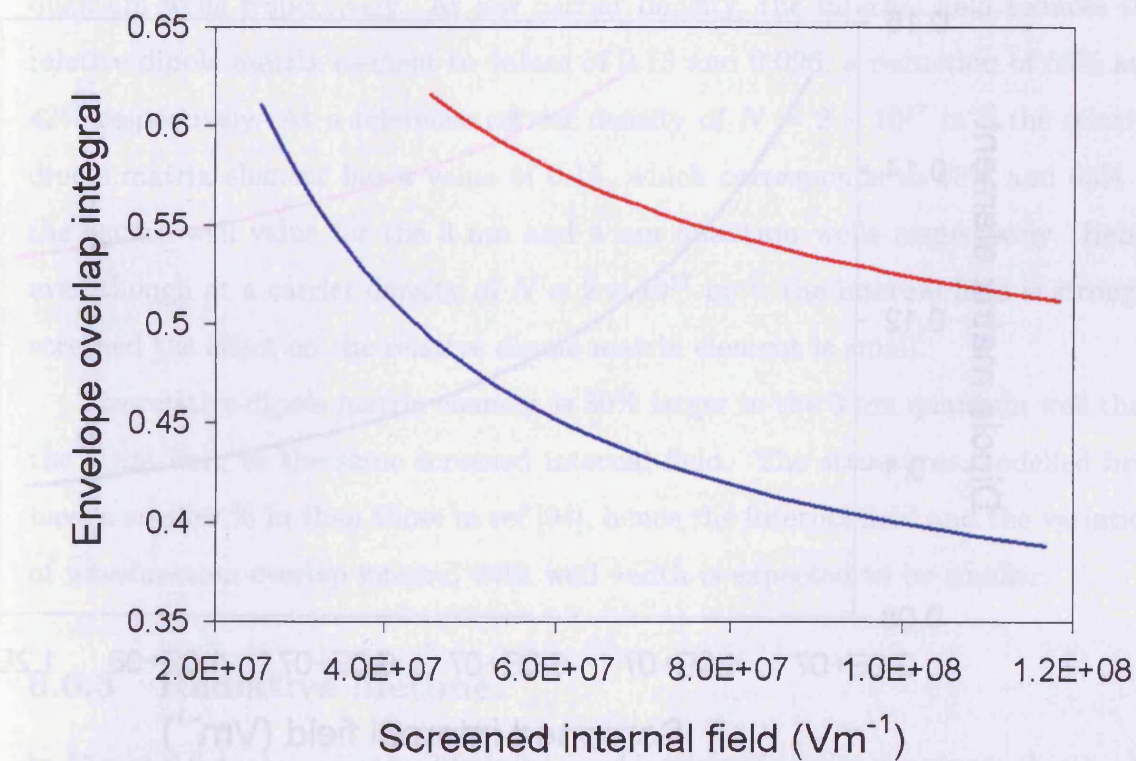

Figure 6.6.2: Variation of the wavefunction overlap integral with carrier density (top) and screened internal field (bottom) for the 3 nm (red) and 4 nm (blue) quantum well structures.

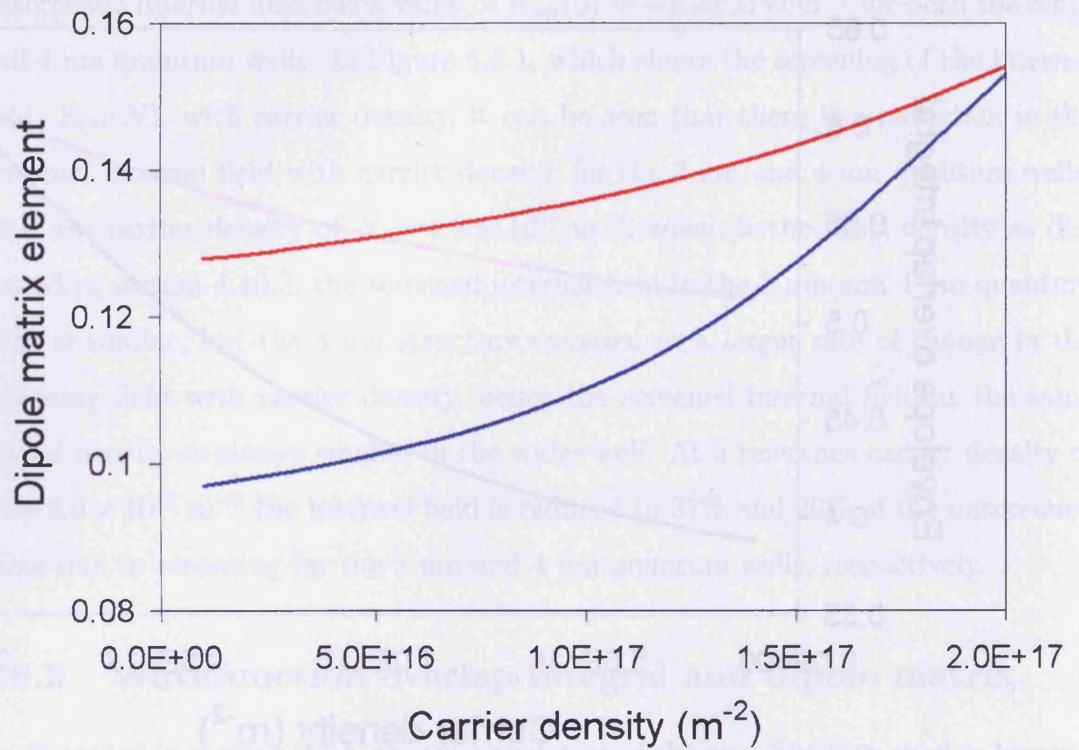

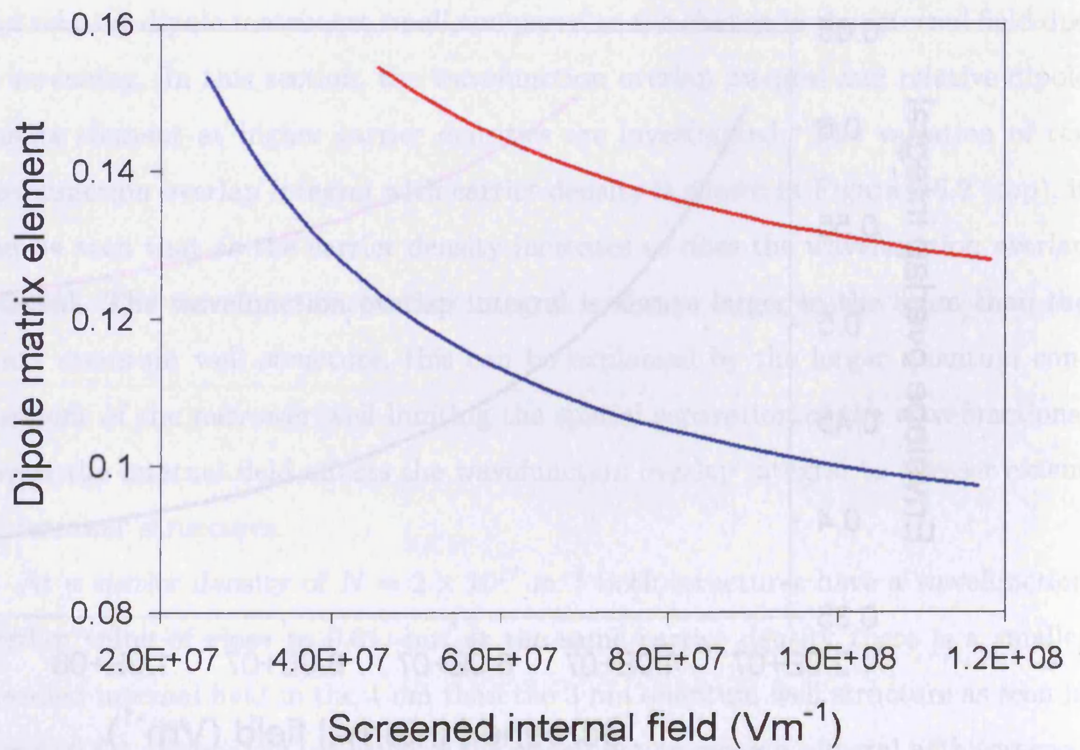

Figure 6.6.3: Variation of the relative dipole matrix element with carrier density (top) and screened internal field (bottom) for the 3 nm (red) and 4 nm (blue) quantum well structures.

has values of 0.51 and 0.39 at low carrier density and reaches a value of 0.61 at a carrier density of $N = 2 \times 10^{17}$ m^{-2}. This compares to values of 0.88 and 0.92 at the square well condition for the 3 nm and 4 nm quantum wells respectively. The rate of change of the wavefunction overlap integral with screened internal field is larger in the wider well, as the spatial separation of the electron and hole wavefunctions is more limited by the quantum confinement of the narrower well. The 4 nm quantum well has a larger wavefunction overlap integral than the 3 nm quantum well at the square well condition as there is a smaller percentage of the wavefunction confined in the barrier region.

As discussed in section 6.5.4, the dipole matrix element is proportional to the wavefunction overlap integral and hence follows the same trends. In Figure 6.6.3 the variation in relative dipole matrix element with carrier density and screened internal field is shown. For the square well case (neglecting the internal field) the relative dipole matrix element has values of 0.22 and 0.23 for the 3 nm and 4 nm quantum wells respectively. At low carrier density, the internal field reduces the relative dipole matrix element to values of 0.13 and 0.096, a reduction of 59% and 42% respectively. At a reference carrier density of $N = 2 \times 10^{17}$ m^{-2} the relative dipole matrix element has a value of 0.15, which corresponds to 68% and 65% of the square well value for the 3 nm and 4 nm quantum wells respectively. Hence even though at a carrier density of $N = 2 \times 10^{17}$ m^{-2}, the internal field is strongly screened the effect on the relative dipole matrix element is small.

The relative dipole matrix element is 30% larger in the 3 nm quantum well than the 4 nm well, at the same screened internal field. The structures modelled here have a smaller % In than those in ref [94], hence the internal field and the variation of wavefunction overlap integral with well width is expected to be smaller.

6.6.3 Radiative lifetime.

In Figure 6.6.4, the radiative lifetime as a function of carrier density is shown. At low carrier density the radiative lifetime is 20 ns and at a reference carrier density

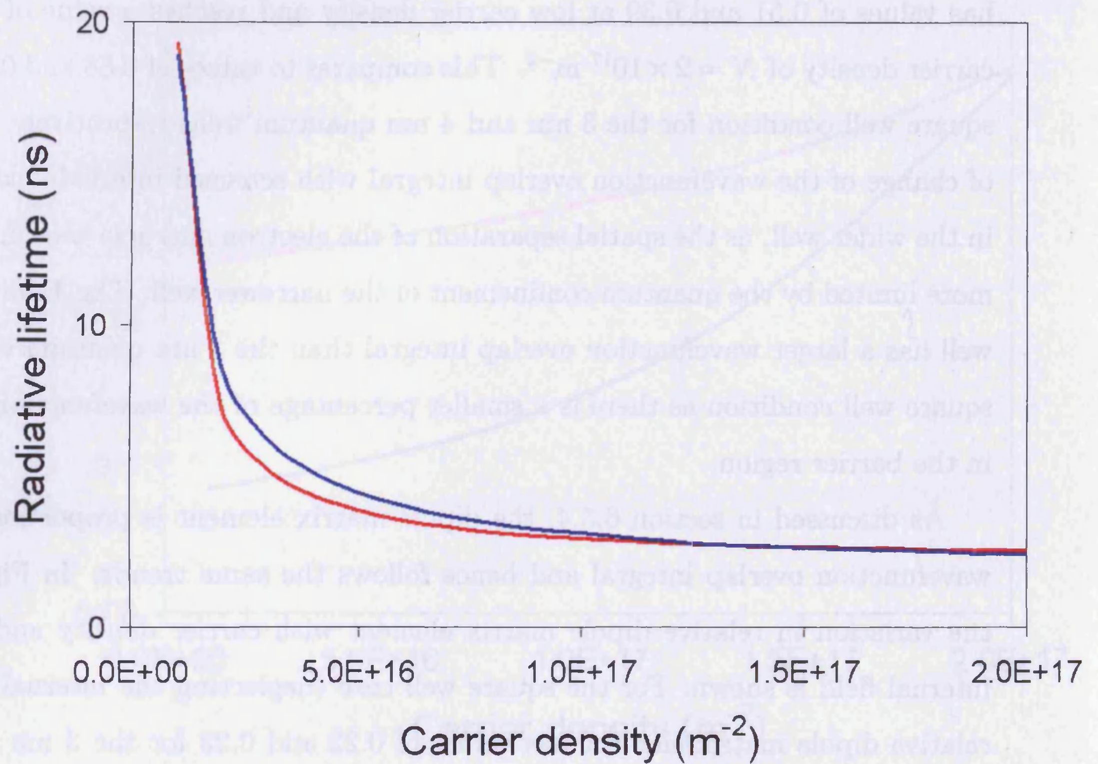

Figure 6.6.4: Radiative lifetime as a function of carrier density for the 3 nm (red) and 4 nm (blue) quantum well structures.

of $N = 2 \times 10^{17}$ m^{-2} the value is reduced to 2.5 ns. At the same carrier density the lifetime for the 4 nm well is always longer than that of the 3 nm well, which is to be expected since the dipole matrix element is less for the wider well as discussed in section 6.6.2.

6.6.4 Material gain.

From investigation of the variation of the material gain with carrier density which is shown in Figure 6.6.5 (top), it can be seen that the 3 nm and 4 nm quantum well structures have a transparency carrier density of $N = 5 \times 10^{16}$ m^{-2} and $N = 4.5 \times 10^{16}$ m^{-2} respectively, with the 3 nm quantum well showing a larger increase in material gain with carrier density, than the 4 nm quantum well. At the transparency point the internal field is screened to a value of $E_{int}(N)$=1.0 MVcm^{-1} for both

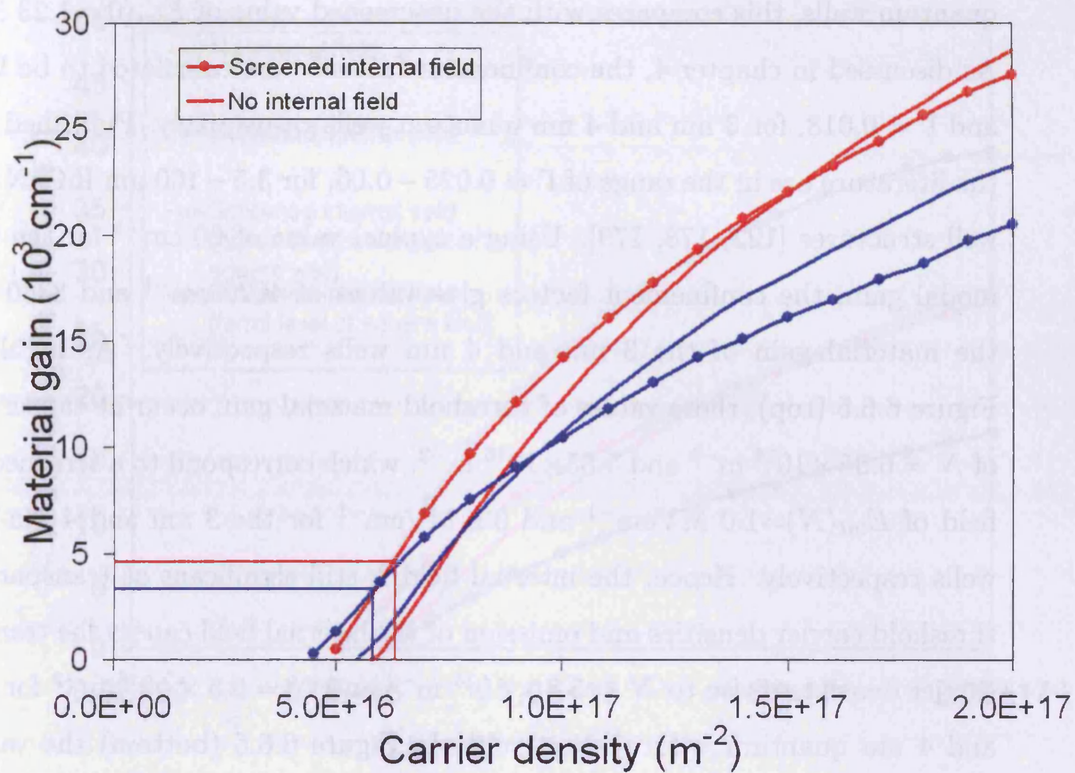

Figure 6.6.5: Variation of material gain with carrier and radiative current density for the 3 nm (red) and 4 nm (blue) quantum well structures, with (line and points) and without (line) the internal field. The threshold condition is also highlighted.

quantum wells, this compares with the unscreened value of $E_{int}(0)$=1.23 MVcm^{-1}. As discussed in chapter 4, the confinement factors were calculated to be $\Gamma = 0.013$ and $\Gamma = 0.018$, for 3 nm and 4 nm quantum wells respectively. Published values in the literature are in the range of $\Gamma = 0.025 - 0.06$, for $3.5 - 100$ nm InGaN quantum well structures [122, 178, 179]. Using a typical value of 60 cm^{-1} for the threshold modal gain, the confinement factors give values of 4620 cm^{-1} and 3330 cm^{-1} for the material gain of the 3 nm and 4 nm wells respectively. As highlighted in Figure 6.6.5 (top), these values of threshold material gain occur at carrier densities of $N = 6.35 \times 10^{16}$ m^{-2} and 5.85×10^{16} m^{-2}, which correspond to a screened internal field of $E_{int}(N)$=1.0 MVcm^{-1} and 0.9 MVcm^{-1} for the 3 nm and 4 nm quantum wells respectively. Hence, the internal field is still significant at transparency and threshold carrier densities and omission of the internal field causes the transparency carrier density to rise to $N = 5.8 \times 10^{16}$ m^{-2} and $N = 5.5 \times 10^{16}$ m^{-2} for the 3 nm and 4 nm quantum wells respectively. In Figure 6.6.5 (bottom) the variation of material gain with radiative current density is shown, it was calculated with a screened internal field and without a field (square well) for both the 3 nm and 4 nm quantum wells. The internal field causes a smaller transparency current in comparison to the square well case. With values of 210 Acm^{-2} and 150 Acm^{-2} for the skewed 3 nm and 4 nm quantum wells respectively, this compares to 260 Acm^{-2} and 240 Acm^{-2} when the internal field is omitted. At the threshold material gain of 4620 cm^{-1} and 3330 cm^{-1} the current has values of 290 Acm^{-2} and 235 Acm^{-2} for the skewed 3 nm and 4 nm quantum wells respectively, these values rise to 360 Acm^{-2} and 330 Acm^{-2} if the internal field is omitted.

To explain the observed shift in transparency carrier density and the crossover in the gain curves with and without the internal field, the effects of the Fermi energy and dipole matrix element on the gain were investigated. In Figure 6.6.6 (top), the variation in the gain with carrier density for the 3 nm quantum well sample with and without internal field is replotted from Figure 6.6.5 (top) along with two other artificial cases of when the effects of the internal field on the Fermi energy and the wavefunction separation are neglected separately. Each of these cases are unrealistic

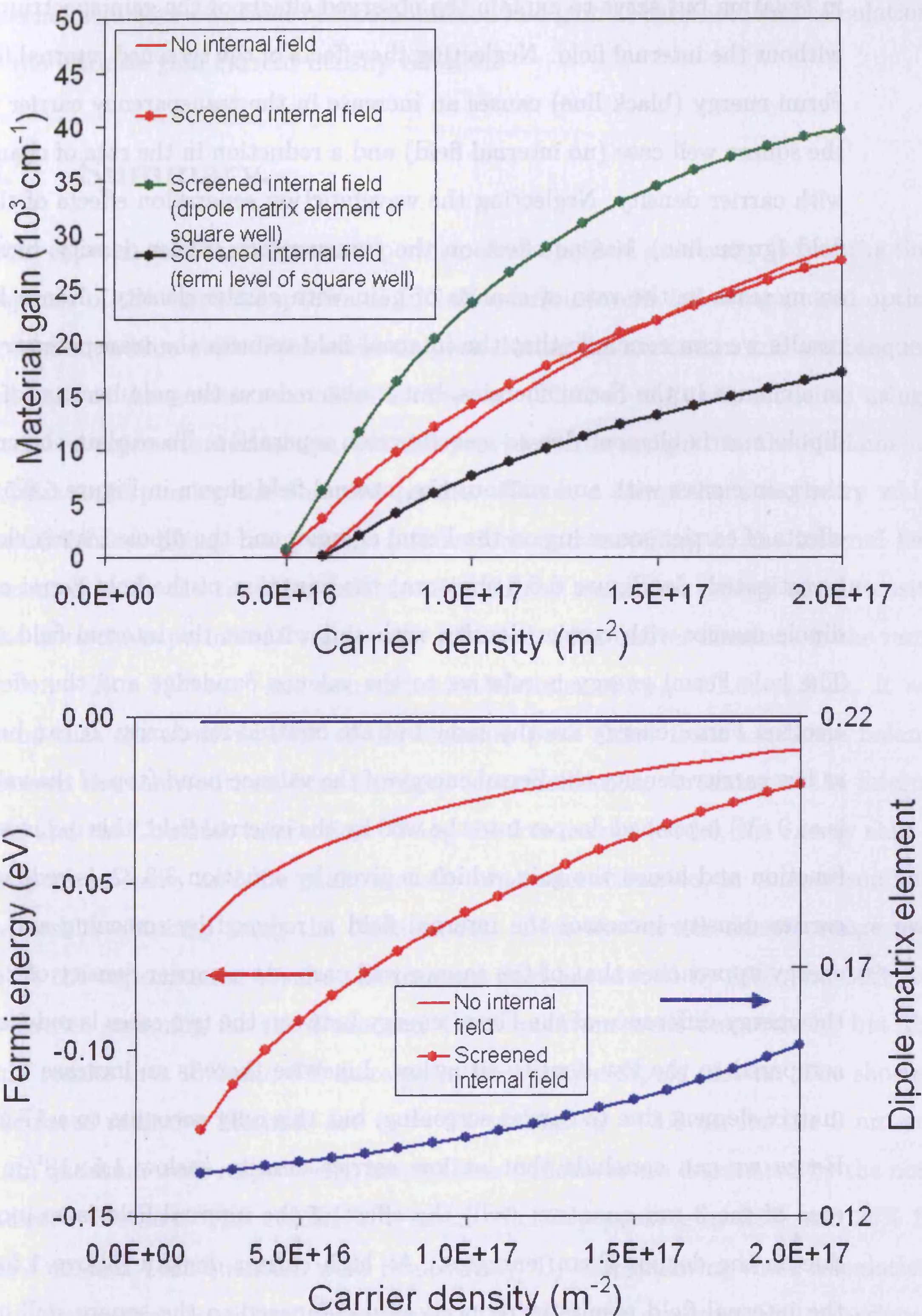

Figure 6.6.6: Variation of material gain (top), hole Fermi energy and dipole matrix element (bottom) with carrier density for the 3 nm quantum well structures with and without the internal field.

in isolation but serve to explain the observed effects of the gain spectrum with and without the internal field. Neglecting the effects of the screened internal field on the Fermi energy (black line) causes an increase in the transparency carrier density to the square well case (no internal field) and a reduction in the rate of change of gain with carrier density. Neglecting the wavefunction separation effects of the internal field (green line), has no effect on the transparency carrier density, but results in an increase in the rate of change of gain with carrier density. Hence from these results we can conclude that the internal field reduces the transparency point due to a change in the Fermi energies, but it also reduces the gain because of a reduced dipole matrix element due to wavefunction separation. To explain the crossover in the gain curves with and without the internal field shown in Figure 6.6.5 (top), the effects of carrier screening on the Fermi energies and the dipole matrix elements are investigated. In Figure 6.6.6 (bottom) the variation of the hole Fermi energy and dipole matrix with carrier density with and without the internal field are shown. The hole Fermi energy is relative to the valence bandedge and the effects on the electron Fermi energy are the same but are omitted for clarity. It can be seen that at low carrier density the Fermi energy of the valence band (top of the valence band is at 0 eV) is pushed deeper into the well by the internal field, this reduces the Fermi function and hence the gain, which is given by equation 3.3.22, is reduced. As the carrier density increases the internal field is reduced by screening and the Fermi energy approaches that of the square well case. At a carrier density of 2×10^{17}m^{-2}, the energy difference of the Fermi energy between the two cases is reduced by 83 % compared to the low density situation. Likewise there is an increase in the dipole matrix element due to carrier screening, but this only accounts to a 17 % increase. Hence we can conclude that at low carrier density (below 1.5×10^{17}m^{-2} for the case of the 3 nm quantum well) the effect of the internal field is to increase gain due to the deeper Fermi energies. At high carrier density (above 1.5×10^{17}m^{-2}) the internal field results in reduced gain compared to the square well case as the increase in internal field screening has a larger influence on the Fermi energies than the wavefunction overlap. These results underline the importance of including the

internal field in calculations of recombination and gain at threshold and calculations of the intrinsic gain current density relation.

6.7 Summary.

From experimental measurements performed at Sheffield university [64] of the time response of the emission spectra of InGaN quantum wells following pulsed optical excitation, a blue–shift of the emission peak during the excitation and a subsequent red–shift as the carriers recombine is observed. The red–shift was modelled using a stretched exponential lineshape, but this provided little insight into the fundamental physics underpinning the observed results. Hence, a comprehensive theory which includes band–filling, many–body interactions and screening of the internal field was used to fit the time dependence of both the transition energy and intensity. The fit to the experimental results was achieved using carrier densities in the range $N = 3 - 20 \times 10^{16}$ m^{-2} and non–radiative lifetimes of $\tau_{NR} = 1.6 - 1.8$ ns. It was found that the observed shift of the emission peak arises from a delicate balance between the contributions from bandgap renormalisation, screening of the internal field and the Coulomb interaction. Using the free carrier model, the energy shift of the peak intensity and the peak intensity are underestimated, in comparison with the results obtained using the Pade model. Over the carrier density range used to fit the experimental results the internal field is reduced by 55% and 30% due to carrier screening for the 3 nm and 4 nm quantum wells respectively, but this only results in a 15% and 5% increase in the relative dipole matrix. The shortest calculated radiative lifetimes are $\tau_R = 2.5$ ns and $\tau_R = 3.8$ ns, for the 3 nm and 4 nm quantum wells respectively, hence these structures are dominated by the non–radiative lifetime. This results in a small efficiency peaking at 28% and 25% for the 3 nm and 4 nm quantum wells respectively. By extrapolating these calculations to higher carrier densities, it was found that the 4 nm quantum well experiences a larger screening field than the 3 nm quantum well at the same carrier density. At a reference carrier density of $N = 2 \times 10^{17}$ m^{-2} the screened internal field is

reduced to 37% and 20% of the unscreened value for the 3 nm and 4 nm quantum wells respectively. Again it was found that although the internal field is strongly screened the change in the relative dipole matrix is small of the order of 9% and 23% for the 3 nm and 4 nm quantum wells respectively. A large change in the radiative lifetime from 20 ns to 2.5 ns over a carrier density range of $N = 1 - 20 \times 10^{16}$ m^{-2} was calculated. Finally from investigation of the gain it was found that at the threshold carrier densities of $N = 6.35 \times 10^{16}$ m^{-2} and $N = 5.85 \times 10^{16}$ m^{-2} for the 3 nm and 4 nm quantum wells respectively, the screened internal field had values of $E_{int}(N)$=1.0 MVcm^{-1} and 0.9 MVcm^{-1}, hence the internal field is still large at the threshold carrier density. Omission of the internal field results in a larger transparency carrier density and overestimates the rate of change of gain with carrier density. Hence at threshold conditions the internal field is substantial and from investigation of the gain–current density relationship it was found that omission of the internal field causes an increase in the transparency current from 210 Acm^{-2} and 150 Acm^{-2} for the 3 nm and 4 nm quantum wells respectively, to 260 Acm^{-2} and 240 Acm^{-2}.

Chapter 7

Summary and future work.

7.1 Summary.

In this thesis a theoretical method based on the Pade model has been presented allowing the properties of InGaN/GaN based quantum well structures to be studied and comparison made with experimental results. InGaN/GaN based quantum well structures are strained due to lattice mismatch between the well and barrier layers, this strain induces large internal fields, which skew the quantum wells, this has a large effect on the emission properties of these devices. In this thesis a method for the measurement of the internal field and the effects of carrier screening of the internal field in InGaN/GaN structures has been presented and the key results are summarised below.

Previously there has been a wide range of values for the internal field and the value of the experimentally determined internal piezoelectric field has been significantly smaller than theoretical values. The importance of using a correct description for the depletion widths of p–i–n structures has been established. By reassessing published work based on the p–n junction approximation, it has been established that it overestimates the depletion width and gives a reduced value for the internal field. Close correlation between the microscopic theory and reverse bias photocur-

rent absorption experiments performed by Pope [63] for the absorption peak energy has been obtained but it was found that the apparent magnitude of the absorption was probably affected by the efficiency with which carriers are extracted at low bias. Hence the energy of the peak absorption is more useful for experimental determination of the internal field. It has also been shown that the measured internal field of -1.9 MVcm^{-1} is consistent within the accepted uncertainty with the field of -1.8 MVcm^{-1} obtained from calculations using piezoelectric and elastic constants interpolated from the binaries listed in the work of Martin et al. [124].

From experimental measurements performed by Olaizola Izquierdo [64] on the time response of the emission spectra of InGaN quantum wells following pulsed optical excitation, a blue–shift of the emission peak during the excitation and a subsequent red–shift as the carriers recombine is observed. The red–shift was modelled using a stretched exponential lineshape, but this provided little insight into the fundamental physics underpinning the observed results. Hence, the Pade model which includes band–filling, many–body interactions and screening of the internal field was used to fit the time dependence of both the transition energy and intensity. The fit to the experimental results was achieved using carrier densities in the range of $N = 3 - 20 \times 10^{16}$ m^{-2} and non–radiative lifetimes of $\tau_{NR} = 1.6 - 1.8$ ns. It was found that the observed shift of the emission peak arises from a delicate balance between the contributions from bandgap renormalisation, screening of the internal field and the Coulomb interaction. Use of the free carrier model was found to underestimate the energy shift and magnitude of the peak intensity, in comparison with the results obtained using the Pade model. The shortest radiative lifetime was calculated as $\tau_R = 2.5$ ns, hence these structures are dominated by the non–radiative lifetime and the maximum efficiency of 28% was calculated. By extrapolating these calculations to higher carrier densities, it was found that the 4 nm quantum well experiences a larger screening field than the 3 nm quantum well at the same carrier density. At high carrier densities screening effects reduce the internal field to approximately a third of its unscreened value, but the change

in the dipole matrix is small of the order of 20% in comparison. At threshold it was found that the screened internal field is still substantial, being of the order of $E_{int}(N) = 0.9 - 1.0$ MVcm^{-1}, From investigation of the gain–current density relationship it was found that omission of the internal field causes an overestimation in the transparency current. Hence it is essential to include the screened internal field in the calculation of gain–current properties of InGaN/GaN laser structures, this is a significant result as the internal field is usually assumed to be fully screened in calculations of InGaN laser performance.

7.2 Future work.

In this work it was established that the internal field in InGaN quantum well structures is dominated by the strain induced piezoelectric field, GaN/AlGaN structures have much larger spontaneous polarisation coefficients than those of InGaN/GaN. Hence investigation of GaN/AlGaN and InGaN/GaN structures would permit the comparison of the effects of tensile and compressive strains and confirmation of the relative importance of piezoelectric and spontaneous fields.

An investigation into the importance of such effects by comparison of experimental data from a variety of sources with the calculated gain spectra would help resolve the degree to what such effects are important in InGaN structures.

Compositional fluctuations of indium content can create quantum dot like localized states, which have large effects on the gain spectrum. An investigation into the importance of such effects by comparison of experimental data from a variety of sources with the calculated gain spectra would help resolve the degree to what such effects are important in InGaN structures.

As found in chapter 5, the efficiency of sweeping out of carriers with reverse bias resulted in the theoretical model overestimating the magnitude of the absorption at small values of reverse bias. Looking at the flow of carriers through the complete structure using a current–continuity Schrodinger Poisson solver such as Simwin^{TM} [144] and using comparison with experimental absorption data to check

this model would be useful and might provide some evidence that the model correctly describes InGaN structures.

In addition temperature dependent theoretical modelling of the optical gain and spontaneous emission spectrum, would provide useful insights into operating conditions. this would be especially useful at low temperature, since it might allow further investigation of the relationship between the radiative and non–radiative lifetimes as discussed in chapter 6. Since non–radiative lifetimes should be much less important at low temperatures.

Bibliography

[1] J.H. Edgar. *Properties, Processing and Applications of Gallium Nitride and Related Semiconductors.* INSPEC: The Institution of Electrical Engineers, 1999.

[2] H. Feick. InGaN–based LEDs. www.mse.berkeley.edu/groups/weber/research/ganLED.html, 1999.

[3] H. Morkoc. *Nitride Semiconductors and Devices.* Springer, 1999.

[4] P.M. Sweeney, C.M. Harder, M.C. Cheung, A.N. Cartwright, F.H. Long, M.E. Aumer, S.F. LeBoeuf, and S.M. Bedair. Optimizing light emission from nitride quantum wells, 2001. GaAs MANTECH Conference, Las Vegas, NV.

[5] A. Girndt, F. Jahnke, S.W. Koch, and W.W. Chow. Microscopic gain theory for group III nitride semiconductor quantum wells. *Materials Science and Engineering B*, 50:174–179, 1997.

[6] C.Kittel. *Introduction to solid state physics.* Wiley, 1996.

[7] S.M. Sze. *Physics of Semiconductor Devices.* Wiley Interscience, 1981.

[8] L.A. Coldren and S.W. Corzine. *Diode Lasers and Photonic Integrated Circuits.* Wiley, 1995.

[9] A.E. Siegman. *Lasers.* University Science Books, 1986.

[10] J. Silfvast. *Laser Fundamentals.* Cambridge, 2000.

[11] D.V. Morgan and K. Board. *An introduction to semiconductor microtechnology.* Wiley, 1996.

[12] A.M. Fox. *Optical Properties of Solids.* Oxford, 2001.

[13] H. Amano, M. Kito, K. Hiramatsu, and I. Akasaki. P-type conduction in Mg-doped GaN treated with low–energy electron beam irradiation (leebi). *Japanese Journal Applied Physics*, 28(12):2112–2114, 1989.

[14] R. Winn Hardin. www.spie.org/web/oer/december/dec99/cover1.html. Challenges remain for blue diode lasers, 1999.

[15] D.M. Tricker, K. Jacobs, and C.J. Humphreys. Characterisation of epitaxial laterally overgrown gallium nitride using transmission electron microscopy. *PHYSICA STATUS SOLIDI B*, 216(1):633–637, 1999.

[16] G. Fasol. Room–temperature blue gallium nitride laser diode. www.sciencemag.org/cgi/content/full/272/5269/1751, 1996.

[17] Nichia. Nichia increases LED power by 10x. www.nichia.co.jp/info/news/new20020304.html, 2002.

[18] P. Blood. Out of the blue. *Chemistry in Britain*, July:38–40, 1999.

[19] ISI Web of Knowledge. www.wos.mimas.ac.uk/, 2003.

[20] G.B. Ren. *Investigation of optical properties in GaN quantum well structures.* PhD thesis, School of Physics and Astronomy: Cardiff University, 1999.

[21] H.K. Cho, J.Y. Lee, J. Humphreys, G.M. Yang, and C.S. Kim. Structural and optical characteristics of InGaN/GaN multiple quantum wells with different growth interruption. *Physica Status Solidi B*, 228(1):165–168, 2001.

[22] W.W. Chow, H. Amano, T. Takeuchi, and J. Han. Quantum well width dependence of threshold current density in InGaN lasers. *Applied Physics Letters*, 75(2):244–246, 1999.

[23] W.W. Chow, A.F. Wright, A. Girndt, F. Jahnke, and S.W. Koch. Microscopic theory of gain for an InGaN/AlGaN quantum well laser. *Applied Physics Letters*, 71(18):2608–2610, 1997.

[24] W.W. Chow and S.W. Koch. *Semiconductor–laser fundamentals.* Springer, 2000.

[25] C. H. Yan, H.W. Yao, J.J. Klaassen, M.F. Rosamond, and P.P. Chow. www.mrs.org/meetings/spring99/abstractbook/abstractbooky.html, 1999.

[26] M. Bugajski and W. Lewandowski. Concentration–dependent absorption and photoluminescence of n–type InP. *Journal of Applied Physics*, 57(2):521–530, 1985.

[27] S. Girlani and L.P. Sadwick. A photoluminescence study of gallium arsenide doped with silicon or beryllium. *Journal of Undergraduate Research: University of Utah*, 2(1), 1991.

[28] M. Ashraf Chaudhry, M. Shakeel Bilal, A.R. Kausar, and M. Altaf. Optical band gap of cadmium phosphate glass containing lanthanum oxide. *Il Nuovo Cimento*, 19:16214, 1997.

[29] A.T. Meney and E.P. O'Reilly. Theory of optical gain in ideal GaN heterostructure lasers. *Applied Physics Letters*, 67(20):3013–3015, 1995.

[30] G. Burns. *Solid State Physics.* Academic Press, 1990.

[31] J.S. Blakemore. *Solid State Physics.* Cambridge, 1985.

[32] S.H. Park and S.L. Chuang. Comparison of zinc–blende and wurtzite GaN semiconductors with spontaneous polarization and piezoelectric effects. *Journal of Applied Physics*, 87:353–364, 2000.

[33] Crystal Lattice Structures: Crystal Lattice Structures. www.nrl.navy.mil/lattice/struk.picts/, 2003.

[34] A. Bar–Lev. *Semiconductors and electronic devices.* Prentice Hall International, 1984.

[35] J. Singh. *Semiconductor Optoelectronics.* McGraw Hill, 1995.

[36] S. Strite and H. Morkoc. GaN, AlN, and InN: A Review, 2001. www.engineering.vcu.edu/fac/morkoc/learning/jvst_review.pdf.

[37] A. Hangleiter and edited by M. Osinski. Optical gain in wide–bandgap group–III nitrides. *Proceedings of SPIE CR83*, CR83(165):1–29, 2002.

[38] G. Frankowsky, F. Steuber, V. Harle, F. Scholz, and A. Hangleiter. Optical gain in GaInN/GaN heterostructures. *Applied Physics Letters*, 68(26):3746–3748, 1996.

[39] G. Koley. Advances in semiconductor devices, 2003. www.ee.sc.edu/classes/Fall03/elct871/Lecture%206–gk.ppt.

[40] J. Kuzmik. InAlN/InGaN high electron mobility transistors: some aspects of the quantum well heterostructure proposal. *Semiconductor Science and Technology*, 17(6):540–544, 2003.

[41] O. Ambacher. Growth and applications of group iii–nitrides. *Journal of Physics D: Applied Physics*, 31:2653–2710, 1998.

[42] Sumitomo Electric Industries. www.sei.co.jp/sn/2002/07/feature_article.html, 2002.

[43] Cree. www.cree.com, 2004.

[44] Piezo Kinetics (USA). www.piezo–kinetics.com/tutorial.htm, 2003.

[45] S. Elliott. *The Physics and Chemisty of Solids.* Wiley, 2000.

[46] American Piezo Ceramics. www.americanpiezo.com, 2003.

[47] eFunda: engineering fundamentals. www.efunda.com/materials/piezo/, 2003.

[48] H. Morkoc, R. Cingolani, F. Della Sala, A. Dicarlo, P. Lugli, and B. Gil. Polarization effects in nitride semiconductor heterostructures, 1999. www.engineering.vcu.edu/fac/morkoc/learning/wofe99_paper_rev4.pdf.

[49] J.R. Hook and H.E. Hall. *Solid State Physics.* Wiley, 1993.

[50] N.M. Johnson, A.V. Nurmikko, and S.P. DenBaars. Blue diode laser. *Physics Today*, 53(10):31, 2000.

[51] O. Madelung, M. Schulz, and H. Weiss. *Numerical data and functional relationships in science and technology: Volume 17.* Springer, 1982.

[52] V. Siklitsky. www.ioffe.rssi.ru/sva/nsm/semicond/, 2003.

[53] Office of Naval Research. www.onr.navy.mil/sci_tech/information/312_electronics/ncsr/materials/, 2004.

[54] S. Nakamura and G. Fasol. *The blue laser diode.* Springer, 1997.

[55] M.I. Nathan. Advances from japan: Review of 'the blue laser diode' [54]. www.sciencemag.org/cgi/content/full/277/5322/46b, 1997.

[56] S.H. Park, Y.T. Lee, and D. Ahn. Spontaneous polarization and piezoelectric effects on intraband relaxation time in wurzite GaN/AlGaN quantum well. *Applied Physics A*, 71:589–592, 2000.

[57] Blueray. Theory of group III nitride lasers. www.blu–ray.com/info/.

[58] J. Hellmig. DVD's: in the fast lane. *Physics World*, 17(7):21–24, 2004.

[59] cdfreaks. http://www.cdfreaks.com/article/186/, 2005.

[60] S. Nakamura and S.F. Chichibu. *Introduction to nitride semiconductor blue laser and light emitting diodes.* Taylor and Francis, 1999.

[61] S. F. Chichibu, T. Azuhata, T. Sota, T. Mukai, and S. Nakamura. Localized quantum well excitons in InGaN single–quantum–well amber light–emitting diodes. *Journal of Applied Physics*, 89(9):5153–5157, 2000.

[62] Ledtronics. What white–light LEDs can illuminate and how they can be used. www.ledtronics.com/pages/Utilizing_LEDs/White_LEDs.htm, 2003.

[63] I.A. Pope. *The Characterisation of InGaN/GaN Quantum well Light Emitting Diodes*. PhD thesis, School of Physics and Astronomy: Cardiff University, 2004.

[64] M. Olaizola Izquierdo. *Ultrafast spectroscopy of nitride semiconductors*. PhD thesis, Department of Physics and Astronomy: University of Sheffield, 2004.

[65] T. Takeuchi, C. Wetzel, S. Yamaguchi, H. Sakai, H. Amano, I. Akasaki, Y. Kaneko, S. Nakagawa, and N. Yamada. Determination of piezoelectric fields in strained GaInN quantum wells using the quantum–confined Stark effect. *Applied Physics Letters*, 73(12):1691–1693, 1998.

[66] Y.D. Jho, J.S. Yahng, E. Oh, and D.S. Kim. Field–dependent carrier decay dynamics in strained InN/GaN quantum wells. *Physical Review B*, 66(035334):1–11, 2002.

[67] A. Bykhovski, B. Gelmont, and M.Shur. The influence of the strain–induced electric field on the charge distribution in GaN-AlN-GaN structure. *Journal of Applied Physics*, 74(11):6734–6739, 1993.

[68] C.Y. Lai, T.M. Hsu, W.H. Chang, K.U. Tseng, C.M. Lee, C.C. Chuo, and J.I. Chyi. Direct measurement of piezoelectric field in $In_{0.23}Ga_{0.77}N$/GaN mqws by electrotransmission spectroscopy. *Journal of Applied Physics*, 91:531–533, 2002.

[69] H. Kollmer, J.S. Im, S. Heppel, J. Off, F. Scholz, and A. Hangleiter. Intra– and interwell transitions in GaInN/GaN multiple quantum wells with built–in piezoelectric fields. *Applied Physics Letters*, 74:82–84, 1999.

[70] O. Mayrock, H. J. Wunsche, and F. Henneberger. Polarization charge screening and indium surface segregation in (In,Ga)N/GaN single and multiple quantum wells. *Physical Review B*, 62:16870, 2000.

[71] J.S. Im, H. Kollmer, J. Off, A. Sohmer, F. Scholz, and A. Hangleiter. Reduction of oscillator strength due to piezoelectric fields in GaN/$Al_xGa_{1-x}N$ quantum wells. *Physical Review B*, 57(16):9435–9438, 1998.

[72] S.H. Park, S.L. Chuang, and D. Ahn. Piezoelectric effects on many–body optical gain of zinc–blende and wurtzite GaN/AlGaN quantum well lasers. *Applied Physics Letters*, 75(10):1354–1356, 1999.

[73] O. Ambacher, J. Majewski, C. Miskys, A. Link, M. Hermann, M. Eickhoff, M. Stutzmann, F. Bernardini, and V. Fiorentini. Pyroelectric properties of Al(In)GaN/GaN hetero– and QW structures. *Journal of Physics: Condensed Matter*, 14:3399–3434, 2002.

[74] T. Takeuchi, S. Sota, M. Katsuragawa, M. Komori, H. Takeuchi, H. Amano, and I. Akasaki. Quantum–confined Stark effect due to piezoelectric fields in GaInN strained quantum wells. *Japanese Journal Applied Physics*, 36(4A):382–384, 1997.

[75] T. Takeuchi, H. Takeuchi, S. Sota, H. Amano, and I. Akasaki. Optical properties of strained AlGaN and GaInN on GaN. *Japanese Journal Applied Physics*, 36(2B):177–179, 1997.

[76] C. Wetzel, T. Takeuchi, H. Amano, and I. Akasaki. Piezoelectric quantisation in GaInN thin films and multiple quantum well structures. *Materials Research Society Symposium Proceedings*, 512(1):181–183, 1998.

[77] N.W. Ashcroft and N.D. Mermin. *Solid State Physics.* Saunders College Publishing, 1988.

[78] W.J. Duffin. *Electricity and magnetism.* McGraw Hill, 1990.

[79] N.A. Shapiro, H. Feick, W. Hong, M. Cich, R. Armitage, and E.R. Weber. Luminescence energy and carrier lifetime in InGaN/GaN quantum wells as a function of applied biaxial strain. *Journal of Applied Physics*, 94(7):4520–4529, 2003.

[80] V. Fiorentini, F. Bernardini, F.D. Sala, A.D. Carlo, and P. Lugli. Effects of macroscopic polarization in III–V nitride multiple quantum wells. *Physical Review B*, 60(1):8849–8859, 1999.

[81] F. Bernardini, V. Fiorentini, and D. Vanderbilt. Spontaneous polarization and piezoelectric constants of III–V nitrides. *Physical Review B*, 56(16):10024–10027, 1997.

[82] S.F. Chichibu, T. Sota, K. Wada, S.P. DenBaars, and S. Nakamura. Spectroscopic studies in InGaN quantum wells. *Materials Research Society Internet Journal Nitride Semiconductor Research*, 2(7):1–12, 1999.

[83] C. Wetzel, H. Amano, and I. Akasaki. Piezoelectric polarization in GaInN/GaN heterostructures and some consequences for device design. *Japanese Journal of Applied Physics*, 39(1):2425–2430, 2000.

[84] H.S. Kim, J.Y. Lin, H.X. Jiang, W.W. Chow, A. Botchkarev, and H. Morkoc. Piezoelectric effects on the optical properties of GaN/$Al_xGa_{1-x}N$ multiple quantum wells. *Applied Physics Letters*, 73(23):3426–3428, 1998.

[85] A.N. Cartwright, P.M. Sweeney, T. Prunty, D.P. Bour, and M. Kneissel. electric field distribution in strained *p–i–n* GaN/InGaN multiple quantum well structures. *Materials Research Society Internet Journal Nitride Semiconductor Research*, 4(12):1–9, 1999.

[86] E.J. Miller and E.T. Yu. Influence of the dipole interaction energy on clustering in $In_xGa_{1-x}N$ alloys. *Applied Physics Letters*, 78(16):2303–2305, 2001.

[87] A. Hangleiter, J.S. Im, H. Kollmer, S. Heppel, J. Off, and F. Scholz. The role of piezoelectric fields in GaN–based quantum wells. *Materials Research Society Internet Journal Nitride Semiconductor Research*, 3(15):1–8, 1998.

[88] D. Ahn and S.L. Chuang. The theory of strained–layer quantum well lasers with bandgap renormalisation. *Institute of Electrical and Electronics Engineers: Journal of Quantum Electronics*, 30(2):350–365, 1994.

[89] R. Lakes. www.silver.neep.wisc.edu/∼lakes/poissonintro.html, 2001.

[90] A.F. Wright. Elastic properties of zinc-blende and wurtzite AlN,GaN, and InN. *Journal of Applied Physics*, 82:2833, 1997.

[91] Broholm. www.pha.jhu.edu/∼broholm/l39/node9.html, 1997.

[92] eFunda: engineering fundamentals. www.efunda.com/formulae/solid_mechanics/mat_mechanics/, 2003.

[93] E. Berkowicz, D. Gershoni, G. Bahir, E. Lakin, D. Shilo, E. Zolotoyabko, A.C. Abare, S.P. Denbaars, and L.A. Coldren. Measured and calculated radiative lifetime and optical absorption of InGaN/GaN quantum structures. *Physical Review B*, 61(16):10994–11008, 2000.

[94] W.W. Chow, M. Kira, and S.W. Koch. Microscopic theory of optical nonlinearities and spontaneous emission lifetime in group–III nitride quantum wells. *Physical Review B*, 60(1):1947–1952, 1999.

[95] J.J. Kim, S.H. Park, and H.M. Kim. Piezoelectric and spontaneous polarization effects on exciton binding energies in wurtzite GaN/AlGaN quantum wells. *Journal of the Korean Physical Society*, 43(1):149–153, 2003.

[96] H. Ouerdane. *Influence of ultrafast carrier dynamics on semiconductor absorption spectra.* PhD thesis, Department of Physics: Heriot–Watt University, 2001.

[97] C.F. Hsu, P.S. Zory, C.H. Wu, and M.A. Emanuel. Coulomb enhancement in InGaAs–GaAs quantum well lasers. *Institute of Electrical and Electronics Engineers: Journal of Selected Topics in Quantum Electronics*, 3(2):158–165, 1997.

[98] J.M. Zinman. *Principles of the theory of solids.* Cambridge, 1964.

[99] M. Lindberg and S.W. Koch. Effective bloch equations for semiconductors. *Physical Review B*, 38(1):3342–3350, 1988.

[100] H. Haug and S.W. Koch. *Quantum theory of the optical and electronic properties of semiconductors.* World Scientific, 1993.

[101] A. Goswami. *Quantum Mechanics.* Brown, 1997.

[102] J.R. Chelikowsky. The pseudopotential–density functional method (PDFM) applied to nanostructures. *Journal of Physics D*, 33(R33):1–39, 2000.

[103] O. Madelung. *Introduction to solid state theory.* Springer, 1978.

[104] H. Haug and S. Schmitt–Rink. Basic mechanisms of the optical nonlinearities of semiconductors near the band edge. *Journal of the Optical Society of America B*, 2(7):1135–1142, 1985.

[105] G. Woan. *The Cambridge Handbook of Physics Formulas.* Cambridge, 2000.

[106] G.D. Mahan. *Many Particle Physics.* Plenum Press, 1990.

[107] H. Haug and S.W. Koch. Semiconductor laser theory with many body effects. *Physcial Review A*, 39(4):1887–1898, 1989.

[108] Z.Mlejnkova. Bandgap renormalization, 1998. www.acms.arizona.edu/publication/pub_by_year/journals/ning–chow/.

[109] M. Yoshikawa, M. Kunzer, J. Wagner, H. Obloh, P. Schlotter, R. Schmidt, N. Herres, and U. Kaufmann. Band-gap renormalization and band filling in

Si-doped GaN films studied by photoluminescence spectroscopy. *Journal of Applied Physics*, 86(8):4400–4402, 1999.

[110] P.O. Holtz, S. Wongmanerod, B. Sernelius, and B. Monemar. p–type modulation doped GaAs/AlGaAs quantum wells, 1996. www.ifm.liu.se/matephys/AAnew/research/comp_oth/q2d.htm.

[111] S. Balle. Simple analytical approximations for the gain and refractive index spectra in quantum–well lasers. *Physical Review A*, 57:1304–1312, 1998.

[112] U. Bandelow, H.C. Kaiser, T. Koprucki, J. Rehberg, ed W. Jaeger, and ed H.J. Krebs. *Mathematics – Key Technology for the Future. Joint Projects Between Universities and Industry.* Springer–Verlag Berlin heidelberg, 2003.

[113] W.W. Chow. Sandia national laboratories, Albuquerque.

[114] M.R.H. Khan, Y. Koide, H.Itoh, N. Sawaki, and I. Akasaki. Edge emission of AlGaN. *Solid State Communications*, 60(6):509, 1986.

[115] S.L. Chuang. Optical gain of strained wurtzite GaN quantum well lasers. *Institute of Electrical and Electronics Engineers: Journal of Quantum Electronics*, 32(10):1791–1799, 1996.

[116] W.W. Chow, M. Hagerott Crawford, A. Girndt, and S.W. Koch. Threshold conditions for an ultraviolet wavelength GaN quantum well laser. *Institute of Electrical and Electronics Engineers: Journal of Selected Topics in Quantum Electronics*, 4(3):514–518, 1998.

[117] RF nitro communications. AlGaN/GaN transistor application notes characterization methods – NES epitaxial films, 2001. www.eettaiwan.com/ARTICLES/2001OCT/PDF/.

[118] T. Onuma, S.F. Chichibu, T. Aoyama, K. Nakajima, P. Ahmet, T. Azuhata, T. Chikyow, T. Sota, S. Nagahama, and T. Mukai. Influence of internal electric field on the recombination dynamics of localized excitons in an InGaN

double-quantum-well laser diode wafer operated at 450 nm. *Japanese Journal Applied Physics*, 42:7276–7283, 2003.

[119] S.H. Wei. III–nitride semiconductors for photo-voltaic applications. *NCPV and Solar Program Review Meeting*, 1(1):712–714, 2003.

[120] J. Wu, W. Walukiewicz, K.M. Yu, J.W. Ager, E.E. Haller, H. Lu, W.J. Schaff, Y. Saito, and Y. Nanishi. Unusual properties of the fundamental band gap of InN. *Applied Physics Letters*, 80(21):3967–3969, 2002.

[121] S.L. Chuang and C.S. Chang. A band–structure model of strained quantum–well wurtzite semiconductors. *Semiconductor Science and Technology*, 12:252–263, 1997.

[122] A.T. Meney, E.P. O'Reilly, and A.R. Adams. Optical gain in wide bandgap GaN quantum well lasers. *Semiconductor Science and Technology*, 11:897–903, 1996.

[123] V.W.L. Chin, T.L. Tansley, and T.Osotchan. Electron mobilities in gallium, indium, and aluminum nitrides. *Journal of Applied Physics*, 75(11):7365–7372, 1994.

[124] G. Martin, A. Botchkarev, A. Rocket, and H. Morkoc. Valence-band discontinuities of wurtzite GaN, AlN, and InN heterojunctions measured by x-ray photoemission spectroscopy. *Applied Physics Letters*, 68(18):2541–2543, 1996.

[125] A. Al–Yacoub, L. Bellaiche, and S.H. Wei. Piezoelectric coefficients of complex semiconductor alloys from first–principles: The case of $Ga_{1-x}In_xN$. *Physical Review Letters*, 89(5):57601–57604, 2002.

[126] P.S. Zory. *Quantum well lasers*. Academic Press Inc., 1993.

[127] W.W. Chow, P.M. Smowton, P. Blood, A. Girndt, F. Jahnke, and S.W. Koch. Comparison of experimental and theoretical GaInP quantum well gain spectra. *Applied Physics Letters*, 71(2):157–159, 1997.

[128] A.D. Andreev and E.P. O'Reilly. Theory of the gain characteristics of InGaN/AlGaN quantum dot lasers. *Materials Research Society Internet Journal Nitride Semiconductor Research*, 4S1(G6.45), 1999.

[129] P. Blood. Quantum well laser diodes: some practical issues. Cork Summer School, 2001.

[130] F. Jahnke and S.W. Koch. Many-body theory for semiconductor microcavity lasers. *Physical Review A*, 52(2):1712–1727, 1995.

[131] S. Wieczorek, W.W. Chow, S.R. Lee, A.J. Fischer, A.A. Allerman, and M.H. Crawford. Analysis of optical emission from high-aluminium AlGaN quantum well structres. *Applied Physics Letters*, 84(24):4899–4901, 2004.

[132] S.H. Park, J.I. Shim, K. Kudo, M. Asada, and S. Arai. Bandgap shrinkage in GaInAs/GaInAsP/InP multi–quantum well lasers. *Journal of Applied Physics*, 72(1):1, 1992.

[133] A. Tomita and A. Suzuki. Carrier–induced lasing wavelength shift for quantum well laser diodes. *Institute of Electrical and Electronics Engineers: Journal of Quantum Electronics*, 23(7):1155–1159, 1987.

[134] D.C. Reynolds, D.C. Look, and B. Jogai. Combined effects of screening and band gap renormalization on the energy of optical transitions in ZnO and GaN. *Journal of Applied Physics*, 88(10):5760–5763, 2000.

[135] M. Pophristic, F.H. Long, C. Tran, I.T. Ferguson, and R.F. Karlicek. Time resolved photoluminescence measurements of quantum dots in InGaN multiple quantum wells and light emitting diodes. *Journal of Applied Physics*, 86(2):1114–1118, 1999.

[136] S.F. Chichibu, A.C. Abare, M.S. Minsky, S. Keller, S.B. Fleischer, J.E. Bowers, E.Hu, U.K. Mishra, and L.A. Coldren. Effective band gap inhomogeneity and piezoelectric field in InGaN/GaN multiquantum well structures. *Applied Physics letters*, 73(14):2006–2008, 1998.

[137] F. Renner, P. Kiesel, G.H. Dhler, M. Kneissl, C.G. Van de Walle, and N.M. Johnson. Quantitative analysis of the polarization fields and absorption changes in InGaN/GaN quantum wells with electroabsorption spectroscopy. *Applied Physics Letters*, 81(3):490–492, 2002.

[138] A. Hangleiter, F. Hitzel, S. Lahmann, and U. Rossow. Compositional dependence of polarization fields in GaInN/GaN quantum wells. *Applied Physics Letters*, 83(6):1169–1171, 2003.

[139] Y.D. Jho, J.S. Yahng, E. Oh, and D.S. Kim. Measurement of piezoelectric field and tunnelling times in strongly biased InGaN/GaN quantum wells. *Applied Physics Letters*, 79(8):1130–1132, 2001.

[140] C. Wetzel, S. Nitta, T. Takeuchi, S. Yamaguchi, H. Amano, and I. Akasaki. On the bandstructure in GaInN/GaN heterostructures: strain, bandgap and piezoelectric effect. *Materials Research Society Internet Journal Nitride Semiconductor Research*, 3(31):1–10, 1998.

[141] F. Bernardini and V. Fiorentini. Macroscopic polarization and band offsets at nitride heterojunctions. *Physical Review B*, 57(16):9427–9430, 1998.

[142] F. Bernardini and V. Fiorentini. Spontaneous versus piezoelectric polarization in III-V nitrides: Conceptual aspects and practical consequences. *Physica Status Solidi (b)*, 216(1):391–398, 1999.

[143] C. Hepburn. www.britneyspears.ac/physics/pn/pnjunct.htm, 2002.

[144] D.W. Winston. www-ocs.colorado.edu/simwindows, 1999.

[145] K. Suzue, S.N. Mohammad, Z.F. Fan, W. Kim, and O. Aktas. Electrical conduction in platinum–gallium nitride Schottky diodes. *Journal of Applied Physics*, 80(8):4467–4478, 1996.

[146] K.A. Stroud. *Engineering Mathematics: 4th Edition.* Macmillan, 1995.

[147] B.V. Zeghbroeck. Principles of semiconductor devices, 1999.

[148] H.D. Summers, P.M. Smowton, P. Blood, M. Dineen, R.M. Perks, D.P. Bour, and M. Kneissel. Spatially and spectrally resolved measurements of optical loss in InGaN laser structures. *Journal of Crystal Growth*, 230:517–521, 2001.

[149] D.P. Bour, M. kneissel, L.T. Romano, R.M. Donaldson, C.J. Dunnrowicz, N.M. Johnson, and G.A. Evans. Stripe–width dependence of the threshold current for gain–guided AlGaInN laser diodes. *Applied Physics Letters*, 74(3):404–406, 1999.

[150] M. Kneiss, 2003. Private communication.

[151] M.E. Vickers, M.J. Kappers, and T.M. Smeeton. Determination of the indium content and layer thicknesses in InGaN/GaN quantum wells by X–ray scattering. *Journal of Applied Physics*, 94(3):1565–1574, 2003.

[152] P.M. Smowton, P. Blood, P.C. Mogensen, and D.P. Bour. Role of sublinear gain–current relationship in compressive and tensile strained 630 nm GaInP lasers. *International Journal of Optoelectronics*, 10(5):383–391, 1995.

[153] P. Blood. Measurement of optical absorption in epitaxial semiconductor layers by a photovoltage method. *Journal of Applied Physics*, 58(6):2288–2295, 1985.

[154] M. Ghisoni, G. Parry, S. Lycett, A. Dewdney, L. Hart, R. Murray, C. Button, and J.S. Roberts. Observation of blue shift in GaAs/InGaP quantum well *p-i-n* diodes. *Material Sci. and Eng. B*, 28:323–326, 1994.

[155] S.H. Park and S.L. Chuang. Piezoelectric effects on electrical and optical properties of wurtzite GaN/AlGaN quantum well lasers. *Applied Physics Letters*, 72(24):3103–3105, 1998.

[156] J. Piprek and S. Nakamura. Physics of high–power InGaN laser diodes. *Institution of Electrical Engineers Proceedings Optoelectronics*, 149(4):145–151, 2002.

[157] S.H. Park and S.L. Chuang. Spontaneous polarization effects in wurtzite GaN/AlGaN quantum wells and comparison with experiment. *Applied Physics Letters*, 76(15):1981–1983, 2000.

[158] J.S. Im, A. Moritz, F.Steuber, V. Harle, F. Scholz, and A. Hangleiter. Radiative carrier lifetime, momentum matrix element, and hole effective mass in GaN. *Applied Physics Letters*, 70(5):631–636, 1997.

[159] M.S. Minsky, S.B. Fleischer, A.C. Abare, J.E. Bowers, E.L. Hu, S. Keller, and S.P. Denbaars. Characterization of high–quality InGaN/GaN multiquantum wells with time–resolved photoluminescence. *Applied Physics Letters*, 72(9):1066–1068, 1998.

[160] S. Kalliakos, P. Lefebvre, and T. Taliercio. Nonlinear behaviour of photoabsorption in hexagonal nitride quantum wells due to free carrier screening of the internal fields. *Physical Review B*, 67(205307):1–10, 2003.

[161] J.C Holst, A. Hoffmann, D. Rudloff, F. Bertram, T. Riemann, J. Christen, T. Frey, D.J. As, D. Schikora, and K. Lischka. The origin of optical gain in cubic InGaN grown by molecular beam epitaxy. *Applied Physics Letters*, 76(20):2832–2834, 2000.

[162] M. Pophristic, F.H. Long, C. Tran, and I.T. Ferguson. Time resolved spectroscopy of InGaN. *Materials Research Society Internet Journal Nitride Semiconductor research*, 5S1(W11.58):1–6, 2000.

[163] S. F. Chichibu, T. Onuma, T. Sota, S.P. Denbaars, S. Nakamura, T. Kitamura, Y. Ishida, and H. Okumura. Localized exciton dynamics in strained cubic $In_{0.1}Ga_{0.9}N/GaN$ multiple quantum wells. *Journal of Applied Physics*, 93(4):2051–2054, 2003.

[164] F. H. Long, M. Pophristic, C. Tran, R.F. Kalicek, Z.C. Feng, and I. Ferguson. Time–resolved laser spectroscopy of nitride semiconductors. *Materials Science and Engineering B*, B59:147–149, 1999.

[165] M. Pophristic, F.H. Long, C. Tran, I.T. Ferguson, and R.F. Karlicek. Time resolved photoluminescence measurements of InGaN light emitting diodes. *Applied Physics letters*, 73(24):3550–3552, 1998.

[166] M. Buongiorno, K, Rapcewicz, and J. Bernholca. Polarization field effects on the electron–hole recombination dynamics in $In_{0.2}Ga_{0.8}N/In_{1-x}Ga_xN$ multiple quantum wells. *Applied Physics Letters*, 71(1):3135–3137, 1997.

[167] J. Wang, J.B. Jeon, Y. M. Sirenko, and K.W. Kim. Piezoelectric effect on optical properties of psudomorphically strained wurtzite GaN quantum wells. *Institute of Electrical and Electronics Engineers: Photonics Technology Letters*, 9(6):728–730, 1997.

[168] J.A. Davidson, P. Dawson, T. Wang, T. Sugahara, J.W. Orton, and S. Sakai. Photoluminescence studies of InGaN/GaN multi–quantum wells. *Semiconductor Science and Technology*, 15:497–505, 2000.

[169] C. Wetzel, T. Takeuchi, H. Amano, and I. Akasaki. Piezoelectric Franz–Keldysh effect in strained GaInN/GaN heterostructures. *Journal of Applied Physics*, 85(3):3786–3790, 1999.

[170] F. Della Sala, A. Di Carlo, P. Lugli, F. Bernardini, V. Fiorentini, R.Scholz, and J.M. Jancu. Free-carrier screening of polarization fields in wurtzite GaN/InGaN laser structures. *Applied Physics letters*, 14:2002–2004, 1999.

[171] W.W. Chow, H. Amano, and I. Akasaki. Theoretical analysis of filamentation and fundamental–mode operation in InGaN quantum well lasers. *Applied Physics Letters*, 76(13):1647–1649, 2000.

[172] H.S. Kim, J.Y. Lin, H.X. Jiang, W.W. Chow, A. Botchkarev, and H. Morkoc. Piezoelectric effects in GaN/AlGaN multiple quantum wells probed by picosecond time resolved photoluminescence. *Materials Research Society Internet Journal Nitride Semiconductor Research*, 4S1(G3.3):–, 1999.

[173] K.F. Riley, M.P. Hobson, and S.J. Bence. *Mathematical methods for physics and engineering.* Cambridge, 1998.

[174] J.F. Muth, J.D. Brown, M.A.L. Johnson, Z. Yu, R.M. Kolbas, J.W. Cook, and J.F. Schetzina. Absorption coefficient and refractive index of GaN, AlN and AlGaN alloys. *Materials Research Society Internet Journal Nitride Semiconductor research*, 4S(1):5.2, 1999.

[175] P. Trautman, K. Pakula, and J.M. Baranowski. The fundamental absorption edge of high crystalline quality GaN, 2004. MRS Fall meeting: Symposium.

[176] P. Lefebvre, A. Morel, M. Gallart, T. Taliercio, J. Allegre, B. Gil, H. Mathieu, B. Damilano, N. Grandjean, and J. Massie. High internal electric field in a graded–width InGaN/GaN quantum well: Accurate determination by time–resolved photoluminescence spectroscopy. *Applied Physics Letters*, 9(1):1252–1254, 2001.

[177] J.D. Thomson, I.A. Pope, P.M. Smowton, P. Blood, R.J. Lynch, G. Hill, T. Wang, and P.J. Parbrook. The influence of acceptor anneal temperature on the performance of InGaN/GaN quantum well light emitting diodes. *Applied physics letters.*

[178] D.A. Stocker, E.F. Schubert, and J.M. Redwing. Optically pumped InGaN-GaN lasers with wet-etched facets. *Applied physics letters*, 77(26):4253–4255, 2000.

[179] S. Nakamura. GaN-based blue/green semiconductor laser. *Institute of Electrical and Electronics Engineers: Journal of Selected Topics in Quantum Electronics*, 3(2):435–442, 1997.